Deep Ultraviolet Light Emitters Based on (Al,Ga)N/GaN Semiconductor Heterostructures

Submitted in partial fulfillment of the requirements for

the degree of

Doctor of Philosophy

in

Department of Material Science and Engineering

Yu-Han Liang

B.S., Materials Science and Engineering, Feng Chia University
M.S., Materials Science and Engineering, National Cheng Kung University

Carnegie Mellon University
Pittsburgh, PA

August, 2017

Abstract

Deep ultraviolet (UV) light sources are useful in a number of applications that include sterilization, medical diagnostics, as well as chemical and biological identification. However, state-of-the-art deep UV light-emitting diodes and lasers made from semiconductors still suffer from low external quantum efficiency and low output powers. These limitations make them costly and ineffective in a wide range of applications. Deep UV sources such as lasers that currently exist are prohibitively bulky, complicated, and expensive. This is typically because they are constituted of an assemblage of two to three other lasers in tandem to facilitate sequential harmonic generation that ultimately results in the desired deep UV wavelength.

For semiconductor-based deep UV sources, the most challenging difficulty has been finding ways to optimally dope the (Al,Ga)N/GaN heterostructures essential for UV-C light sources. It has proven to be very difficult to achieve high free carrier concentrations and low resistivities in high-aluminum-containing III-nitrides. As a result, p-type doped aluminum-free III-nitrides are employed as the p-type contact layers in UV light-emitting diode structures. However, because of impedance-mismatch issues, light extraction from the device and consequently the overall external quantum efficiency is drastically reduced. This problem is compounded with high losses and low gain when one tries to make UV nitride lasers.

In this thesis, we provide a robust and reproducible approach to resolving most of these challenges. By using a liquid-metal-enabled growth mode in a plasma-assisted molecular beam epitaxy process, we show that highly-doped aluminum containing III-nitride films can be achieved. This growth mode is driven by kinetics. Using this approach, we have

been able to achieve extremely high p-type and n-type doping in (Al,Ga)N films with high aluminum content. By incorporating a very high density of Mg atoms in (Al,Ga)N films, we have been able to show, by temperature-dependent photoluminescence, that the activation energy of the acceptors is substantially lower, thus allowing a higher hole concentration than usual to be available for conduction. It is believed that the lower activation energy is a result of an impurity band tail induced by the high Mg concentration. The successful p-type doping of high aluminum-content (Al,Ga)N has allowed us to demonstrate operation of deep ultraviolet LEDs emitting at 274 nm. This achievement paves the way for making lasers that emit in the UV-C region of the spectrum. In this thesis, we performed preliminary work on using our structures to make UV-C lasers based on photonic crystal nanocavity structures. The nanocavity laser structures show that the threshold optical pumping power necessary to reach lasing is much lower than in conventional edge-emitting lasers. Furthermore, the photonic crystal nanocavity structure has a small mode volume and does not need mirrors for optical feedback. These advantages significantly reduce material loss and eliminate mirror loss. This structure therefore potentially opens the door to achieving efficient and compact lasers in the UV-C region of the spectrum.

Acknowledgements

I would like to thank my advisor, Prof. E. Towe, for encouragement, guidance, and support throughout my Ph.D. program. His profound knowledge inspires me to come up with many new ideas on photonic and optoelectronic semiconductor materials and devices.

I also want to express my gratitude to all the members of my dissertation committee: Professor R. Davis, Professor H. K. Kim, and Professor D. Lambeth for taking the time to evaluate my work and for their useful suggestions.

I thank Dr. Y. Luo for encouraging and supporting me in my research. Finally, I want to express my heartfelt thanks to my family: my parents, my wife, and my son for their constant support during my Ph.D program.

This work was partially supported by DARPA, an agency of the U.S. Department of Defense, though the Space and Naval Warfare Systems Center under Grant No. N66001-12-1-4202.

List of Figure

Table of Contents

Chapter 1

Introduction

It is critical and timely to develop compact, highly efficient, and environmentally friendly deep ultraviolet light-emitting sources that emit in the UV-A (400 – 320 nm), UV-B (320 – 280 nm), and UV-C (280 – 100 nm) regions of the spectrum. These spectral regions are of considerable interest for some important potential applications summarized in Figure 1-1. Some miscellaneous applications of UVA and UVB light emitters include high density optical storage, and phototherapy for treatment of psoriasis and vitiligo. Higher volume of applications of UVC light sources include near-line-of-sight (NLOS) communications, sterilization, water purification, and biomedical diagnostics. In biochemical detection as an example, only a few chromophores absorb in the visible region, whereas all functional agents absorb in the UVC region. Due to the myriads of applications, progress in the development of solid-state UV light-emitting sources has surged in recent decades.

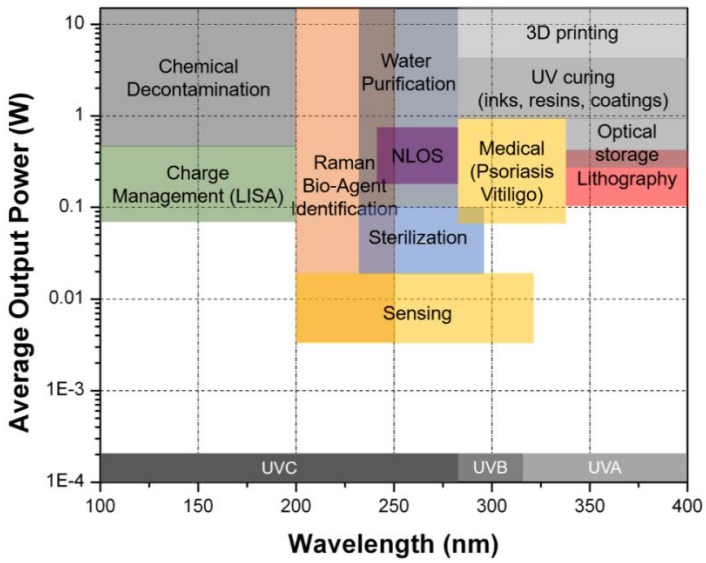

Figure 1-1: Application areas of ultraviolet light emitting devices.

Compared to conventional UV light sources, such as mercury lamps, ultraviolet LEDs offer a number of advantages: robustness, compactness, environmental friendliness, fast on-and-off switching, and long lifetimes. The achieved and projected performance of UV light-emitting diodes (LEDs) is summarized in Figure 1-2 [1]. In the past decade, UVA LEDs with excellent performance have begun to replace some conventional ultraviolet light lamps. However, deep ultraviolet LEDs in UVB and particularly UVC range still suffer from extremely low external quantum efficiency (EQE), which is a function of the internal quantum efficiency (IQE) in the active layer. This performance metric is defined as

$$EQE = \frac{\text{number of photons emitted into free space}}{\text{number of electrons injected into LED}} = \frac{P/(h\nu)}{I/e} = IQE \cdot LEE$$

where LEE represents light extraction efficiency.

To date, the highest EQE of deep UV light-emitting diodes is extremely low: it is currently about 20 % and was achieved by Takayoshi *et al.* [2]. In addition, most UVB and UVC LEDs provide only a few milliwatts or less of output power. These twin problems prevent ultraviolet LEDs from widespread applications. Ultraviolet light sources that exhibit narrow linewidths, high beam quality, and high output powers would therefore provide more functionality for applications in biochemical detection, general sensing, and non-line-of-slight communication. For example, intense UV lasers are required in order to achieve adequate signal-to-noise ratios in identifying diverse biological and chemical compounds in Raman spectroscopy. However, producing a UV laser diode has proved to be even more difficult because of the need for significant gain to overcome losses. The peak gain coefficient, $g(n)$, can be expressed as

$$g(n) = g'(n - n_{tr}) \tag{1-1}$$

where g' is the differential gain ($\frac{\partial g}{\partial n}$), and n_{tr} is the transparency carrier concentration when the gain is zero. The threshold condition (g_{th}) is when peak gain equals the sum of the intrinsic loss (α_i) and the mirror transmission loss (α_m); this is given as

$$\Gamma g_{th} = \alpha_i + \alpha_m$$
$$\alpha_m = \frac{1}{2L} ln \frac{1}{R_1 R_2} \tag{1-2}$$

where Γ is the optical confinement factor, L is the length of the cavity, and R_1 and R_2 represent the reflectivity of the facet mirrors in a cavity. The relationship between optical gain and bias current can be described by the linear expression

$$g = \frac{g_0}{J_0}\left(\frac{J\eta_i}{d} - J_0\right) \tag{1-3}$$

where η_i is the internal quantum efficiency, d is the thickness of an active layer, and J_0 is normalized transparency current density ($J_0 \equiv J_{tr}/d$). By combining Equation (1-2) and (1-3), the threshold current density for lasing can be given by

$$J_{th} = \frac{J_0 d}{\eta_i}\left(1 + \frac{g_{th}}{g_0}\right) = \frac{J_0 d}{\eta_i}\left(1 + \frac{1}{g_0 \Gamma}\left(\alpha_i + \frac{1}{2L} ln \frac{1}{R_1 R_2}\right)\right) \tag{1-4}$$

From the discussion above, it is clear that a laser diode requires high current injection and low losses to achieve lasing. These conditions, however, are very difficult to achieve in AlGaN-based ultra-wide bandgap semiconductors. This has restricted the development of low-cost and compact deep-UV lasers, thus limiting a range of possible applications for this technology. A summary of recent developments in UV current-injected laser diodes is shown in Figure 1-3 [3]. This figure shows that the shortest wavelength laser diode is at 336 nm; this result was reported by Hamamatsu [4]. We summarize the key challenges in the development of AlGaN-based UV light emitters in the

following paragraphs. Most of the problems are common to the realization of both lasers and LEDs operating in the deep UV region.

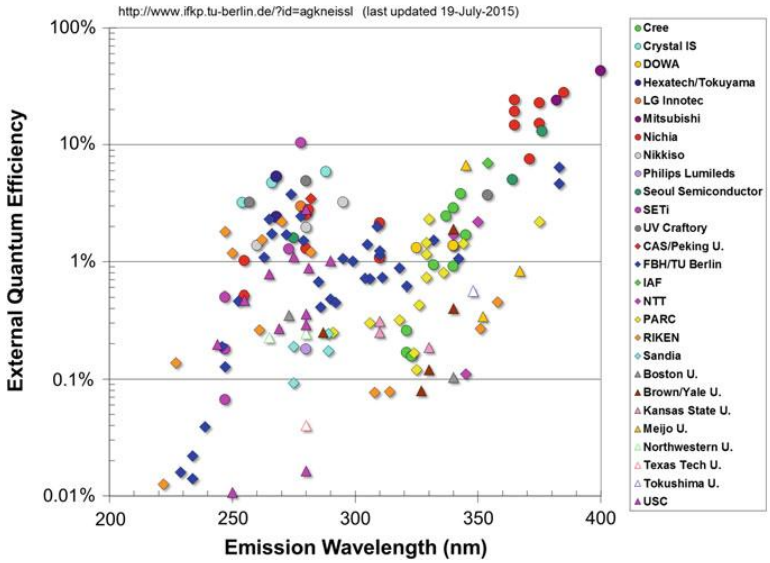

Figure 1-2: Achieved and projected performance of near and deep UV LEDs [1].

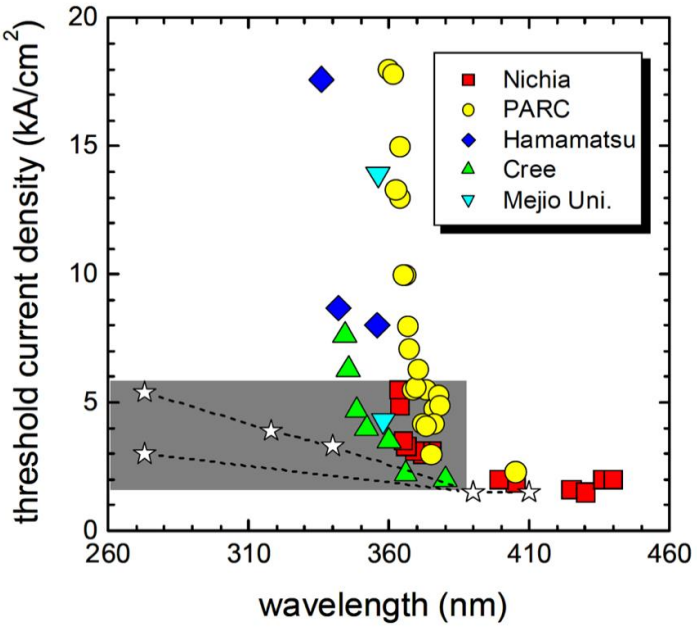

Figure 1-3: Measured threshold current density for III-nitride-based ultraviolet laser diodes [3].

One of the significant challenges for AlGaN-based emitters is lack of native substrates for lattice-matched epitaxial growth. Although GaN and AlN bulk substrates are commercially available, they are still expensive, small-sized and not of sufficiently high quality. In addition, because of the wide range of film compositions and lattice constants in a typical device structure, lattice-mismatch-induced defects still limit the performance of ultraviolet devices. Currently, sapphire is therefore the most popular substrate for growing III-nitrides primarily because it is low cost and readily available in high quality. The only problem is the large lattice mismatch between sapphire and III-nitrides. This leads to a high density of dislocations which act as non-radiative recombination centers that limit the internal quantum efficiency for both LEDs and laser diodes.

Another major challenge is to fabricate highly doped and low resistivity n-type and especially p-type III-nitride alloys with aluminum mole fractions greater than 30%. This is primarily due to the high ionization energies for Mg acceptors (630 meV) and Si donors (282 meV) in AlN [5] and (Al,Ga)N alloys. As a result, only a small portion (about 1 %) of Mg acceptors are ionized at room temperature in Mg-doped AlGaN films, resulting in low free hole concentrations and high resistivity. Apart from the low thermally activated hole density, the bottleneck of low solubility in GaN and AlN materials strongly restricts the efficiency of Mg doping in AlGaN films. This limited solubility becomes obvious at higher Al content in $Al_XGa_{1-X}N$ because the formation enthalpy of Mg_{Al} in AlN is much higher than that for Mg_{Ga} in GaN [6]. In addition, AlGaN materials typically suffer from a high density of compensating defects, such as nitrogen vacancies and oxygen and hydrogen impurities. Among the defects, nitrogen vacancies have been proposed as the most dominant compensating centers in Mg-doped $Al_XGa_{1-X}N$ materials. They are more likely to be

generated in AlN than in GaN due to a strikingly lower formation energy in AlN [7]. These problems make it difficult to achieve effective doping, particularly in p-type films. To exacerbate the problem, good ohmic contacts are difficult to achieve in p-type (Al, Ga)N due to lack of universal metals with the right work functions. These factors contribute to the relatively high operating voltages of UV light-emitting devices. To circumvent this doping issue, most researchers use p-type GaN instead of transparent p-type AlGaN as a contact layer to reduce resistivity and increase hole concentration. However, this brings the problem of absorption of UV light by the top-most p-GaN layer, thus reducing the light extraction efficiency in ultraviolet LEDs; yet another problem is the back reflection of UV light at the sapphire/air interface on the bottom surface due to total internal reflection.

Due to these cumulative problems, it is very difficult to achieve UV lasers in typical electrically-driven stripe-geometry laser diodes such as that illustrated in Figure 1-4. This is due to the fact that to simultaneously achieve optical and electrical confinement is very difficult. To achieve optical confinement, a cladding layer of high Al-containing AlGaN with low index should be employed. This however makes it difficult to achieve high carrier concentration and low resistivity in the high-aluminum-containing AlGaN layer. This subsequently makes it difficult to create population inversion in the large bandgap gain media. Furthermore, increasing the index of refraction discontinuity in the layers leads to more dislocations because of the large lattice mismatch in the epilayers; this of course reduces carrier recombination efficiency. Another practical issue is that it is difficult to make Fabry-Perot mirror facets by cleaving the sapphire substrate to make conventional edge-emitting UV laser diodes. Any mirror facets made by dry or wet chemical etching have large facet losses that significantly impact the performance of UV laser diodes.

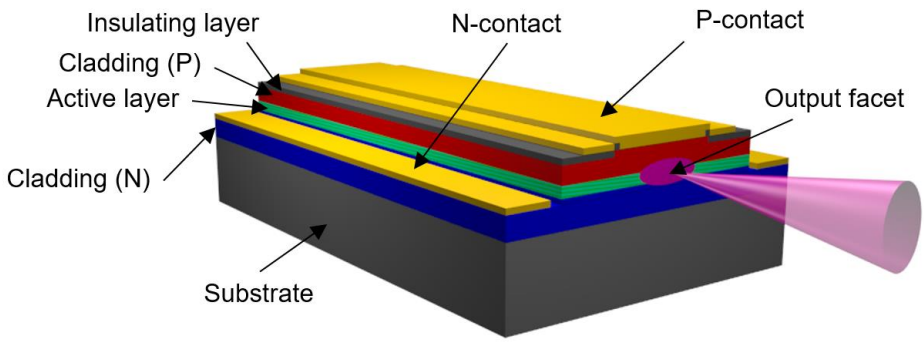

Figure 1-4: A typical configuration of ridge-type edge-emitting laser.

The primary objective of this thesis is to resolve the key problems of Mg- and Si-doped (Al,Ga)N films and their film quality grown by plasma-assisted molecular beam epitaxy; the secondary objective is to demonstrate a high efficiency deep ultraviolet LED, and thereby pave the path to the realization of ultraviolet laser diodes. We also theoretically investigate the potential of the ultraviolet laser based on a photonic crystal structure.

1.1 State-of-the-art III-Nitride semiconductor ultraviolet laser diodes

In this Section, we review recent developments in III-nitride semiconductor UV laser diodes. Since the first III-nitride laser diodes were reported by Nakamura and coworkers in 1996 [8], these devices (particularly in the blue) continue to revolutionize our lives. Over time, applications that require compact, high power light sources with shorter wavelengths have created an imperative to develop electrically-pumped ultraviolet laser diodes. To achieve devices with these shorter wavelengths requires AlGaN films with higher aluminum

compositions. No functioning electrically-driven ultraviolet laser diodes have so far been fabricated from the nitride materials.

1.1.1 Prior approaches to resolving the challenges of making UV lasers

Of the many challenges we have already discussed in the previous Section, the biggest is the lack of suitable substrates on which to grow high crystalline quality aluminum containing III-nitride layers. Bulk AlN substrates are currently the only alternative substrates for growth of UV laser structures that emit at short wavelengths. The first electrically-driven UV laser diode at 368 nm grown on an AlN substrate was reported by M. Kneissl *et al.* in 2007 [9]. Even though the threading dislocation density of the AlGaN heterostructures was reduced to the range of mid–10^8 cm^{-2}, the threshold current density was 13 kA/cm^2, which is very high; it is even worse for UV lasers with shorter wavelengths.

Unlike the case for UV LEDs, where satisfactory performance can be realized with partial absorption in the p-type layers, the p-side of a laser diode must be highly transparent. Ultra-violet lasers therefore require p-type AlGaN cladding layers with high aluminum mole fractions with minimal absorption. This requirement is contingent on achieving high p-type doping concentration and low resistivity in the Mg-doped AlGaN layers. Many approaches have been proposed to resolve this problem. Simon *et al.* proposed an approach that enhances p-type polarization doping by using compositionally graded AlGaN alloys [10]. This takes advantage of the existence of acceptor-like or donor-like impurities or defects that can be ionized by polarization. However, Moustakas *et al.* have reported that the acceptor-like and donor-like polarization-induced impurities or defects generated by this approach are insufficient for p-type and n-type doping without incorporation of intentional dopants [11]. Another viable approach is to use a short period Mg-doped $Al_xGa_{1-x}N/Al_yGa_{1-y}N$ superlattice

(SPSL), first proposed by Schubert *et al.* [12]. This technique increases the overall hole concentration by allowing deep acceptors in the wide band gap barriers to ionize into the valence band of the neighboring narrow band-gap nitrides, rather than into the valence band of the bulk material. The method allows both vertical and lateral hole transport since the SPSLs are very thin; the approach has recently been demonstrated in UV light-emitting diodes [12, 13]. However, the p-type AlGaN superlattices still suffer from a high resistance that leads to significant electrical losses. Another recent approach is by Rajan *et al.* where they proposed and experimentally demonstrated use of quantum tunneling junctions with high hole injection efficiency in UV LEDs [14, 15]. Forming a tunneling diode, however, typically requires degenerate doping of both the p-type and n-type regions. This is a difficult materials problem: it is almost impossible to achieve degenerate p^+-type doping in AlGaN with high Al mole content. Such tunneling heterostructures are therefore of limited practical use in deep ultraviolet devices emitting in the UVC region. The simultaneous achievement of the desired electrical performance and the low optical absorption is still a difficult and unresolved problem.

1.1.2 Alternative concepts for compact UV III-nitride lasers

Alternative methods to circumvent the problems discussed in the previous Section have been proposed. One promising approach is to utilize electron-beam pumped multi-quantum wells. Non-equilibrium electron-hole pairs in electron-beam pumped lasers are generated by ionization of the lattice atoms and avalanche electron collisions initially injected by the electron beam. Oto *et al.* reported deep UV emission at 240 nm from electron-beam pumped AlGaN/AlN quantum wells that resulted in a high output power of 100 mW with power efficiency of 40% [17]. Shimahara *et al.* demonstrated a device with an

output power of 20 mW, with a power efficiency of 4%. An electron-beam pumped UV device using Si-doped AlGaN films that provide higher emission intensity at 247 nm with an output power of 2.2 mW and a power efficiency of 0.24% was reported by Shimahara *et al.* [18]. Most recently, Matsumoto *et al*. also demonstrated deep UV emission in AlGaN/AlN quantum wells using graphene nanoneedle field emitters [19]. Although several efforts have succeeded in achieving deep UV laser emission by electron-beam pumping, the major drawbacks of this method are the bulk and low electron generation efficiency of the electron-beam sources. Another challenge is the fact that photons are not well confined in the active region and thus stimulated emission is difficult to achieve. Heating is also problem; this arises from the electron-phonon interactions and the quasi-equilibrium electron-hole plasma in the active region of the crystal due to the high intensity electron beam.

Second harmonic generation (SHG) is another promising method for achieving electrically-pumped deep UV laser. Conventionally, it involves passing a high power beam in the infrared spectral range though multiple stages of nonlinear crystals which convert the long wavelengths to visible light. However, there is a limited number of frequency-doubling materials for deep UV light emitters. Most common non-linear crystal materials absorb the UV light. Furthermore, it is difficult to meet the critical phase matching condition for efficient second harmonic generation. The most suitable nonlinear optical material is β-BaB_2O_4 (BBO). Tangtrongbenchasil *et al.* reported the generation of UVC light at the wavelength of 220 nm from a BBO nonlinear crystal by using a blue laser diode at 440 nm as the fundamental input light [20]. Large inefficiencies and the cumbersome optical setup of this method make it of limited practical use.

Most recently, Mi and his coworkers [21] successfully demonstrated optically-pumped ultraviolet lasers by employing tapered AlGaN nanowire structures. These nanostructures, nearly free of structural defects, were directly grown on n-type Si substrates by plasma-assisted MBE [21–23]. The tapered geometry effectively reduces the refractive index at the bottom of nanowires, thereby preventing significant optical loss through the underlying Si substrate. Although lasing characteristics with a low threshold current density of 200 A/cm^2 is demonstrated because of the high quality (Q) factor of the optical cavity, the device operates at 77K. One of the significant unresolved issues with this approach is how to make a good ohmic contact without utilizing any filling materials. Contact metals are likely to deposit on the side walls of the nanowires and cause electrical shorts. Another issue is that it is very difficult to control the size and spacing of the nanowires. Effective tailoring of the wavelength and the other optical properties of the laser are still challenges. Although the AlGaN-based nanowires represent a breakthrough into UV laser technology, they still have a long way to go in realizing commercially viable and electrically-driven laser devices that can operate at room-temperature.

In summary, we have discussed the major challenges in developing electrically-driven UV laser diodes based on wide band gap III-nitride semiconductors. A number of novel heterostructure devices have been proposed to improve the device structures necessary for efficient current injection. Despite the progress made to date on the development of sub-300 nm emitters, the achievable optical gain through electrical injection does not yet exceed the intrinsic and mirror losses. Consequently, the shortest wavelength of AlGaN-based laser diodes reported has remained at 336 nm [4]. For devices grown by molecular beam epitaxy,

the wavelength of ultraviolet laser diodes operating at room-temperature has not yet been pushed below 388 nm [24].

1.1.3 Are advanced photonic crystal lasers feasible in the UV region?

Except for the alternative UV laser designs already discussed, miniaturization of photonic crystal lasers offers another option. This approach provides a new pathway to achieving a compact UV laser. A typical defect-type photonic crystal structure, illustrated in Figure 1-5, is composed of a periodic dielectric membrane with a defect region. The defect region provides a resonant cavity with a high quality (Q) factor and very small mode volume (V_{mode}). This high ratio of quality factor to modal volume (Q/V_{mode}) promotes a high radiative recombination rate which is enhanced through the Purcell effect, whose enhancement factor is usually expressed as

$$F_P = \frac{3}{4\pi^2}\left(\frac{\lambda}{n}\right)^3 \frac{Q}{V_{mode}} \tag{1-5}$$

This feature leads to extremely low threshold current (I_{th}), given as [25]

$$I_{th} = \left(\frac{qN_0V_{mode}}{\tau_{sp}} + \frac{q\gamma}{\beta}\right) + I_{nr} \tag{1-6}$$

where N_0 is the transparency carrier density, τ_{sp} represents spontaneous emission time into all optical modes. The second term in Eq. (1-6) represents the current needed to overcome losses in the optical cavity, while the last term I_{nr} is the current for non-radiative process.

The Purcell effect has been extensively studied on photonic crystal lasers based on III-arsenide and III-phosphide semiconductors in the past decades. Vuckovic *et al.*, for example, reported work on visible and near infrared photonic crystal lasers based on (In, Ga) (As, P) materials [25–30]. However, there are only a few reports on photonic crystal

nanocavity laser in ultraviolet region. Wu *et al.* demonstrated use of ZnO ultraviolet photonic crystal structure that lased at the wavelength of 388 nm under optical pumping at room temperature [31]. Yet another group reported an optically-pumped (In, Ga)N photonic crystal nanocavity laser emitting at the wavelength of 390 nm [32]. In spite of the fact that photonic crystal structures have the potential for realization of advanced UV lasers, electrically-driven UV photonic crystal laser devices have not yet been developed.

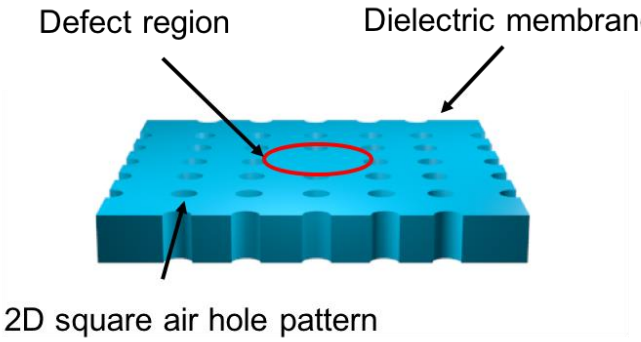

Figure 1-5: Schematic illustration of defect-type 2D patterned dielectric photonic crystal.

1.2 Overview of the thesis

Historically, many research groups have extensively investigated approaches to improving the crystalline quality and efficient doping of GaN-based materials for conventional edge-emitting laser diodes. However, it remains difficult to realize electrically-driven laser diodes operating at the shorter wavelengths, especially in the UVC region. Although many approaches have been proposed and tried, none of them has led to the successful fabrication of reliable, compact, and cost-effective electrically-driven ultraviolet

laser diodes. In this work, we propose and examine a new approach based on photonic crystals which could avoid or alleviate most of the problems of the existing approaches. Even with the new approach, improving p-type doping remains crucial for electrically-driven devices.

The rest of the thesis is organized as follows. In Chapter 2, we will discuss the synthesis of p- and n- type AlGaN films with high doping concentrations grown by plasma-assisted MBE under a liquid-enabled growth mode. This approach is reliable and reproducible for growing high quality device structures that require high-Al-content III-nitrides. On the way to making the ultraviolet lasers, we developed conventional p-i-n heterojunction as well as metal-insulator-semiconductor (MIS) heterostructure light-emitting diodes that emit in the ultraviolet region. The device results are discussed in Chapter 3. In Chapter 4, we discuss the fabrication, characterization, and simulation of advanced ultraviolet photonic crystal nanocavity laser structures, and then compare these to conventional edge-emitting lasers.

In Appendix A, we describe the molecular beam epitaxy process used for growth of the epitaxial films used in this work, and in Appendix B, we will present the fabrication processes and discuss the characterization methods Appendix C used in this work.

1.3 Reference

[1] M. S. Shur and R. Gaska, "Deep-ultraviolet light-emitting diodes," *IEEE Trans. Electron Devices*, vol. 57, pp. 12–25, 2010.

[2] M. Shatalov, W. Sun, and A. Lunev, "Deep-ultraviolet light-emitting diodes with external quantum efficiency higher than 20% at 275nm achieved by improving light-extraction efficiency," *Appl. Phys. Express 10*, vol. 10, p. 31002, 2017.

[3] M. Kneissl, T. Kolbe, J. Schlegel, J. Stellmach, C. Chua, Z. Yang, V. Küller, M. Weyers, and N. M. Johnson, "AlGaN-based Ultraviolet Lasers - Applications and Materials Challenges," *OSA Tech. Dig.*, p. JTuB1, 2011.

[4] H. Yoshida, Y. Yamashita, M. Kuwabara, and H. Kan, "Demonstration of an ultraviolet 336 nm AlGaN multiple-quantum-well laser diode," *Appl. Phys. Lett.*, vol. 93, no. 24, pp. 235–238, 2008.

[5] Y. Taniyasu, M. Kasu, and T. Makimoto, "An aluminium nitride light-emitting diode with a wavelength of 210 nanometres," *Nature*, vol. 441, no. 7091, pp. 325–328, 2006.

[6] C. Stampfl and C. G. Van de Walle, "Theoretical investigation of native defects, impurities, and complexes in aluminum nitride," *Phys. Rev. B*, vol. 65, p. 155212, 2002.

[7] C. G. Van de Walle, C. Stampfl, and J. Neugebauer, "Theory of doping and defects in III–V nitrides," *J. Cryst. Growth*, vol. 189–190, pp. 505–510, 1998.

[8] S. Nakamura, M. Senoh, S. Nagahama, N. Iwasa, T. Yamada, T. Matsushita, Y. Sugimoto, and H. Kiyoku, "Room-temperature continuous-wave operation of InGaN multi-quantum-well structure laser diodes," *Appl. Phys. Lett.*, vol. 69, no. 26, p. 4056, 1996.

[9] M. Kneissl, Z. Yang, M. Teepe, C. Knollenberg, O. Schmidt, P. Kiesel, N. M. Johnson, S. Schujman, and L. J. Schowalter, "Ultraviolet semiconductor laser diodes on bulk AlN," *J. Appl. Phys.*, vol. 101, p. 123103, 2007.

[10] J. Simon, V. Protasenko, C. Lian, H. Xing, and D. Jena, "Polarization-induced hole doping in wide-band-gap uniaxial semiconductor heterostructures.," *Science*, vol. 327, no. 5961, pp. 60–64, 2010.

[11] H. Sun and T. D. Moustakas, "UV emitters based on an AlGaN p-n junction in the form of graded-index separate confinement heterostructure," *Appl. Phys. Express*, vol. 7, p. 12104, 2014.

[12] E. F. Schubert, W. Grieshaber, and I. D. Goepfert, "Enhancement of deep acceptor activation in semiconductors by superlattice doping," *Appl. Phys. Lett.*, vol. 69, no. 24, pp. 3737–3739, 1996.

[13] B. Cheng, S. Choi, J. E. Northrup, Z. Yang, C. Knollenberg, M. Teepe, T. Wunderer, C. L. Chua, and N. M. Johnson, "Enhanced vertical and lateral hole transport in high aluminum-containing AlGaN for deep ultraviolet light emitters," *Appl. Phys. Lett.*, vol. 102, no. 23, p. 231106, 2013.

[14] M. Martens, C. Kuhn, E. Ziffer, T. Simoneit, V. Kueller, A. Knauer, J. Rass, T.

Wernicke, S. Einfeldt, M. Weyers, and M. Kneissl, and M. Citation:Kneissl, "Low absorption loss p-AlGaN superlattice cladding layer for current-injection deep ultraviolet laser diodes," *Appl. Phys. Lett.*, vol. 108, p. 151108, 2016.

[15] Y. Zhang, S. Krishnamoorthy, F. Akyol, A. A. Allerman, M. W. Moseley, A. M. Armstrong, and S. Rajan, "Design of p-type cladding layers for tunnel-injected UV-A light emitting diodes," *Appl. Phys. Lett.*, vol. 109, p. 191105, 2016.

[16] S. Krishnamoorthy, F. Akyol, and S. Rajan, "InGaN/GaN tunnel junctions for hole injection in GaN light emitting diodes," *Appl. Phys. Lett.*, vol. 105, p. 141104, 2014.

[17] T. Oto, R. G. Banal, K. Kataoka, M. Funato, and Y. Kawakami, "100 mW deep-ultraviolet emission from aluminium-nitride-based quantum wells pumped by an electron beam," *Nat. Photonics*, vol. 4, pp. 767–770, 2010.

[18] Y. Shimahara, H. Miyake, K. Hiramatsu, F. Fukuyo, T. Okada, H. Takaoka, and H. Yoshida, "Fabrication of deep-ultraviolet-light-source tube using Si-doped AlGaN," *Appl. Phys. Express*, vol. 4, p. 42103, 2011.

[19] T. Matsumoto, S. Iwayama, T. Saito, Y. Kawakami, F. Kubo, and H. Amano, "Handheld deep ultraviolet emission device based on aluminum nitride quantum wells and graphene nanoneedle field emitters," *Opt. Express*, vol. 20, p. 24320, 2012.

[20] C. Tangtrongbenchasil and K. Nonaka, "Tunable 220 nm UV-C Generation Based on Second Harmonic Generation Using Tunable Blue Laser Diode System," *Jpn. J. Appl. Phys.*, vol. 47, no. 4, pp. 2137–2140, 2008.

[21] A. T. Connie, S. Zhao, S. Sadaf, I. Shih, Z. Mi, X. Du, and J. Lin, “Optical and electrical properties of Mg-doped AlN nanowires grown by molecular beam epitaxy Optical and electrical properties of Mg-doped AlN nanowires grown by molecular beam epitaxy,” *Appl. Phys. Lett.*, vol. 106, p. 213105, 2015.

[22] S. Zhao, X. Liu, S. Y. Woo, J. Kang, G. A. Botton, and Z. Mi, “An electrically injected AlGaN nanowire laser operating in the ultraviolet-C band,” *Appl. Phys. Lett.*, vol. 107, p. 43101, 2015.

[23] K. H. Li, X. Liu, Q. Wang, S. Zhao, and Z. Mi, “Ultralow-threshold electrically injected AlGaN nanowire ultraviolet lasers on Si operating at low temperature.,” *Nat. Nanotechnol.*, vol. 10, pp. 140–144, 2015.

[24] M. Sawicka, G. Muziol, H. Turski, S. Grzanka, E. Grzanka, J. L. Weyher, C. Chèze, R. Kucharski, P. Perlin, C. Skierbiszewski, M. Sawicka, G. Muziol, H. Turski, S. Grzanka, E. Grzanka, M. Albrecht, and R. Kucharski, “Ultraviolet laser diodes grown on semipolar (20-21) GaN substrates by plasma-assisted molecular beam epitaxy,” *Appl. Phys. Lett.*, vol. 251101, pp. 10–14, 2013.

[25] A. Scherer, O. Painter, and J. Vuc, “Defect modes of a two-dimensional photonic crystal in an optically thin dielectric slab,” *J. Opt. Soc. Am. B*, vol. 16, no. 2, pp. 275–285, 1999.

[26] S. Buckley, M. Radulaski, K. Biermann, and J. Vukovi, “Second harmonic generation in photonic crystal cavities in (111) -oriented GaAs Second harmonic generation in photonic crystal cavities in (111) -oriented GaAs,” *Appl. Phys. Lett.*, vol. 103, p.

211117, 2013.

[27] K. Rivoire, S. Buckley, Y. Song, M. L. Lee, and J. Vuckovic, “Photoluminescence from $In_{0.5}Ga_{0.5}As$/GaP quantum dots coupled to photonic crystal cavities,” *Phys. Rev. B*, vol. 85, p. 45319, 2012.

[28] K. Rivoire, A. Faraon, J. Vuckovic, K. Rivoire, A. Faraon, and J. Vuckovic, “Gallium phosphide photonic crystal nanocavities in the visible Gallium phosphide photonic crystal nanocavities in the visible,” *Appl. Phys. Lett.*, vol. 93, p. 63103, 2016.

[29] H. Altug, D. Englund, and J. V. U. Ckovi, “Ultrafast photonic crystal nanocavity laser,” *Nat. Phys.*, vol. 2, no. July, pp. 484–488, 2006.

[30] H. Chen and D. Deppe, “High quality two-dimensional photonic crystal slab cavities,” *Appl. Phys. Lett.*, vol. 79, no. 26, pp. 4289–4291, 2001.

[31] X. Wu, A. Yamilov, X. Liu, S. Li, V. P. Dravid, R. P. H. Chang, and H. Cao, “Ultraviolet photonic crystal laser,” *Appl. Phys. Lett.*, vol. 85, no. 17, pp. 3657–3659, 2004.

[32] T. Wu, P. Weng, Y. Hou, T. Lu, T. Wu, P. Weng, Y. Hou, and T. Lu, “GaN-based photonic crystal surface emitting lasers with central defects GaN-based photonic crystal surface emitting lasers with central defects,” *Appl. Phys. Lett.*, vol. 99, p. 221105, 2011.

Chapter 2 Liquid-metal-enabled synthesis of (Al, Ga)N films by plasma-assisted molecular beam epitaxy

2.0 Introduction

To date, most aluminum-containing nitride films grown by molecular beam epitaxy, up to date suffer from poor crystalline quality and low doping efficiency; these problems hamper development of high performance devices. Optimal growth conditions for high crystalline quality aluminum-containing nitride compounds generally require growth under group-III-rich conditions. On the other hand, to achieve high p-type doping efficiency, without compensating donor defects, requires nitrogen-rich conditions [1]. These conditions are mutually exclusive.

Many studies have now established that aluminum-containing nitride films with smooth surfaces are best grown under metal-rich conditions; nitrogen-rich conditions lead to rough and faceted surface morphologies that are unsuitable for optoelectronic devices. Neugebauer *et al.*, for example, used analytical arguments from density-functional theory and scanning-tunneling microscopy experiments to demonstrate that smooth nitride films can only be achieved under metal-rich growth conditions. Their arguments support the idea that a thin liquid metal layer at the growth front acts as a surfactant that opens up an efficient diffusion channel for lateral adatom transport; this promotes growth of atomically smooth nitride films [2]. Similarly, numerous experimental studies support the notion that presence of excess Ga, which can act as a surfactant, leads to layer-by-layer growth of smooth GaN

films [3, 4]. A negative aspect of the excess liquid Ga is formation of metal droplets; this prevents creation of abrupt heteroepitaxial interfaces in multilayer structures.

Another challenge that has limited development of high performance ultraviolet light sources is low doping efficiency in high-aluminum-containing nitride films. P-type doping of aluminum-containing III-nitrides is complicated by the high activation energy of Mg acceptors in the films. The low incorporation of Mg dopant [5] and the significant tendency for self-compensation is attributed to a presence of donor-like native defects or complexes [6]. It is not yet a settled matter what the optimal MBE growth conditions are for synthesis of AlGaN films with high p-type doping. Most researchers agree that nitrogen-rich conditions are necessary for p-type doping because of the availability of Ga substitutional sites for Mg and the decrease of compensating nitrogen vacancies. The problem however is that under nitrogen-rich conditions, Mg-doped films are likely to be of poor crystalline quality, with rough surfaces. These twin problems make it difficult to synthesize aluminum-rich nitride films that are doped with a high concentration of Mg acceptor impurities and are also of high crystalline quality; overall, there are still no detailed studies on highly doped p-type aluminum-rich AlGaN grown by molecular beam epitaxy.

Recently, Moustakas *et al.* reported experiments and some theoretical analyses of high quality AlGaN/AlN multi-quantum wells with high internal quantum efficiency. They also reported results on GaN films with high p-type doping concentrations of up to 3×10^{18} cm^{-3}. All their samples were grown by plasma-assisted molecular beam epitaxy at extremely high III/V ratios [7]. They suggested that the growth mechanism for their (Al, Ga)N films under the extreme metal-rich conditions was similar to that in conventional liquid phase epitaxy; in effect, the growth could be treated as if it were near thermodynamic equilibrium.

Hoke *et al.* provided additional purely thermodynamic analyses to explain the chemical reactions and the incorporation behavior of group III species and impurities in nitride films under metal-rich growth conditions [8]. They argued that Mg_3N_2, one of the by-products of the reaction, is a stable phase in metal-rich conditions. This chemical reaction is expressed as:

$$3Mg + 2GaN \rightarrow Mg_3N_2 + 2Ga, \qquad \Delta G_{1000k} = -79.3\ kJ/mole$$

However, this appears to contradict available experimental evidence for molecular beam epitaxy. In fact, there are reports in the literature indicating that Mg_3N_2, which causes polarity inversion in III-nitrides, is likely to be formed when there is a high flux of active nitrogen instead [9]. It appears, therefore, that the mere presence of liquid metal during molecular beam epitaxy cannot be easily explained within the thermodynamic equilibrium model because of the low growth temperatures involved, which are far below the thermal equilibrium temperatures for III-nitride compounds.

2.1 Thin film growth mechanisms and associated thermodynamic and dynamic processes

Early quantitative studies of epitaxial thin film growth of semiconductors were largely empirical [10, 11]. It was known then that the driving force for thin film growth was primarily dominated by competition between thermodynamics and kinetics. In the following, we compare and contrast the growth mechanisms for liquid phase epitaxy, dominated by thermodynamics, and molecular beam epitaxy, governed primarily by kinetics.

At its simplest, conventional liquid phase epitaxy is crystallization by cooling and solidification from the liquid (molten) state, where the driving force is the temperature gradient of the cooling along a relevant coordinate. Under the right conditions of chemical equilibrium among mixed crystals in a melt, a crystalline solid can form. For a general $A_xB_{1-x}\mathrm{C}$ ternary compound formed from group-III elements and dimeric group-V molecules in liquid-solid equilibrium, the essential chemical reaction is

$$A_{(l)} + B_{(l)} + C_{(l)} = A_xB_{1-x}\mathrm{C}_{(s)}. \tag{2-1}$$

The phase diagrams that describe the equilibrium conditions are generally determined by consideration of the thermodynamics of the binary systems that form the boundaries of the ternary compound [12]. For the canonical ternary under discussion, the binary systems are *AC*, *BC*, and *AB*. Their deviation from ideality is described in terms of the interaction coefficient

$$\kappa = \frac{\Delta G_m^e}{N_{AC}N_{BC}} = \frac{\Delta H_m - T\Delta S_m^e}{N_{AC}N_{BC}}, \tag{2-2}$$

where ΔG_m^e is the excess free energy of mixing—a form of a fundamental thermodynamic relationship; when normalized by the concentrations N_{AC} and N_{BC} of the binaries *AC* and *BC* in the solution, it is the interaction coefficient. The equilibrium conditions between the solid and liquid phases can be evaluated by relating the interaction parameter, κ, to the activity coefficients, $\gamma_i^{s(l)}$, and the chemical potentials, $\mu_i^{s(l)}$ in the solid and liquid phases. For the canonical three-component compound, the activity coefficient for element *A* is

$$\mathrm{RT}\ln\gamma_A^l = \kappa_{AC}^l\left(N_C^l\right)^2 + \kappa_{AB}^l\left(N_B^l\right)^2 + \left(\kappa_{AC}^l + \kappa_{AB}^l - \kappa_{BC}^l\right)N_B^lN_C^l \tag{2-3}$$

Similar equations for elements B and C can be written down as cyclic permutations of the subscripts. The corresponding chemical potential in the liquid is

$$\mu_A^l(T) = \mu_A^{0l}(T) + RT \cdot \ln(\gamma_A^l N_A), \tag{2-4}$$

and in the solid it is

$$\mu_{AC}^c(T) = \mu_{AC}^{0c}(T) + RT \cdot \ln(x). \tag{2-5}$$

The superscripts l, 0, and c denote, respectively, the liquid state, pure state, and the crystalline solid state; x denotes the fraction of AC in the compound $(AC)_x(BC)_{1-x}$ which is assumed to form a perfect solid solution. A similar equation can be written down for the BC compound. The chemical potential of the pure compound above can be related to the chemical potentials of its constituents in the liquid state by the Vieland formula:[13, 14]

$$\mu_{AC}^{0c}(T) = \mu_A^{sl}(T) + \mu_C^{sl}(T) - \Delta S_{AC}^F(T_{AC}^F - T) - \Delta C_p\left(T_{AC}^F - T - T \cdot ln\left[\frac{T_{AC}^F}{T}\right]\right), \tag{2-6}$$

where ΔS_{AC}^F is the entropy of fusion, ΔC_p is the difference between the specific heat of the compound and its supercooled liquid, and sl denotes a stoichiometric liquid. At equilibrium, the chemical potentials of the crystalline solid and of the constituent elements in the liquid are related to each other by

$$\mu_{AC}^c(T) = \mu_A^l(T) + \mu_C^l(T), \tag{2-7}$$

and

$$\mu_{BC}^c(T) = \mu_B^l(T) + \mu_C^l(T). \tag{2-8}$$

Two basic assumptions undergird the foregoing discussion. The first is that it is possible to dissolve a solute in a liquid solvent; this is the ideality condition. The second is that the processes are near thermodynamic equilibrium. The latter assumption allows one to use Equations (2-4), (2-5), and (2-6) in the relations for the chemical potentials in Equations (2-7) and (2-8), at equilibrium to derive the liquidus surfaces by elimination of x in the resultant equations, and to derive the solidus lines by elimination of the temperature, T. In this type of analysis, one typically neglects the specific heat term [14].

In the usual arrangement of a liquid phase epitaxy system, constituents diffuse vertically because of a concentration gradient in the liquid solution to the growth front where they are incorporated into the growing crystal. The growth rate is diffusion-limited, which endows the liquid phase epitaxy process with a decided advantage in that extremely high growth rates in the range of 0.1 – 1.0 μm/minute are possible. Such growth rates are much higher than what is possible in the typical molecular beam epitaxy process [15], where there is no temperature gradient or vertical diffusion of the constituent species to the growth front. Furthermore, the requirement for high solubility of solutes in bulk solvents cannot be satisfied in the MBE process. For growth of GaN, for example, high solubility of nitrogen in liquid gallium would be required. This solubility can be estimated according to [16]

$$\Delta H_F = RT^2 \frac{dln(x)}{dT} \tag{2-9}$$

where ΔH_F is the melting enthalpy and x is the mole fraction of nitrogen in liquid gallium. Generally, the solubility of nitrogen in gallium would require elevated temperature and pressure conditions. Because of this, it remains a challenge to grow GaN thin films from liquid solutions [19, 20]. Despite the fact that metastable active nitrogen species, such as atomic nitrogen (N), ionic nitrogen (N_2^+), and metastable molecular nitrogen (N_2^*), could improve solubility of nitrogen in liquid Ga [19], this is irrelevant for the molecular beam epitaxy process in its vacuum and low temperature growth environment.

In contrast to liquid phase epitaxy, the MBE process is dominated by surface kinetics. For the nitrides, the growth rate is controlled by the effective arrival rate of the molecular fluxes, substrate temperature, and the interatomic bonding strength. It may usually appear that liquid-metal-assisted molecular beam epitaxy is similar to conventional liquid phase epitaxy because of the presence of a liquid metal layer on the surface. This is in

fact not the case. The metallic film (which is probably only a few atomic monolayers thick) provides a diffusion channel for adatoms which may then find subsurface adsorption sites. In this respect, plasma-assisted molecular beam epitaxy under extreme metal-rich conditions is dominated by adatom kinetics.

2.2 High-aluminum-content AlGaN films and quantum wells grown by molecular beam epitaxy

Aluminum-containing single-layer nitride films and quantum-well heterostructures were grown by plasma-assisted molecular beam epitaxy. The films were investigated *in-situ* using a 10-kV reflection-high-energy-electron diffraction (RHEED) system. All the AlGaN films were grown under extreme metal-rich conditions at substrate temperatures of 770 °C, well above the GaN decomposition temperature (750 °C) [20]. To achieve high crystalline quality epilayers, two special AlN films were grown: the first is a 100-nm AlN buffer layer deposited at a temperature of 800 °C; this is followed by a thin AlN nucleation layer grown at the intermediate temperature of 750 °C before the actual growth of the AlGaN films. Note that the AlN buffer layers were grown under excess aluminum flux, enabling the formation of liquid aluminum at the growth front. During growth of the (Al,Ga)N films, indium flux, which is used as a surfactant, is introduced; this reduces the surface energy and helps to uniformly distribute the liquid metal layer on the growth surface, thus preventing surface roughness of the grown films. The compositions of the $Al_xGa_{1-x}N$ films were determined by HRXRD ω-2θ scans as shown in Figure 2-1 (a). The Al mole fraction (x) is determined from the peak position of the $Al_xGa_{1-x}N$ film shifting from the reference peak position of the AlN ($2\theta = 35.94°$). According to Vegard's law, the calculated compositions are 70%, 58%, and

42% corresponding to Al cell temperatures of 1000°C, 990°C, and 980°C, respectively, for a given growth temperature. In Figure 2-1 (b), the Al mole fraction (x) in $Al_xGa_{1-x}N$ varies almost linearly with Al cell temperature. Low-temperature (77 K) photoluminescence emission spectra of the $Al_xGa_{1-x}N$ films for different Al mole fractions is shown in Figure 2-2. As expected, the sharp emission peaks shift to shorter wavelengths with increasing Al composition, irrespective of the Ga flux as long as there is excess metal flux. Figure 2-3 is a schematic illustration of the action of the constituent species during growth, accompanied by the relevant RHEED pattern in (a); the other illustrations, and the related RHEED patterns in (b) and (c), show a model of what is going on subsequent to closure of the constituent shutters. We observe and note that the RHEED patterns of the $Al_xGa_{1-x}N$ films are visibly dim during the growth. It is believed that the "dimness" of the patterns is due to the presence of an extremely thin liquid metal layer on the growing film surface. It is unlikely that a RHEED pattern would be observable if the metal layer was a thick liquid pool at the growth front; the pristine underlying crystalline order would be inaccessible to the surface electron diffraction process; the electron beam is incident at a glancing angle, with a shallow penetration depth of less than a nanometer [21]. When the constituent fluxes are shut off, while the substrate is maintained at the high growth temperature, very bright and streaky RHEED patterns emerge after only a few minutes as a result of re-evaporation of the thin excess gallium liquid layer from the surface. After this thermal treatment, the grown films were examined under an optical microscope, and were found to be free of any metal droplets on the surface. Figure 2-4 (a) is a schematic illustration of the relative magnitudes of Al, Ga, In, and active nitrogen atomic fluxes during growth of the $Al_xGa_{1-x}N$ films with an Al composition of 42 % and 58 %, respectively. Since the bonding strength of Al-N (11.52

eV/bond) is much higher than that of Ga-N (8.92 eV/bond) and of In-N (7.72 eV/bond) [22], aluminum adatoms were consumed first by the active nitrogen. Any active nitrogen atoms that were not consumed by the Al then react with Ga atoms and the remaining excess Ga and In atoms contribute to the thin liquid layer at the growth surface. As can be seen in Figure 2-4 (b) and (c), the RHEED pattern is brighter for an (Al,Ga)N film with the relatively low Al fraction of 42 % than that for an (Al,Ga)N film with a composition of 58%; this is because of the much thinner liquid layer on the surface of the lower content aluminum. We also note that the growth rate of the liquid-enabled AlGaN films is constant at about 4.2 nm/min, irrespective of the metal fluxes as long as there is excess metal flux. This growth rate is slightly higher than that encountered in stoichiometric and nitrogen-rich growth conditions without the presence of liquid metal for equivalent nitrogen flux as in the liquid metal case. This fact provides evidence that high solubility of solute atoms in extremely thin metal monolayers is not necessary for molecular beam epitaxial growth under metal-rich conditions. If solubility were required under the metal-rich conditions, the growth rate would be much lower than what is observed since it is known that the solubility of nitrogen is negligible in liquid group-III metals. Note that this is in contrast to what the situation is in conventional liquid phase epitaxy where high solubility is crucial. It appears therefore that the chemical reaction that takes place when ternary nitrides are grown under liquid metal conditions by plasma-assisted molecular beam epitaxy may be described by

$$Ga_{(l)} + Al_{(g)} + \frac{1}{2}N^{*}_{2(g)} \rightarrow AlGaN_{(S)}. \tag{2-10}$$

The thin liquid gallium layer on the surface serves the function of a fluid-like surfactant to improve the lateral diffusion of the impinging vapor fluxes by lowering the diffusion

barrier. One can describe the gallium consumption rate during the growth by the first-order rate equation

$$\frac{d\rho}{dt} = -\Gamma_{AlGaN} - \phi_{des} - \frac{dn_{Ga}}{dt}, \tag{2-11}$$

where ρ is the Ga adatom density, Γ_{AlGaN} is the AlGaN growth rate, ϕ_{des} is the Ga desorption rate, and n_{Ga} is the remaining liquid Ga on the surface. This rate equation approximation is a consequence of assuming that the growth rate of the AlGaN film is constant irrespective of the gallium flux whenever excess metal conditions prevail; desorption only occurs at the liquid-vapor interface. In short, the extremely thin metal layer, which is incapable of supporting any temperature gradient on the surface, limits the influence of a thermodynamic driving force. The only reasonable assumption therefore is that growth of nitride films under metal-rich conditions by molecular beam epitaxy is dominated by kinetic processes.

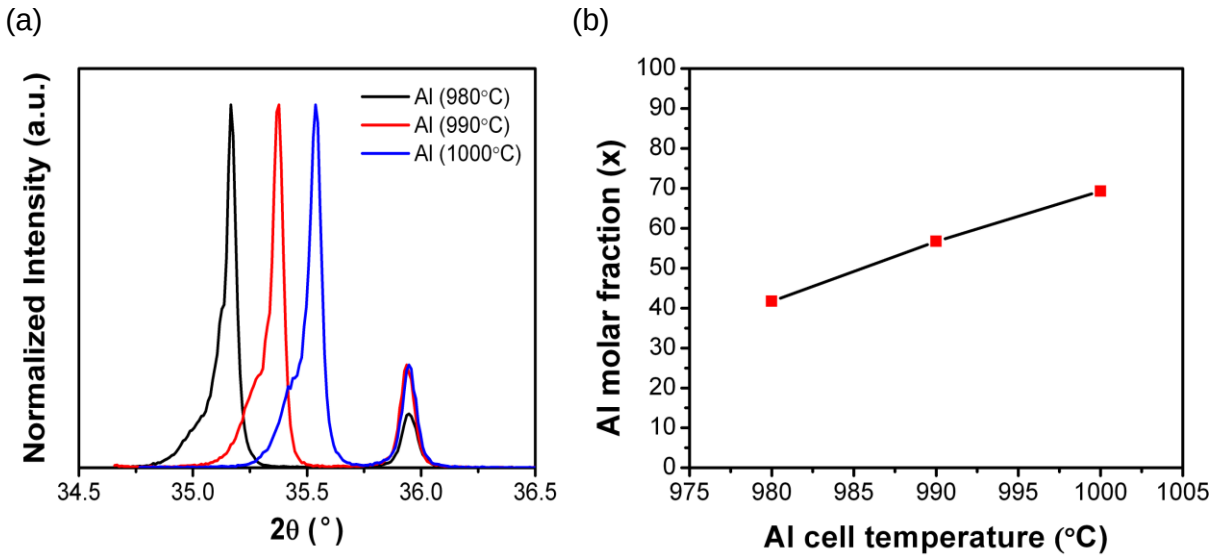

Figure 2-1: (a) The theta-2theta scan of AlGaN films with different Al cell temperatures; (b) The diagram of Al molar fraction of AlGaN changing with the Al cell temperature grown by MBE.

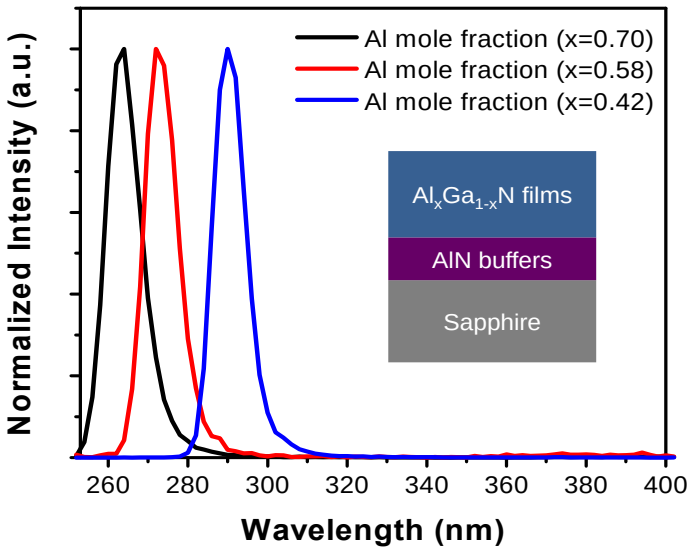

Figure 2-2: Low-temperature (77 K) photoluminescence emission spectra of $Al_xGa_{1-x}N$ films with different Al mole fractions (x).

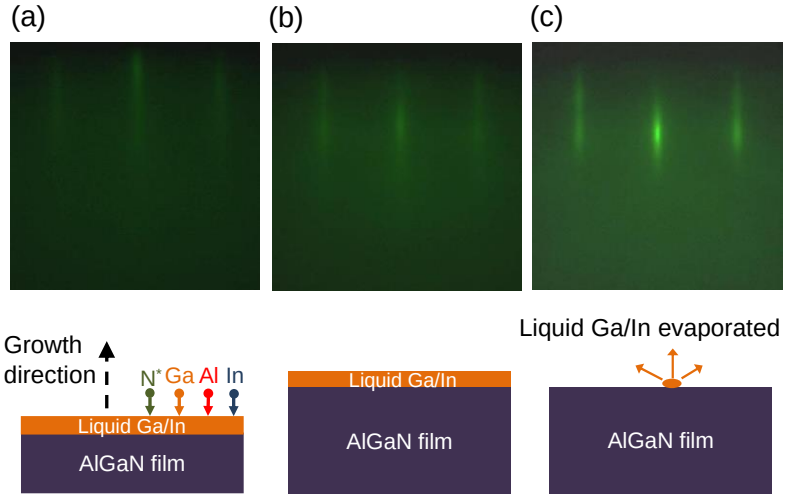

Figure 2-3: Illustration of the liquid-metal-enabled epitaxial growth mechanism. Photographs on top show RHEED patterns emanating from an AlGaN film (a) during the growth, (b) 1 minute and (c) 3 minutes after cell shutters were closed, but with the substrate still at the growth temperature.

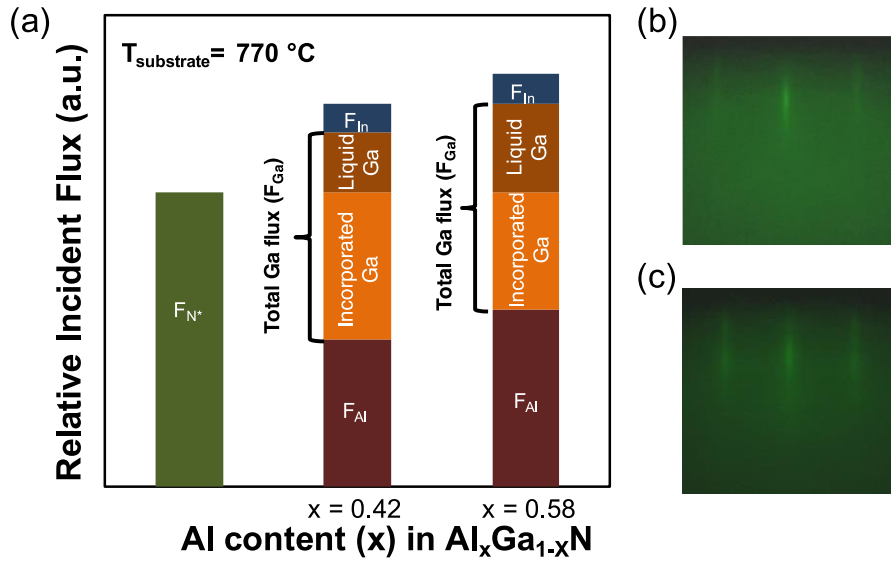

Figure 2-4: A schematic illustration of the relative magnitudes of the Al, Ga, In, and active nitrogen fluxes during growth of $Al_xGa_{1-x}N$ films. The RHEED pattern in (b) is for an $Al_xGa_{1-x}N$ film with Al content of 42%, and (c) is for a film with an aluminum content of 58%.

We also studied the optical and structural characteristics of $Al_xGa_{1-x}N/Al_yGa_{1-y}N$ multiple quantum-well films grown under such metal-rich growth conditions. Five-period $Al_xGa_{1-x}N/Al_yGa_{1-y}N$ quantum-well structures were grown on AlN buffer layers at the growth temperature of 770 °C. The barrier and well widths were estimated, respectively, to be about 8 nm and 2.5 nm. These estimates are based on scanning transmission electron microscopy (STEM) measurements whose micrographs are shown in Figure 2-6 (a). The schematic structure of the films and their corresponding low-temperature (77 K) photoluminescence spectra are shown in Figure 2-5. The strong emission peak at 299 nm in Figure 2-5 (a) originates from the quantum well region of the $Al_{0.7}Ga_{0.3}N/Al_{0.42}Ga_{0.58}N$ structure while the weaker peak at 262 nm is associated with emission from the barrier region. The emission peak is blue-shifted to 286 nm in Figure 2-5 (b) for the

$Al_{0.7}Ga_{0.3}N/Al_{0.58}Ga_{0.42}N$ multi-quantum structure with the higher aluminum composition of the well region as expected. According to Vegard's law, theoretical estimates require higher Al compositions in the AlGaN well regions for the emission peaks to be pushed toward the short wavelength region. Bhattacharyya *et al.* have suggested that this is probably due to compositional inhomogeneity in aluminum-containing films grown under extreme Ga-rich conditions [23]. This is also confirmed by the Z-contrast high angle annular-dark field (HAADF) electron micrograph of the cross-sectional $Al_{0.7}Ga_{0.3}N/Al_{0.58}Ga_{0.42}N$ quantum-well structure. Figure 2-6 (b) of the enlarged image reveals the cluster-like features in the AlGaN well regions that is confirmed by the cross-sectional TEM elemental mapping image as shown in the Figure 2-6. These features could lead to strong localized exciton emission at the minimum of the energy potential, which is illustrated in Figure 2-7. The domination of defect-related nonradiative recombination will be potentially reduced, leading to higher internal quantum efficiency in solid state UV lighting devices. This analogy is similar to what happens due to compositional inhomogeneity in indium-containing nitrides [24]. This compositional inhomogeneity, however, is unlikely to occur from a thermodynamic point of view because there is no miscibility gap in ternary AlGaN compounds; on the other hand, from a growth kinetics point of view, a compositional inhomogeneity could occur due to the difference in adatom mobilities on the growth surface. While this has been experimentally demonstrated in AlGaN films grown by molecular beam epitaxy under nitrogen-rich growth conditions [25, 26], it would still be misleading to assert that growth is dominated by thermodynamics when liquid metal conditions prevail.

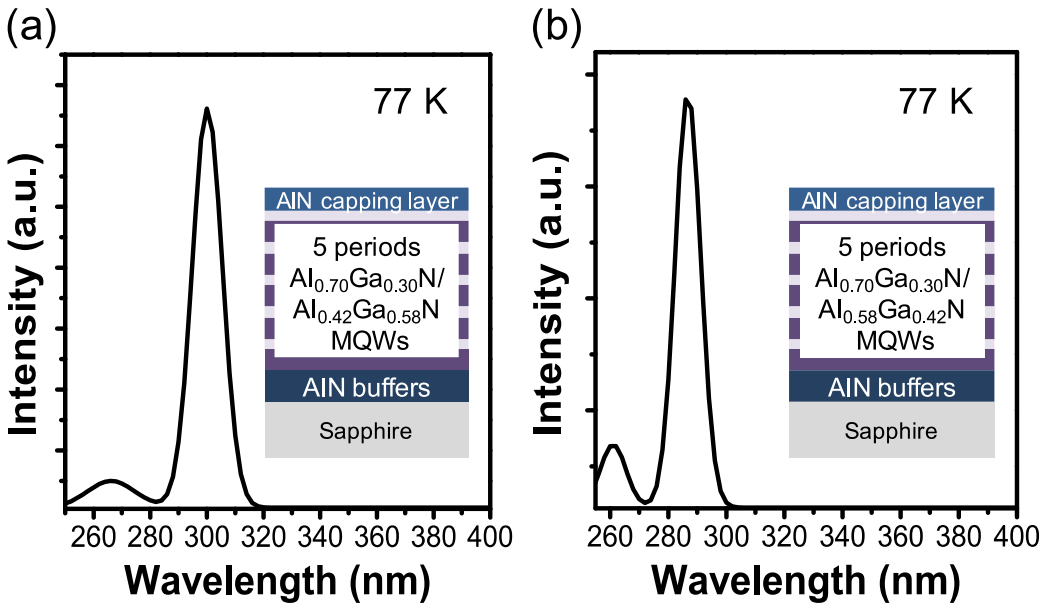

Figure 2-5: The schematic structure and photoluminescence emission spectrum for (a) an $Al_{0.70}Ga_{0.30}N/Al_{0.42}Ga_{0.58}N$ multiple quantum-well structure, and (b) for an $Al_{0.70}Ga_{0.30}N/Al_{0.58}Ga_{0.42}N$ multiple quantum-well structure.

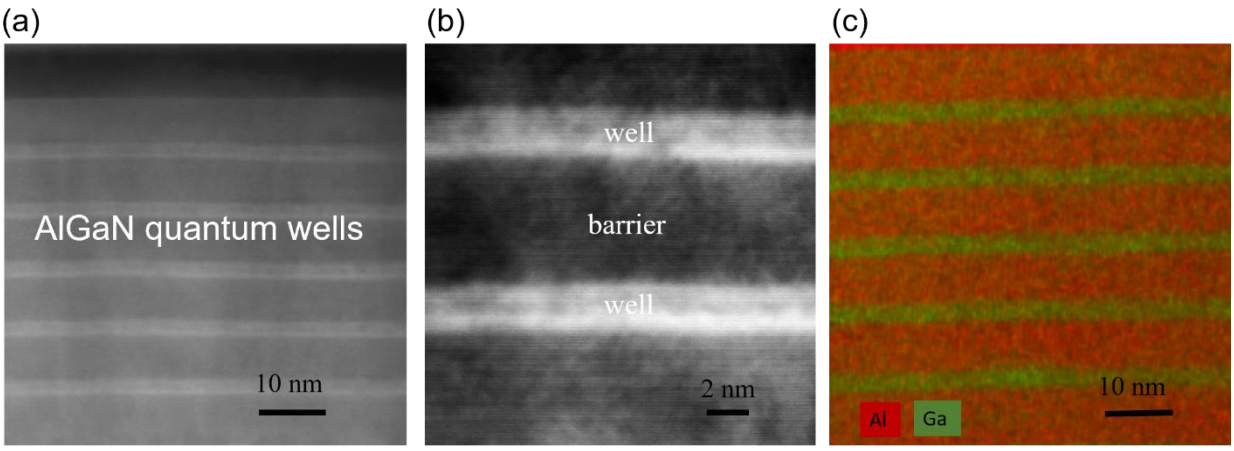

Figure 2-6: (a) Cross-sectional Z-contrast scanning TEM image of $Al_{0.70}Ga_{0.30}N/Al_{0.58}Ga_{0.42}N$ multiple quantum wells. (b) An enlarged version of the image in (a) reveals the cluster-like compositions in the AlGaN quantum wells. (c) Cross-sectional elemental mapping image of $Al_{0.70}Ga_{0.30}N/Al_{0.58}Ga_{0.42}N$ multiple quantum wells.

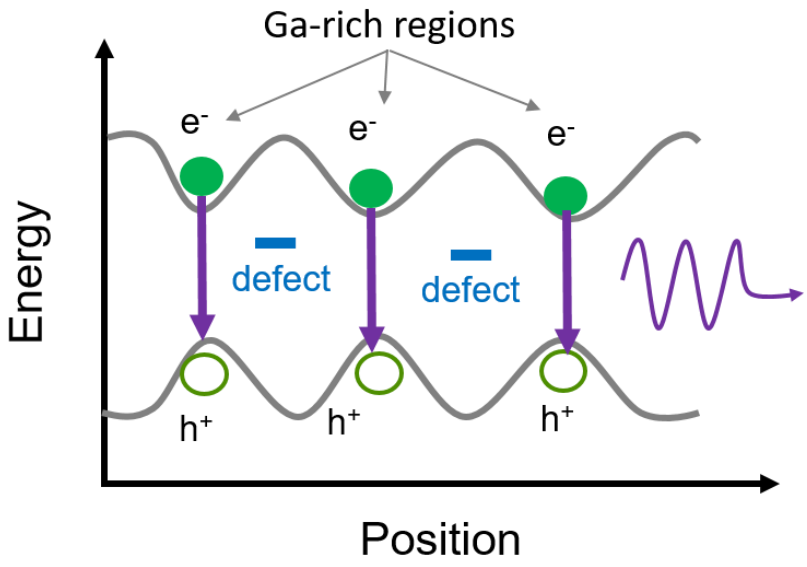

Figure 2-7: The schematic diagram of energy potential on compositional inhomogeneous nitride films, where the potential valley represents Ga-rich regions in (Al, Ga)N films grown under liquid-enabled growth model by molecular beam epitaxy. These potential minima can localize electrons and holes to form localized excitons.

2.3 Highly-doped AlGaN films grown by liquid-metal-enabled growth

To further investigate the range of possibilities under the liquid-metal-rich conditions, we have grown films with intentional dopant impurities. A number of 900-nm thick GaN films doped with Mg were grown on c-plane sapphire substrate; an initial layer of a certain thickness of GaN was grown without Mg, and then the Mg shutter was opened without growth interruption. The thin, initial, unintentionally doped GaN film was grown to prevent inversion of the surface polarity. All doped films were grown under metal-rich conditions at substrate temperatures of 770 °C. The Ga-cell temperature was kept constant at 895°C during the growth; this corresponds to a Ga beam equivalent pressure (BEP) of 8.3 × 10^{-8} Torr in our system. The Mg-cell temperature was varied from 310 – 380 °C. We

emphasize that a thin liquid metal layer was always present on the film surface during the growths in order to enhance the diffusion of impinging adatoms and to avoid polarity inversion. Figure 2-8 shows the carrier types determined from Hall-effect measurements, and the corresponding RHEED patterns for various Mg-cell temperatures (hence fluxes). All films showed streaky RHEED patterns, indicating that the surface structure was covered with Ga with no Mg_3N_2 formed, which would have induced polarity inversion. This further shows that the liquid metal wetting-layer uniformly covers the growth surface. If this were not the case, the RHEED patterns would be spotty because of rough surface morphology caused by the fact that some regions may be terminated by nitrogen atoms. Note that for high Mg fluxes (T_{Mg} > 370 ^{o}C), the samples become n-type probably due to formation of Mg clusters at interstitial sites that contribute to donor-type defects. This conversion causes wider and streaky RHEED patterns as seen in the insets of Figure 2-8 (a). On the other hand, Figure 2-8 (b) shows that p-type GaN films with high hole concentrations of up to the mid 10^{18} cm^{-3} range with low resistivity can be obtained under the liquid metal growth conditions of molecular beam epitaxy. Electrically *active* high hole concentrations of up to 6 × 10^{17} cm^{-3} were also achieved in AlGaN films with Al compositions of up to 70 %. The corresponding secondary ion mass spectrometry (SIMS) result shown in Figure 2-9 indicates that high Mg doping concentrations of up to 5 × 10^{19} cm^{-3} can be achieved in the p-type $Al_{0.7}Ga_{0.3}N$ film. There are a number of reasonable explanations for the high incorporation efficiency. In one scenario, it could be that due to the presence of the thin liquid metal layer on growth surface, the vapor pressure of the Mg buried by the liquid is negligible at the substrate growth temperatures of molecular beam epitaxy. If the surface liquid layer were not there, Mg would otherwise have a higher probability of re-evaporating, making it

difficult to dope aluminum-containing nitrides because of the high vapor pressure of Mg which, at the substrate temperatures of 700 °C, is over 10 mTorr. We would also like to comment that at the growth front, the interface between solid and liquid is at a *kinetic* equilibrium because of the high substrate temperatures used in these experiments. Incorporated gallium is easily re-dissolved to liquid metal because of the weaker Ga-N bond (compared to the stronger Al-N bond); nitrogen on the other hand is difficult to re-sublimate into vacuum due to the thin liquid metal layer on the surface. We thus speculate that the higher probability of desorption of incorporated gallium generates more group-III vacancies that become available for Mg incorporation. This would lead to fewer nitrogen vacancies (V_N) that could act as compensating defects in p-type material when the growth is carried out under extreme metal-rich conditions. With such a high density of Mg atoms incorporated, the Bohr radii of the free holes overlap, allowing the Mg acceptors to interact and form an impurity band rather than a single acceptor level within the band gap. This probably leads to an extended band tail, and thus a lowering of the activation energy as illustrated in Figure 2-10. It then becomes plausible and practical that high p-type doping of Al-rich nitrides is possible because of the reduction of the activation energy when growth is carried out under liquid metal growth conditions.

Under normal circumstances, it is difficult to achieve highly conductive n-type III-nitride alloys that have a high composition of Al in them. Our p-type results on aluminum-containing alloys, discussed in the foregoing, have motivated us to re-examine the prevailing status of n-type, silicon-doped nitrides. We have grown a series of Si-doped (Al, Ga) N films under various conditions on top of an undoped GaN layer, which in turn, was grown on top of an AlN buffer layer as discussed earlier. These films were grown at several Si-cell

temperatures that ranged from 1150 – 1250 °C; streaky RHEED patterns were observed in all cases. We were able to measure high electron concentrations of up to 10^{20} cm^{-3} in both GaN and Al-rich AlGaN fims as shown in Figure 2-11. These data indirectly provide additional evidence that high solubility is not necessary at the extreme metal-rich growth conditions used; this is especially so since silicon exhibits a low solubility of about 2 % at 700 °C in liquid gallium [27]. As already argued in the case for p-type doping, the high n-type concentration of III-nitrides would not be possible if solubility, which is governed by equilibrium thermodynamics, is necessary for liquid-metal-assisted molecular beam epitaxy.

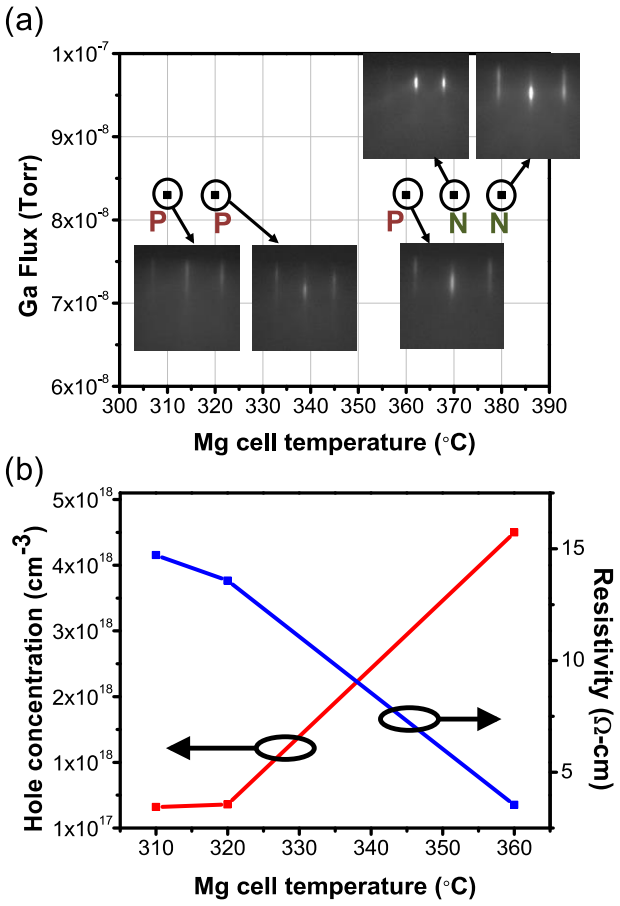

Figure 2-8: (a) Carrier type for Mg-doped GaN films for varying Mg-cell temperatures with the corresponding RHEED patterns shown as insets; (b) Resistivity and hole carrier concentration of Mg-doped GaN films for varying Mg-cell temperatures.

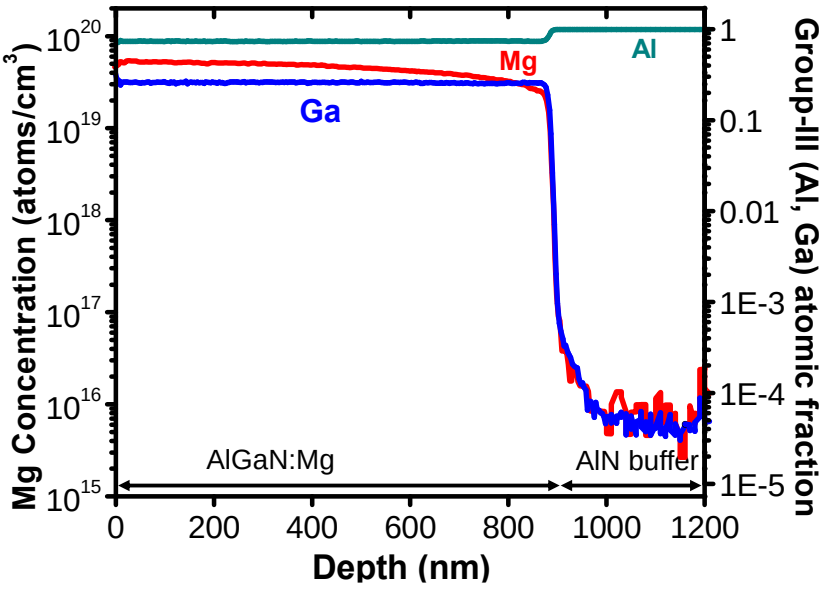

Figure 2-9: Secondary ion mass spectroscopy (SIMS) depth profile for a Mg-doped $Al_{0.7}Ga_{0.3}N$ film.

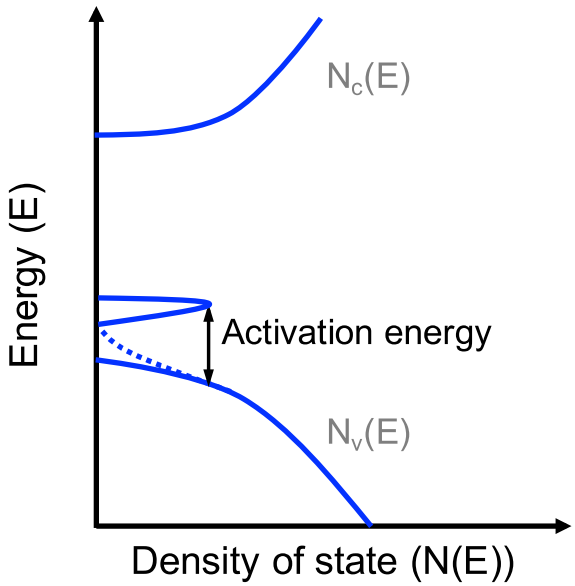

Figure 2-10: Band structure of an (Al,Ga)N structure that is highly doped p-type. The dashed line represents extension of a band tail toward the band-edge which tends to lower the activation energy of dopant impurities in aluminum-containing nitrides.

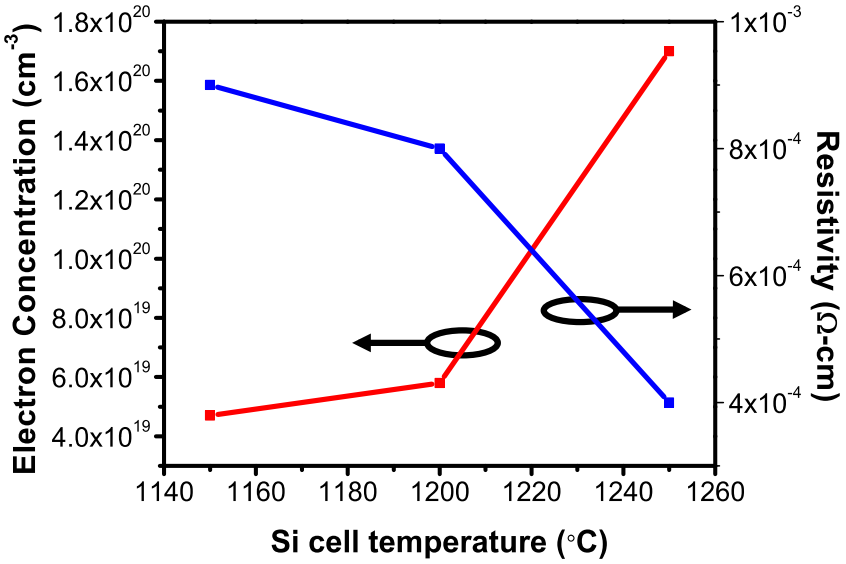

Figure 2-11: Electron carrier concentration and resistivity of Si-doped GaN for varying Si-cell temperatures.

2.4 Study of the activation energy of Mg-doped (Al, Ga)N films

Here, we continue to study the mechanisms for achieving highly-doped (Al,Ga)N films grown by plasma-assisted molecular beam epitaxy under the liquid-metal-enabled growth mode. To characterize Mg-doped (Al,Ga)N films, we carried out temperature-dependent PL measurements. Figure 2-12 (a) shows that the band-edge emission peak of p-type GaN film is located at around 360 nm (3.44 eV). As the temperature decreases, the strong ultraviolet luminescence (UVL) band centered at 379 nm (3.27 eV) becomes intense but without shifting. We attribute this UVL band to the conduction band-to-acceptor band (e-A^0) or shallow donor-acceptor-pair (DAP) transitions. It is worth noting that the Mg-doped GaN film are free of nitrogen vacancies (V_N) or related complexes because such self-compensated defect complexes would be attributed to deep donor-acceptor pair (DAP)

recombination, which is associated with a blue luminescence (BL) band at around 2.8 eV [28]. This BL band does not occur in our PL spectra. Another weak emission feature in the PL spectra is at around 390 nm (3.18 eV); this is attributed to longitudinal-optical (LO) phonon replicas, which are associated with the interaction between bound excitons and LO phonons.

We also performed the temperature-dependent PL experiments on Mg-doped AlGaN films with Al concentration of up to 70%; the data is shown in Figure 2-12 (b). The band-edge emission is located at 265 nm (4.68 eV); the emission at 307 nm (4.04 eV) is associated with donor-acceptor-pair (DAP) transitions. This can be inferred from the fact that the broad UVL band gradually shifts to longer wavelengths as temperature of the sample is increased. This is probably because photo-generated electrons initially captured by neutral shallow donor levels are excite into the conduction band at elevated temperatures, but only few bound holes can be ionized to the valence band because of the relatively higher ionization energy (> 26 meV) at room temperature.

The thermal activation energy of Mg acceptors in p-type (Al, Ga)N films can be determined from the Arrhenius formula

$$I(T) = \frac{I(0)}{1 + \alpha \cdot \exp(-E_a/kT)} \tag{2-12}$$

where $I(T)$ represents the PL intensity at temperature of T, $I(0)$ is the PL intensity as the sample temperature approaches zero Kelvin, E_a is the activation energy of the acceptors, and k is the Boltzmann constant. The parameter α is defined as the rate constant $\alpha = \tau_R/\tau_0$, where τ_R is the radiative lifetime of carriers, and τ_0 is the nonradiative lifetime constant of the carriers. The temperature-dependence of thermal quenching of the UV emission intensity can be fitted by using Equation (2-12). The fitted curves for p-type GaN and p-type

$Al_{0.7}Ga_{0.3}N$ are shown in Figure 2-13 (a) and (b), respectively. As temperature decreases, the PL intensity remains relatively constant because negligible acceptors are activated at cryogenic temperatures. We estimated that the activation energies as determined by the slope of curves are 128.3 meV for GaN and 220.1 meV for the high-Al-content $Al_{0.7}Ga_{0.3}N$, respectively. Compared to theoretical results in the literature [29, 30], these activation energies are drastically lower for both p-type GaN and p-type $Al_{0.7}Ga_{0.3}N$ grown by the liquid-metal-enabled molecular beam epitaxy. We have further studied the temperature-dependent PL spectra and noticed that the full width of half maximum (FWHM) of UVL bands are estimated to be 206 meV in p-type GaN and 146 meV in p-type $Al_{0.7}Ga_{0.3}N$ films, respectively. These broad UVL bands provide evidence that the energy levels of Mg acceptors overlap and interact to form an acceptor band at high Mg incorporations. As a result, the reduction of the thermal activation energies can be attributed to significantly broadened Mg energy levels and to a band tailing effect that effectively leads to hole hopping conduction in the impurity band.

In summary, we have provided experimental evidence to demonstrate that aluminum-containing III-nitride films with high crystalline quality and high doping efficiency can be synthesized by plasma-assisted molecular beam epitaxy under extremely metal-rich growth conditions dominated by *kinetics*.

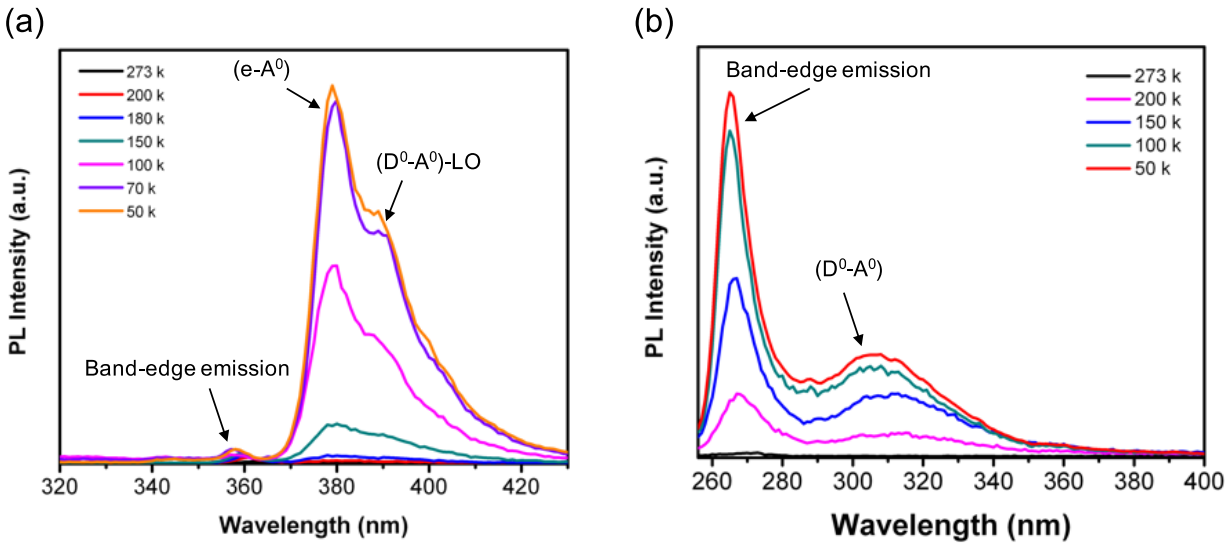

Figure 2-12: Temperature-dependent PL spectra of (a) Mg-doped GaN film (b) Mg-doped $Al_{0.7}Ga_{0.3}N$ film grown by plasma-assisted molecular beam epitaxy.

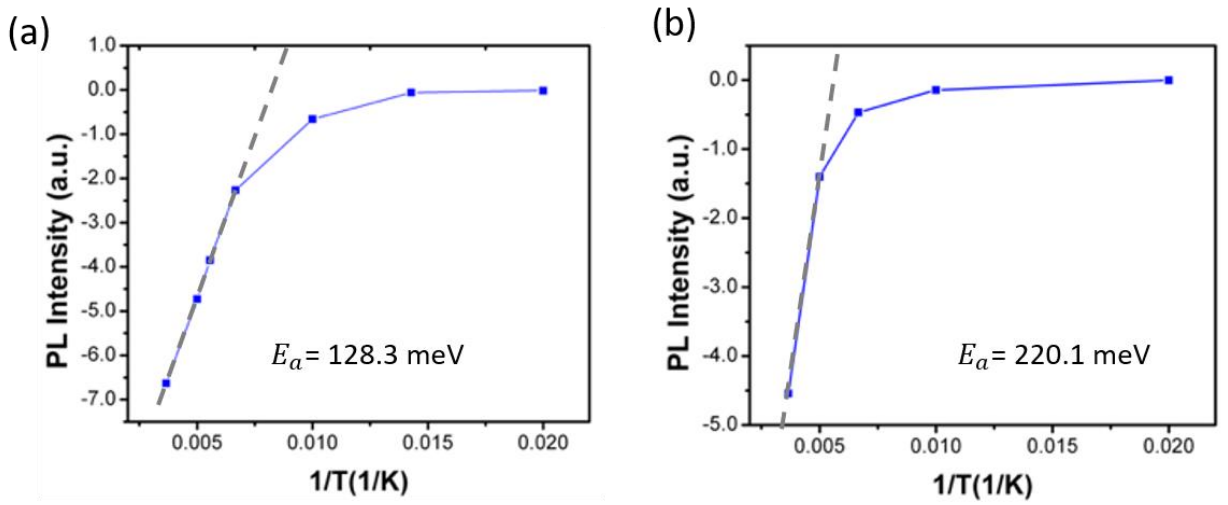

Figure 2-13: Temperature dependence of the PL intensity of ultraviolet luminescence band on (a) Mg-doped GaN and (b) Mg-doped $Al_{0.7}Ga_{0.3}N$.

2.5 Reference

[1] C. Stampfl and C. G. Van de Walle, “Theoretical investigation of native defects, impurities, and complexes in aluminum nitride,” *Phys. Rev. B*, vol. 65, p. 155212, 2002.

[2] J. Neugebauer, T. K. Zywietz, M. Scheffler, J. E. Northrup, H. Chen, and R. M. Feenstra, “Adatom Kinetics On and Below the Surface: The Existence of a New Diffusion Channel,” *Phys. Rev. Lett.*, vol. 90, no. 5, p. 56101, 2003.

[3] G. Mula, C. Adelmann, S. Moehl, J. Oullier, and B. Daudin, “Surfactant effect of gallium during molecular-beam epitaxy of GaN on AlN (0001),” *Phys. Rev. B*, vol. 64, p. 195406, 2001.

[4] G. Koblmuller, S. Fernández-Garrido, E. Calleja, and J. S. Speck, “In situ investigation of growth modes during plasma-assisted molecular beam epitaxy of (0001) GaN,” *Appl. Phys. Lett.*, vol. 91, no. 1, p. 161904, 2007.

[5] T. Zheng, W. Lin, D. Cai, W. Yang, W. Jiang, H. Chen, J. Li, S. Li, and J. Kang, “High Mg effective incorporation in Al-rich $Al_XGa_{1-X}N$ by periodic repetition of ultimate V/III ratio conditions.,” *Nanoscale Res. Lett.*, vol. 9, no. 1, p. 40, 2014.

[6] C. A. Hurni, J. R. Lang, P. G. Burke, and J. S. Speck, “Effects of growth temperature on Mg-doped GaN grown by ammonia molecular beam epitaxy,” *Appl. Phys. Lett.*, vol. 101, no. 10, p. 102106, 2012.

[7] T. D. Moustakas and A. Bhattacharyya, “The role of liquid phase epitaxy during growth of AlGaN by MBE,” *Phys. Status Solidi*, vol. 9, no. 3–4, pp. 580–583, 2012.

[8] W. E. Hoke, a. Torabi, J. J. Mosca, and T. D. Kennedy, “Thermodynamic analysis of

cation incorporation during molecular beam epitaxy of nitride films using metal-rich growth conditions," *J. Vac. Sci. Technol. B Microelectron. Nanom. Struct.*, vol. 25, no. 3, p. 978, 2007.

[9] V. Ramachandran, R. M. Feenstra, W. L. Sarney, L. Salamanca-Riba, J. E. Northrup, L. T. Romano, and D. W. Greve, "Inversion of wurtzite GaN(0001) by exposure to magnesium," *Appl. Phys. Lett.*, vol. 75, no. 6, p. 808, 1999.

[10] T. Y. Wu and G. L. Pearson, "Phase diagram, crystal growth, and band structure of InGaAs," *J. Phys. Chem. Solids*, vol. 33, p. 409, 1972.

[11] G. A. Antypas and R. L. Moon, "Growth and characterization of InGaAsP–InP lattice-matched heterojunctions," *J. Electrochem. Soc.*, vol. 120, p. 1574, 1973.

[12] M. B. Panish, "Phase equilibria in the system Al-Ga-As-Sn and electrical properties of Sn-doped liquid phase epitaxial $Al_xGa_{1-x}As$," *J. Appl. Phys.*, vol. 44, no. 6, p. 2667, 1973.

[13] M. Ilegems and G. L. Pearson, "Derivation of the Ga-Al-As ternary phase diagram with applications to liquid phase epitaxy," *Symp. GaAs*, pp. 3–10, 1968.

[14] L. J. Vieland, "Phase equilibria of III-V compounds," *Acta Metall.*, pp. 137–142, 1963.

[15] B. M. McSkimming, C. Chaix, and J. S. Speck, "High active nitrogen flux growth of GaN by plasma assisted molecular beam epitaxy," *J. Vac. Sci. Technol. A*, vol. 33, no. 5, p. 05E128, 2015.

[16] J. M. Prausnitz, *Molecular thermodynamics of fluid-phase equilibria, second edition*. New Jersey: Printice-Hall, 1986.

[17] J. S. Dyck, K. Kash, M. T. Grossner, C. C. Hayman, A. Argoitia, N. Yang, M. H.

Hong, M. E. Kordesch, and J. C. Angus, “Growth of oriented thick films of gallium nitride from the melt,” *Mrs Internet J. Nitride Semicond. Res.*, vol. 537, p. G3.23, 1999.

[18] S. V. Novikov and C. T. Foxon, “Plasma-assisted electroepitaxy of GaN layers from the liquid Ga melt,” *J. Cryst. Growth*, vol. 354, no. 1, pp. 44–48, 2012.

[19] N. Newman, “The energetics of the GaN MBE reaction: a case study of meta-stable growth,” *J. Cryst. Growth*, vol. 178, no. 1–2, pp. 102–112, 1997.

[20] S. W. Kaun, M. H. Wong, U. K. Mishra, and J. S. Speck, “Molecular beam epitaxy for high-performance Ga-face GaN electron devices,” *Semicond. Sci. Technol.*, vol. 28, no. 7, p. 74001, 2013.

[21] K. Rabe, C. Ahn, and J. M. Triscone, *Physics of Ferroelectronics: A Modern Perspective*, vol. 105. Heidelberg: Sprin, 2007.

[22] R. J. Shul, R. D. Briggs, S. J. Pearton, C. B. Vartuli, and C. R. Abernathy, “Chlorine-based Plasma Etching of GaN,” *Mat. Res. Soc. Symp. Proc.*, vol. 449, no. 1, pp. 969–980, 1997.

[23] A. Bhattacharyya, T. D. Moustakas, L. Zhou, D. J. Smith, and W. Hug, “Deep ultraviolet emitting AlGaN quantum wells with high internal quantum efficiency,” *Appl. Phys. Lett.*, vol. 94, pp. 25–27, 2009.

[24] S. F. Chichibu, A. Uedono, T. Onuma, B. A. Haskell, A. Chakraborty, T. Koyama, P. T. Fini, S. Keller, S. P. DenBaars, J. S. Speck, U. K. Mishra, S. Nakamura, S. Yamaguchi, S. Kamiyama, H. Amano, I. Akasaki, J. Han, and T. Sota, “Origin of defect-insensitive emission probability in In-containing (Al,In,Ga)N alloy semiconductors,” *Nat. Mater.*, vol. 5, no. 10, pp. 810–816, 2006.

[25] A. Pierret, C. Bougerol, M. Den Hertog, B. Gayral, M. Kociak, H. Renevier, and B. Daudin, “Structural and optical properties of $Al_XGa_{1-x}N$ nanowires,” *Phys. Rev. B*, vol. 7, no. 10, pp. 868–873, 2013.

[26] M. Sawicka, C. Chèze, H. Turski, J. Smalc-Koziorowska, M. Kryško, S. Kret, T. Remmele, M. Albrecht, G. Cywiński, I. Grzegory, and C. Skierbiszewski, “Growth mechanisms in semipolar (20-21) and nonpolar m plane (10-10) AlGaN/GaN structures grown by PAMBE under N-rich conditions,” *J. Cryst. Growth*, vol. 377, p. 184, 2013.

[27] P. H. Knck and J. Broder, “The solubility of silicon and germanium in gallium and indium,” *Phys. Rev. Lett.*, vol. 90, p. 521, 1953.

[28] U. Kaufmann, M. Kunzer, M. Maier, H. Obloh, A. Ramakrishnan, B. Santic, and P. Schlotter, “Nature of the 2.8 eV photoluminescence band in Mg doped GaN,” *Appl. Phys. Lett.*, vol. 72, no. 11, pp. 1326–1328, 1998.

[29] Y. Taniyasu, M. Kasu, and T. Makimoto, “An aluminium nitride light-emitting diode with a wavelength of 210 nanometres,” *Nature*, vol. 441, no. 7091, pp. 325–328, 2006.

[30] H. X. Jiang and J. Y. Lin, “Hexagonal boron nitride for deep ultraviolet photonic devices,” *Semicond. Sci. Technol.*, vol. 29, no. 8, p. 84003, 2014.

Chapter 3

Ultraviolet light-emitting diodes

After successful achievement of high p-type and n-type doping and high quality multi-quantum wells, we have attempted to integrate these elements to create light-emitting devices. In addition to conventional AlGaN-based PIN heterostructures, we have also examined a metal-insulator-semiconductor (MIS) type of diode to clarify the conduction and emission mechanisms in ultraviolet LEDs.

3.1 Ultraviolet light-emitting diodes based on PIN heterostructures

Figure 3-1 shows a schematic structure of the UV LED epilayers and the corresponding band diagram. This band diagram, which is for a forward-biased condition, was created using a commercial software called SiLEDSe, which implements a one-dimensional drift-diffusion model that accounts for specific features of the nitride materials, such as strong piezoelectricity and spontaneous polarization. Prior to fabricating the UV LEDs, we performed such simulations to optimize the parameters and dimensions of the quantum wells and the p-type dopant density in the III-nitride layers for high current injection efficiency and internal quantum efficiency. Following this optimization, we synthesized typical LED structures which are comprised of 0.2 μm of an AlN buffer layer on top of a 30-nm thick AlN nucleation layer on a sapphire substrate; these buffer layers were grown by plasma-assisted molecular beam epitaxy. They are followed by 10 periods of an AlGaN/AlN (3 nm/ 3 nm) short period superlattice (SPSL) before deposition of the Si-doped $Al_{0.7}Ga_{0.3}N$ cladding layer. The purpose of the superlattice is to relieve strain. The composition of the AlGaN layer in the superlattice is the same as that of the Si-doped

AlGaN cladding layer. Following growth of the n-AlGaN cladding layer, an active region consisting of 5 periods of $Al_{0.58}Ga_{0.42}N/Al_{0.70}Ga_{0.30}N$ quantum wells, each with a thickness of 2 nm is grown. The active region is followed by a 10-nm Mg-doped $Al_{0.8}Ga_{0.2}N$ electron-blocking layer. The thickness of the barrier layer close to the n-type AlGaN cladding layer is 10 nm, while the other barrier layer close to the electron blocking layer is 7 nm. Such an asymmetric quantum well design is used to balance the electron and hole injections since electrons and holes have different diffusion lengths. The entire structure is capped with 150-nm thick p-type $Al_{0.7}Ga_{0.3}N$ contact layer. The quantum wells were grown under metal-rich conditions to allow formation of uniform and compositionally homogeneous layers. The n-type AlGaN cladding layer was also grown under the same conditions to enable an atomically smooth surface for growing subsequent quantum wells, while the p-type AlGaN cladding layers were grown under extreme Ga-rich conditions to prevent three-dimensional island growth as well as to achieve high doping efficiency (as described in previous chapters).

Light-emitting diodes were then fabricated by a standard photolithographic process, illustrated in Figure 3-2. Figure 3-3 schematically shows the fabrication steps for ultraviolet light-emitting diodes. The as-grown samples were first patterned so that an n-type electrode could be deposited. The patterning is done using Cl_2-based inductively coupled plasma reactive-ion etching (ICP - RIE) to define the n-contact mesa. The etch rate for the $Al_{0.7}Ga_{0.3}N$ layer using Cl_2 (25 sccm)/ BCl_3 (5 sccm)/ Ar (70 sccm) gases was estimated to be about 230 nm/min. The n-type electrode was then annealed in forming gas to achieve an ohmic contact. After that, a thin p-type current spreading layer and a thick p-type contact pad were deposited by electron-beam evaporator on the p-type (Al, Ga)N. The deposited p-

type contact was then annealed. The last step was the etching of the mesa to isolate each LED device.

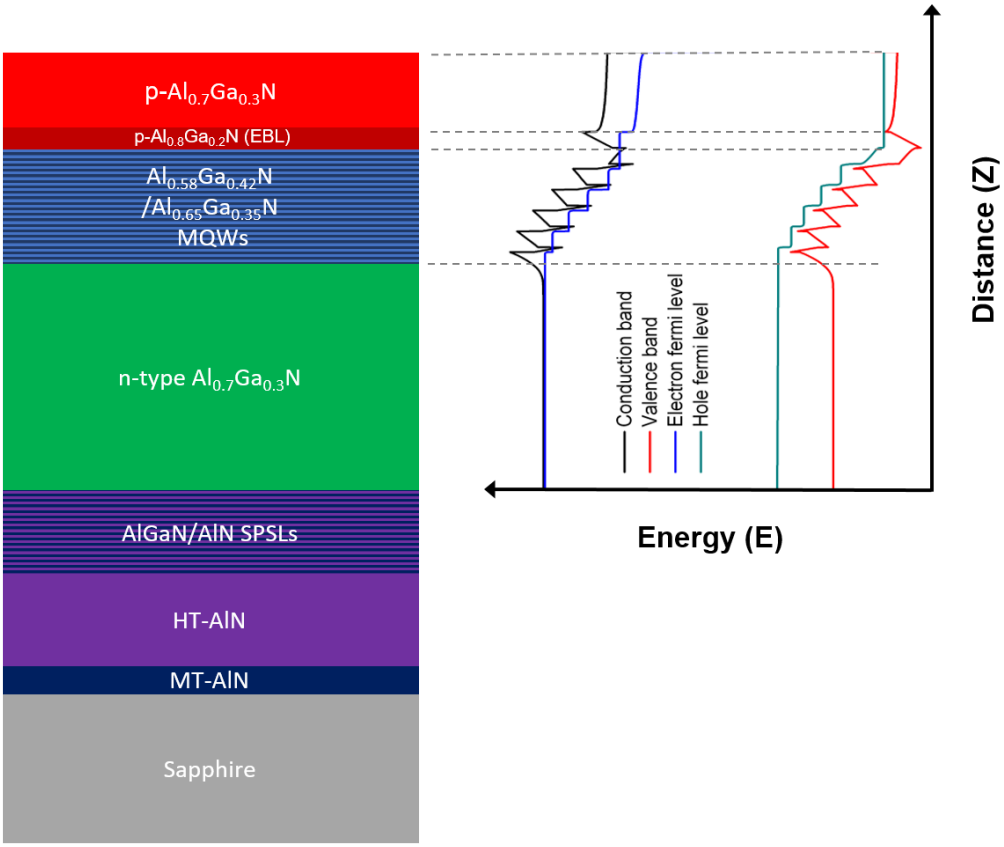

Figure 3-1: The schematic structure of LED epitaxial layers and the corresponding band diagram simulated by the commercial software, SiLENSe.

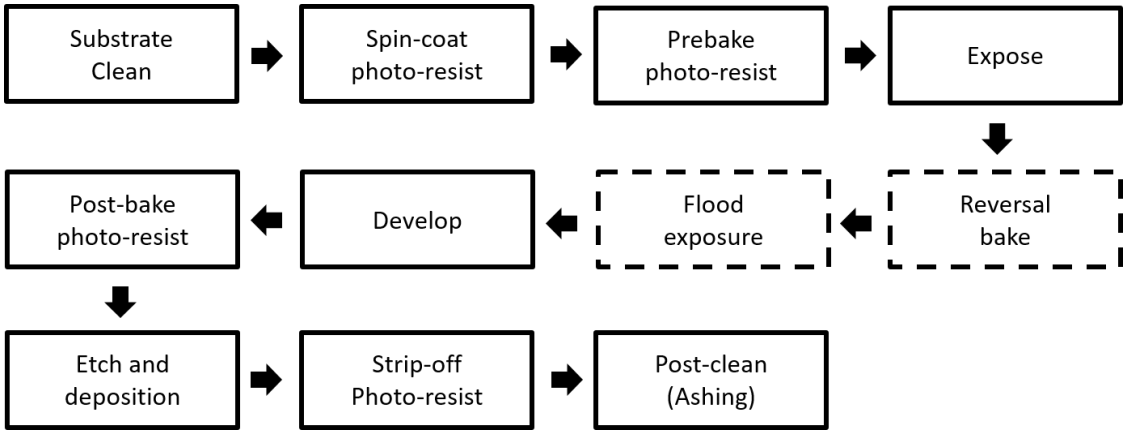

Figure 3-2: Process flow of photolithography

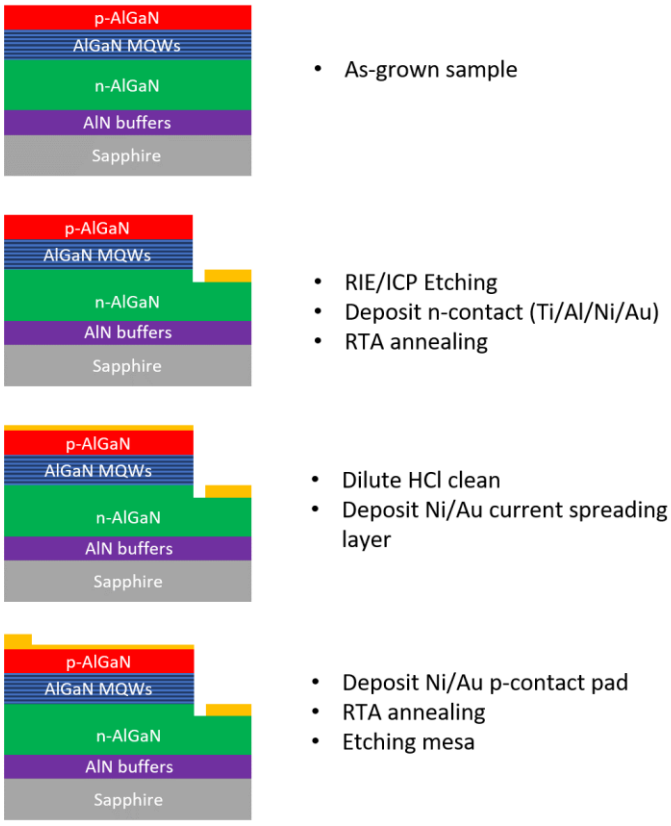

Figure 3-3: The schematic illustration of LED micro-fabrication.

3.1.1 Current-voltage characterization of the UV LEDs

3.1.1.1 Evaluation of the quality of the contacts

The transmission line method (TLM) was used to characterize the quality of the contacts. A general diagram of the TLM structure is shown in Figure 3-4 (a). Fixed dimensions for the metal contact bars with lengths of W separated from each other with distances L were designed to determine the specific contact resistance. The total resistance (R_T) is given by

$$R_T = \frac{R_{sh}L}{W} + 2R_C \approx \frac{R_{sh}L}{W} + \frac{2R_{shc}L_T}{W} \quad (3\text{-}1)$$

where R_{sh} is the sheet resistance of the doped semiconductor layer, R_C is the contact resistance which can be expressed as $R_C \approx \frac{R_{shc}L_T}{W}$. R_{shc} is the sheet resistance under the contact, and $L_T = (\rho_c/R_{shc})^{1/2}$ is the transfer length. The total resistance (R_T) for various contact separations can be plotted as functions L as shown in Figure 3-4 (b). The sheet resistance of the doped semiconductor can then be determined from the slope (R_{sh}/W) of the plot, while the contact resistance (R_C) can be obtained from the intercept at $L = 0$. The intercept at $R_T = 0$ gives $2L_T$.

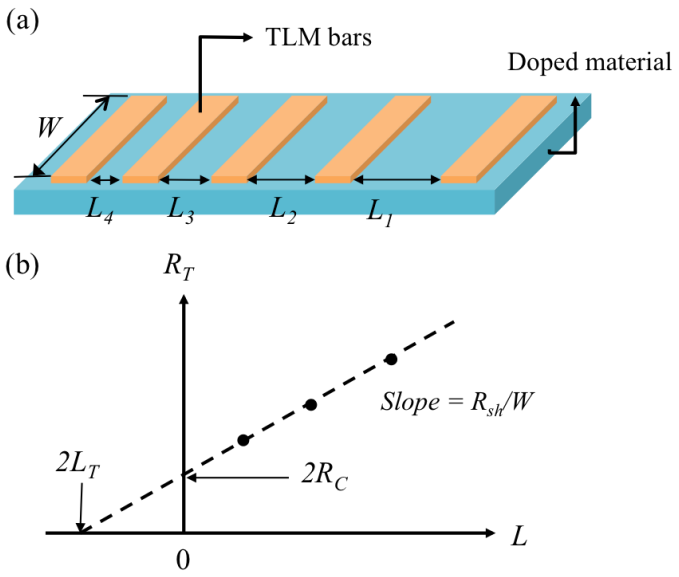

Figure 3-4: (a) The schematic diagram of TLM measurement (b) The plot of total resistance as function of contact spacing.

3.1.1.2 Formation and measurement of the n-type contact

The n-type ohmic contact for the deep UV LEDs fabricated in this work was based on the following combination of metals: Ti/Al/Ni/Au (20nm/100nm/40nm/50nm). Figure 3-5 (a) shows the current-voltage characteristic of an n-type AlGaN layer with a high AlN mole fraction of 70 %; as can be seen, this contact is approximately linear and hence ohmic after annealing at 900 °C in an ambient of forming gas for 30 secs. The corresponding TLM result for the n-type contact is shown in Figure 3-5 (b). From the plot, the contact resistance is 0.45 kΩ, while the calculated sheet resistance is 6 kΩ/□

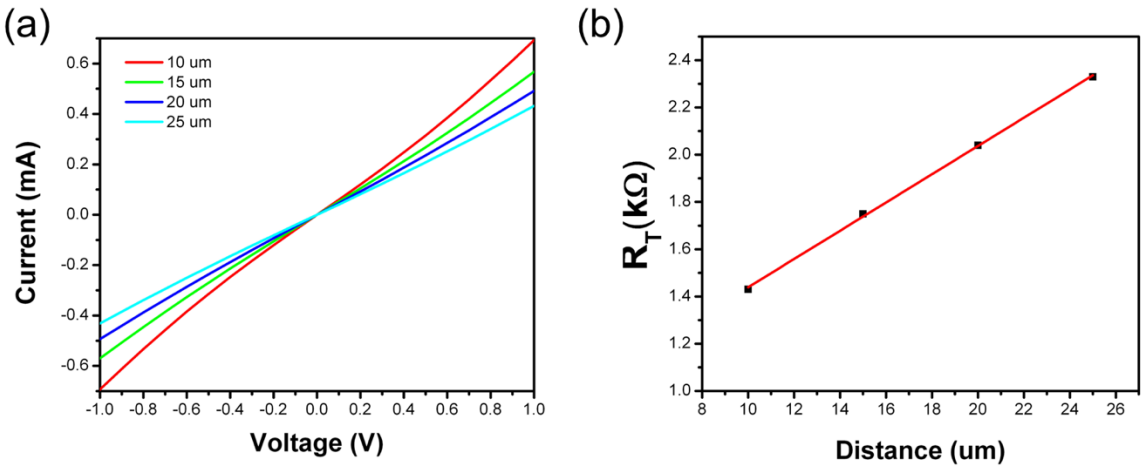

Figure 3-5: (a) I-V characterization of n-AlGaN with Ti/Al/Ni/Au contact annealing at 900 °C in N_2 ambient for 30 secs. (b) The TLM plot of Ti/Al/Ni/Au n-contact.

3.1.1.3 Formation and measurement of the p-type contact

Forming a p-type contact is a challenge for two main reasons: first, it is difficult to achieve high conductivity in high-Al-content AlGaN, and second, identifying metals with the proper (high) work functions is still an open problem. In this work, we used Ni/Au (20nm/100 nm), which are the best combination of metals for p-type contact. The deposited contact was annealed at 500 °C in air for 3 minutes. Figure 3-6 shows the I-V characteristic for such a p-type contact; the behavior approximately linear and hence ohmic as in the case for the n-type contact.

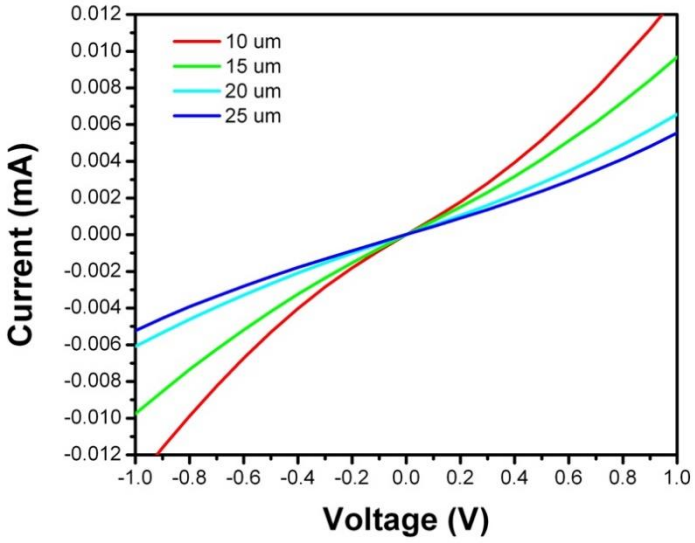

Figure 3-6: I-V characterization of p-type AlGaN with Ni/Au contact annealing at 500 °C in air ambient for 3 min.

3.1.1.4 Current-Voltage (I-V) characterization of prototype deep UV LEDs

A current-voltage (I-V) characteristic of a LED with mesa dimensions of 500 × 500 μm^2 is shown in Figure 3-7. The device exhibits a rectifying behavior and a turn-on voltage of approximately 7 V. The I-V characteristic of a conventional forward-biased diode is given by

$$I - \frac{(V - IR_S)}{R_P} = I_S \cdot exp\left[\frac{e(V - IR_S)}{nkT}\right] \quad (3\text{-}2)$$

where R_P is the resistance in parallel with the current paths or channels in the p-n junction, and R_S is a series resistance attributed to excessive contact resistance or to the resistance of the neutral regions. The diode turn-on voltage is made up of a distributed range of voltages rather than being a single value due to parasitic resistances for each diode. In highly doped

semiconductors, the turn-on voltage in general, can be approximated by the bandgap energy divided by the elementary charge, $V_{turn-on} \approx E_g/e$. However, it is generally higher for III-nitride-based LEDs due to the following reasons. First, large bandgap discontinuities occur in the nitride system; these cause additional voltage drops. Second, high contact resistances in these materials can cause additional voltage drops at the ohmic contacts. Lastly, high parasitic contact resistances can occur in the nitride layers themselves.

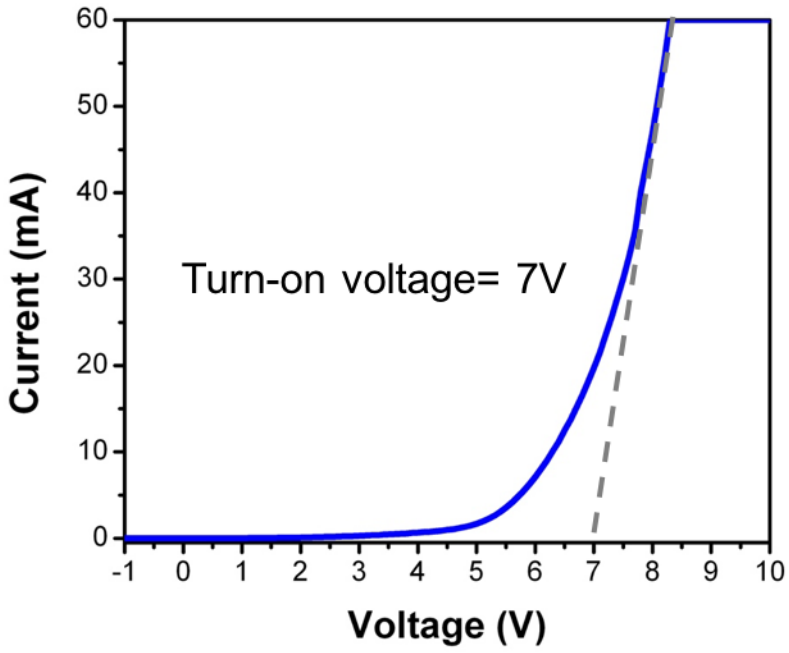

Figure 3-7: I-V characteristics of a deep UV LED device emitting at 274 nm.

3.1.2 Optical characterization of the UV LEDs

The electroluminescence (EL) spectra of deep UV LEDs whose typical die size is 500 µm × 500 µm are illustrated in Figure 3-8. These spectra were measured under various dc current injection levels from 10 mA to 25 mA using a calibrated integrated sphere at room

temperature. The near band-edge emission is located at 274 nm with a narrow FWHM of 11 nm. The optical output power of this device under continuous current injection is shown in Figure 3-9. The output power begins to saturated at 0.76 mW at a current of 30 mA CW probably due to heating. The corresponding external quantum efficiency (EQE) and wall-plug efficiency (WPE) is estimated to be about 0.56 % and 0.35%, respectively. This external quantum efficiency is rather high compared to state-of-the-art UV LEDs grown by molecular beam epitaxy [1]. The relatively high value is attributed to the successful achievement of n-type and particularly p-type doping and in high quality aluminum-rich AlGaN films. As illustrated in Figure 3-10, utilizing Al-rich AlGaN as a p-type contact layer enable to enhance the light extraction to free space due to the inhibition of UV light absorption. In addition, p-AlGaN with a large band gap serves as a thick barrier to prevent electrons effusion out of the quantum-well region; most importantly, it can significantly reduce the barrier height (E_B) for injecting holes from a p-type layer to an active layer. Cumulatively, p-type AlGaN with high aluminum mole fractions can increase overall carrier injection efficiency of a deep ultraviolet LED.

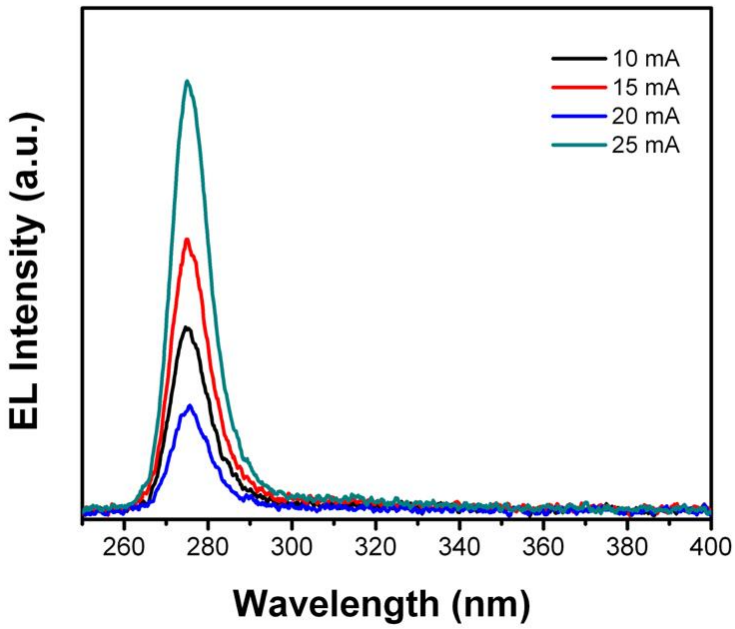

Figure 3-8: EL spectrum of an UV light emitting diode with a emission wavelength at 274 nm under various dc drive currents.

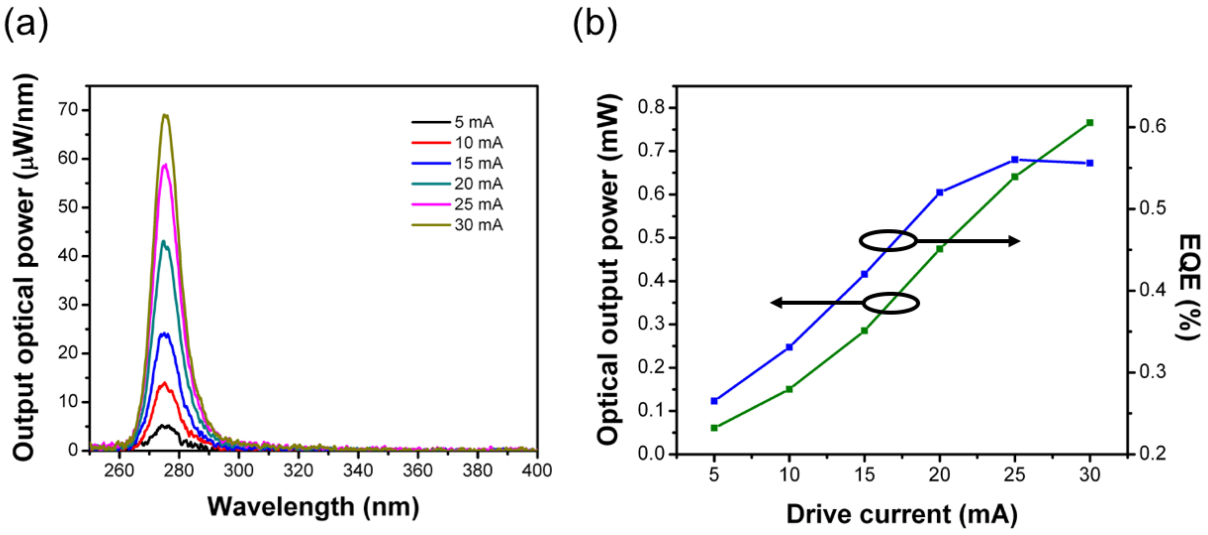

Figure 3-9: (a) Electroluminescence spectra, plotted as output power/nanometer v.s. wavelength, of a deep UV LED device with a peak intensity at 274 nm at various dc drive currents. (b) The plot of optical output power and EQE at various dc drive current.

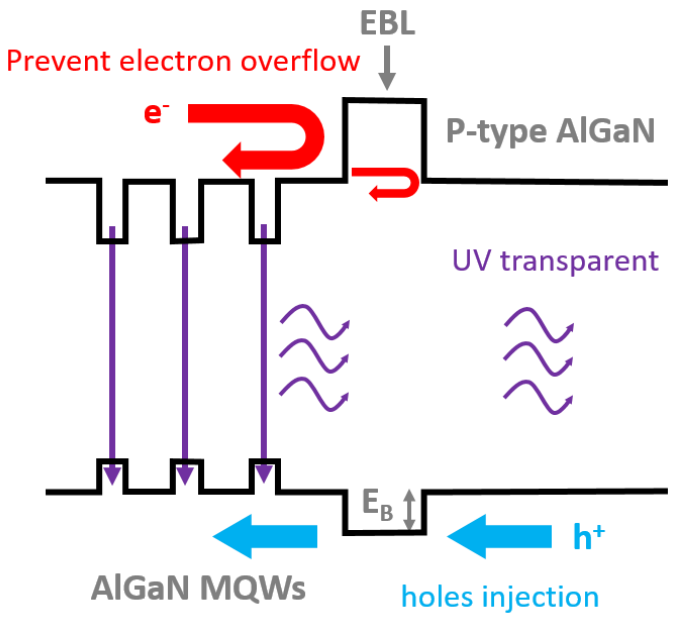

Figure 3-10: Schematic band diagram of an ultraviolet light emitting diode using (a) Mg-doped GaN and (b) Mg-doped AlGaN as the topmost p-type contact layer.

3.2 Ultraviolet light – emitting diodes based on Metal – Insulator – Semiconductor (MIS) structures

(Al, Ga) N is the most promising material for ultraviolet light-emitting diodes. However, as we already discussed, Mg-doped III-nitride films with high hole concentrations and low resistance are extremely difficult to achieve. Although we have presented a viable approach to high p-type doping concentration, there is another feasible approach to avoiding the need for high doping: it is by using metal-insulator-semiconductor (MIS) structures, first proposed by Maruska *et al.* [2]. An intriguing advantage is that light-emitting diodes with MIS Schottky diode structures, in general, have lower turn-on voltages than conventional

PIN heterostructures due to higher current flow across a low potential barrier [3,4]. This should reduce power consumption, thus saving energy.

The fundamental working principle of an MIS structure is illustrated in Figure 3-11. Figure 3-11 (a) shows the energy band diagram of an MIS structure without any forward bias applied. When sufficient forward bias is applied, as in Figure 3-11 (b), minority carriers (holes) are injected into the n-type semiconductor by tunneling through an insulating layer of a suitable thickness (t). To achieve sufficient minority carrier concentrations, the insulator material should be chosen such that the band gap and the work function lead to a lower tunneling barrier height (ϕ_h) for holes than the barrier for electrons (ϕ_e). In this way, the majority carriers (electrons) accumulate at the interface between the insulator and the semiconductor layer. The accumulated electrons can then recombine with the holes to emit light.

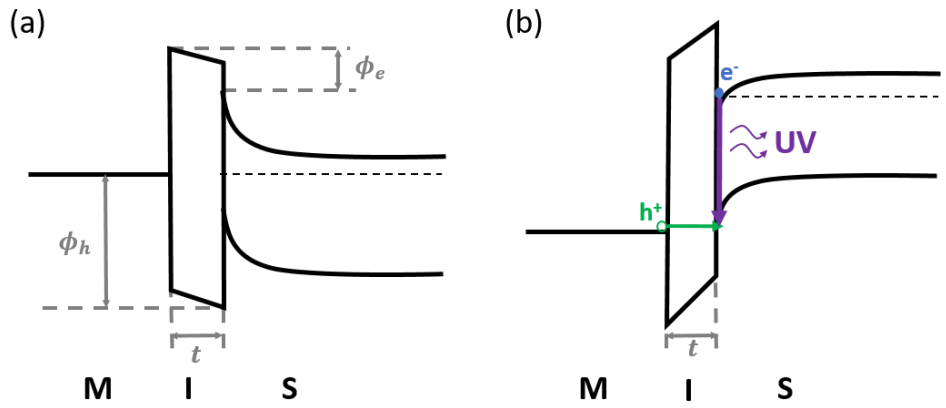

Figure 3-11: Schematic picture of energy band diagram for a metal-insulator-semiconductor structure (a) without bias and (b) with forward bias applied. ϕ_h and ϕ_e represent, respectively, the barrier height for holes and for electrons. The thickness of the insulating layer is denoted by t.

3.2.1 GaN – based MIS ultraviolet light – emitting diodes

Figure 3-12 illustrates the schematic diagram of a GaN-based MIS light-emitting diode. A thin insulating AlN layer of 10 nm was deposited on 1 µm of n-type GaN layer doped with silicon to an electron carrier concentration of 1×10^{19} cm^{-3}. We employed a multi-layer metal structure consisting of Ti (40 nm)/Al (120 nm)/Ni (40 nm)/Au (80 nm) stack for the n-contact electrode; this is annealed at 875 °C for 30 seconds in a forming gas atmosphere. A thin transparent contact layer of Ni (5 nm)/Au (5 nm) and a thicker contact layer of Ni (20 nm)/ Au (100 nm) was deposited on top of the AlN insulating layer for electrical probing. The Ni/Au stack layer was annealed at 500°C for 3 minutes in air ambient. The Ni/Au metal combination was chosen because it has a high work function that potentially reduces the barrier height for holes (ϕ_h) and enhances carrier recombination at the AlN/N-type GaN interface.

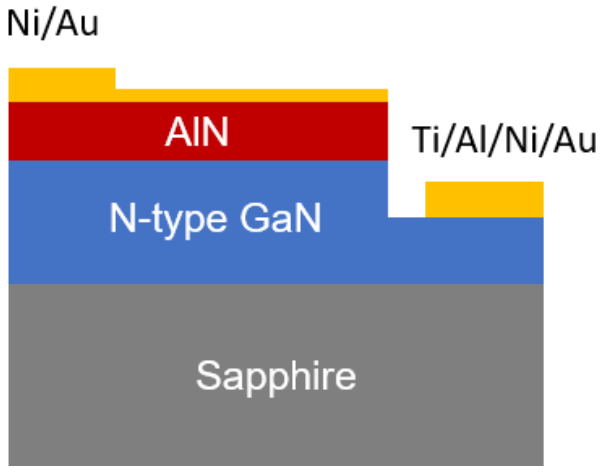

Figure 3-12: Schematic diagram of GaN-based MIS light emitting diodes.

Figure 3-13 shows the I-V characteristic for a typical GaN MIS diode at room temperature. The current increases dramatically above the threshold voltage of 3.1 eV, demonstrating good diode-like rectifying behavior. Note that the turn-on voltage for this GaN MIS LED is much lower than that for a conventional PIN heterostructure; this is probably because of the absence of the high voltage drops found in typical p-type (Al, Ga)N layers.

We have also performed TLM measurements for the GaN MIS diode. In Figure 3-14, the linear I-V characteristic between Ti/Al/Ni/Au contact metal combination and the N-type GaN demonstrates that a good ohmic contact is formed. From the plot, the contact resistance is 12 Ω, while the calculated sheet resistance is 0.145 kΩ/☐.

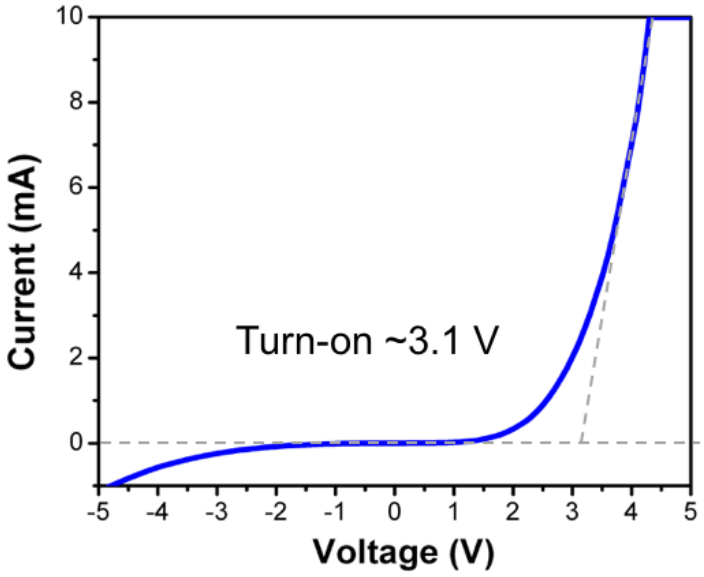

Figure 3-13: I-V characterization of the GaN MIS light emitting diode.

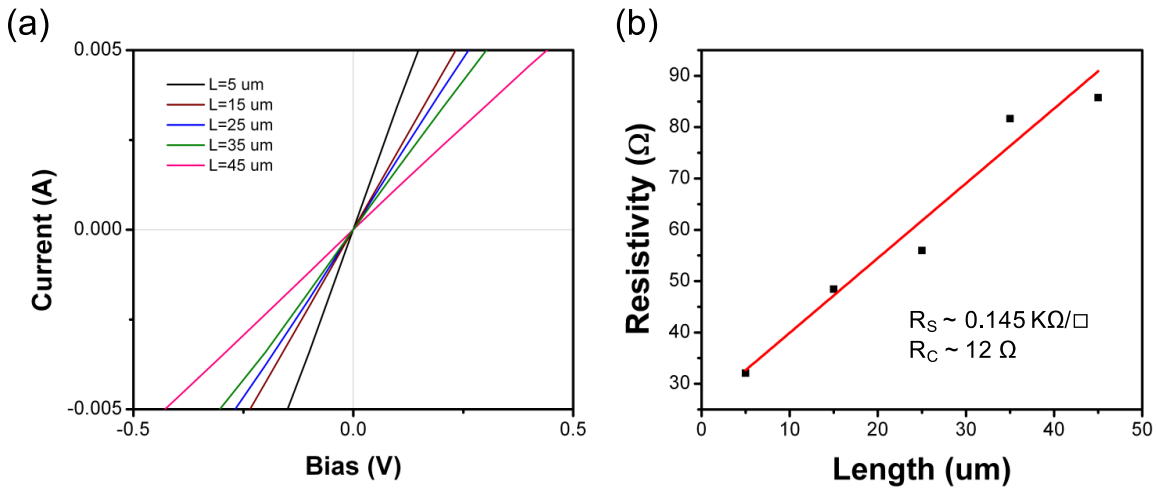

Figure 3-14: (a) I-V characterization of n-GaN with Ti/Al/Ni/Au contact annealing at 875 °C in forming gas for 30 seconds (b) TLM measurement on the mesa with various spacing of rectangular bars from 5 um to 45 um.

The electroluminescence (EL) spectrum of a typical GaN-based MIS LED at room temperature is shown in. Figure 3-15. The emission peak is located at 366 nm under a forward bias of 5 V. This result demonstrates the successful creation of a MIS UV light-emitting diodes without any p-type doping. This has potential for design and fabrication of solid state UV lighting with low power consumption.

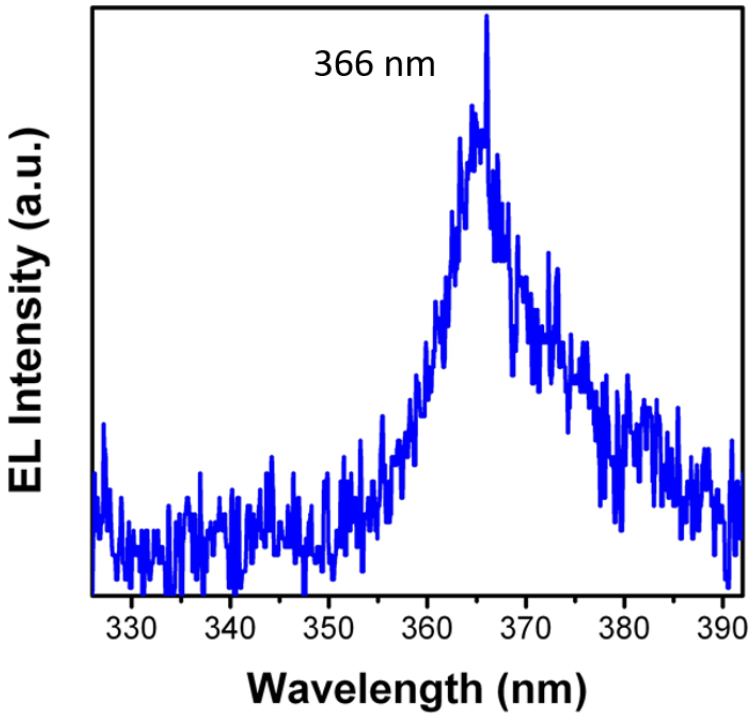

Figure 3-15: Electroluminescence spectrum of the GaN MIS light emitting diode.

3.2.2 AlGaN – based MIS deep ultraviolet light-emitting diodes

After successfully achieving a GaN-based MIS Schottky-barrier-type light-emitting diode, we attempted to push the emission wavelength of a such device to the shorter wavelengths by incorporating high-aluminum containing III-nitrides. The schematic diagram and design of the band structure of an AlGaN-based MIS LEDs are illustrated in Figure 3-16 (a) and (b). A 1-um thick Si-doped $Al_{0.58}Ga_{0.42}N$ film with an electron carrier concentration of 1×10^{19} cm^{-3} was deposited on a sapphire substrate by molecular beam epitaxy. Following this, a thin insulating layer of a composite of AlN with two different thickness of 15 nm and 50 nm was deposited on top of the n^{+}-AlGaN film. We note that a palladium (Pd) metal

contact instead of nickel is used for this MIS diode due to its higher work function (ϕ) required to match the larger band gap of the (Al,Ga)N. This should decrease the barrier to the minority holes (ϕ_h) being injected from the metal to the n-type AlGaN semiconductor.

Figure 3-17 shows the current-voltage (I-V) characteristics of the AlGaN-based MIS LEDs with different thickness of the insulating AlN layer. The I-V curves of both devices exhibit a diode-like rectifying behavior. However, the device with the thinner insulating AlN layer of 15 nm has a larger leakage current than that of the device with a thicker AlN layer (50 nm). As expected, the thicker insulating layer provides better carrier confinement at the interface of insulating AlN layer and the heavily doped AlGaN semiconductor layer. Despite the good carrier confinement, the turn-on voltage of the device with the 50-nm AlN layer is 2.8 V, which is slightly higher than the 2.5 V of the device with a 15-nm AlN layer. This indicates that the thicker insulating layer reduces the injection of minority carrier into the semiconductor region. Compared to the GaN-based MIS LEDs, the turn-on voltages of the AlGaN-based MIS LEDs are slightly lower. We suspect that the lower turn-on voltage is probably a result of the higher work function of the Pd metal which reduces the barrier height for minority carrier injection. We have also investigated the contact resistance between the Ti/Al/Ni/Au contact metal combination and the n-type AlGaN by TLM measurements. Figure 3-18 shows that a low contact resistance of 41 Ω and a low series resistance of 0.61 kΩ/□ can be achieved for this metal contact combination on n-type high aluminum-containing AlGaN films. The electroluminescence spectrum of the AlGaN-based MIS LEDs is shown in Figure 3-19. The weak emission peak at around 275 nm can be attributed to the low carrier density and low carrier confinement in such a device.

Therefore, to further improve the devices in terms of high quantum efficiency, we

have fabricated MIS LEDs designed with low-dimensional quantum well structure in them. Such a structure should provide strong carrier confinement in the well region and enhance excitonic recombination. The epitaxial structure of the MIS quantum well light-emitting diode is illustrated in Figure 3-20 (a). In this structure, an ultra-thin GaN single quantum well is inserted between the insulating layer and the n-type AlGaN. The band structure of this device is shown in Figure 3-20 (b). By carefully controlling the GaN layer thickness to a monolayer precision, the quantum confined energy levels can be shifted to higher energies (E_n) by reducing the thickness of the GaN quantum well (L_Z), according to the equation

$$E_n = \frac{\hbar^2 k_n^2}{2m} = \frac{\hbar^2 n^2 \pi^2}{2mL_Z} \tag{3-3}$$

This is experimentally demonstrated in the room-temperature photoluminescence shown in Figure 3-21. The emission wavelength shifts from 350 nm to 320 nm with decreasing thickness of the GaN quantum well from 7-8 ML to 4-5 ML. These thicknesses are estimated from the growth rate.

A schematic of the GaN quantum well MIS LEDs with different well thicknesses is illustrated in Figure 3-22 (a). A combination of Pd/Au metals are utilized for the Schottky contact to the AlN insulator layer, while a combination of Ti/Al/Ni/Au serves as the ohmic contact to the n-type AlGaN semiconductor layer. Figure 3-22 (b) shows the EL spectra of GaN quantum well MIS LEDs under 6V forward voltage at room temperature. This shows that the emission wavelength can be shifted by controlling the thickness of the ultrathin GaN quantum well in the electrically-injected ultraviolet MIS LEDs.

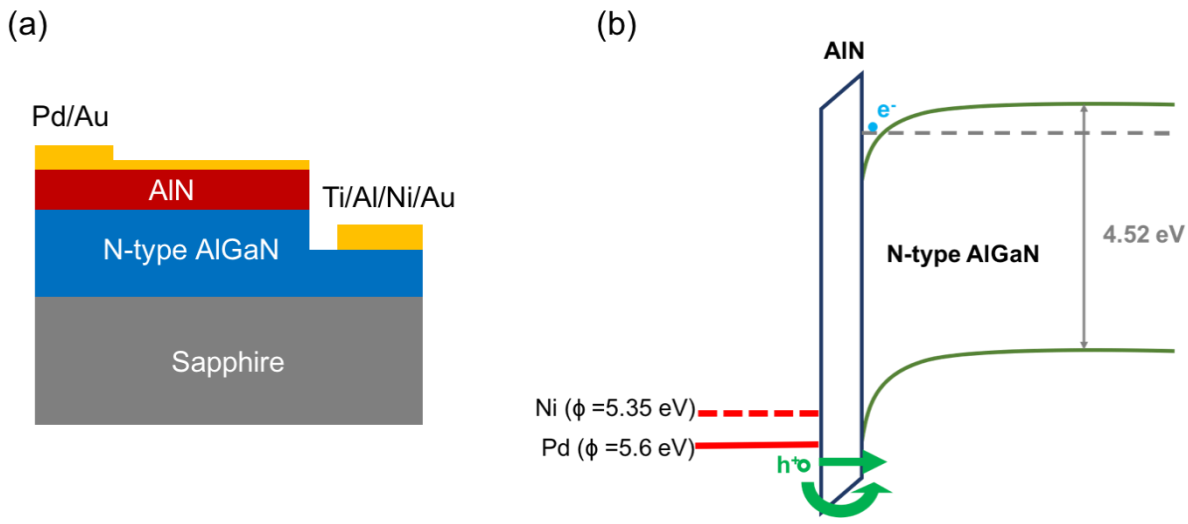

Figure 3-16: The schematic diagram of (a) AlGaN-based MIS light emitting diodes and (b) the corresponding band structure.

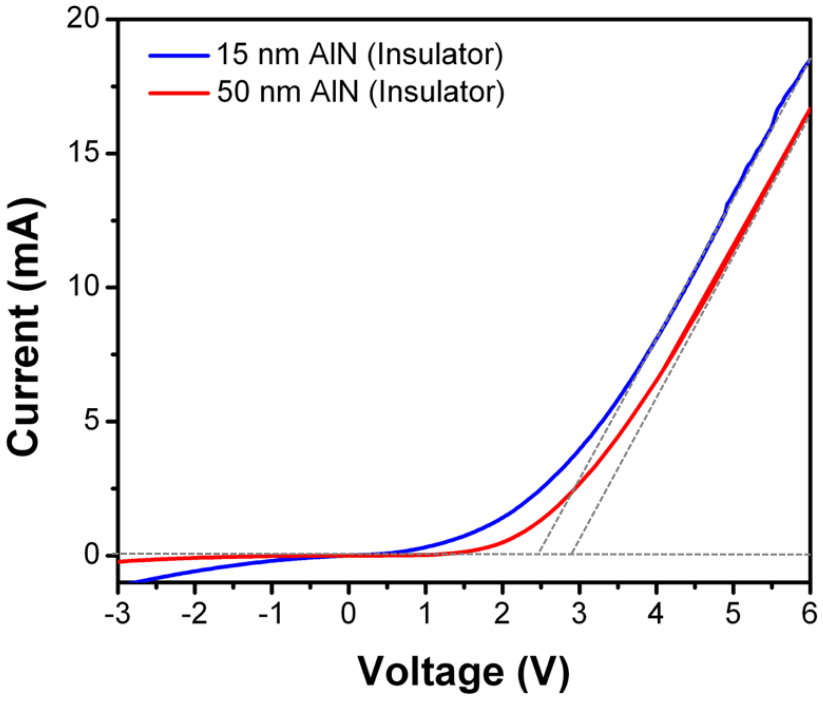

Figure 3-17: I-V characterization of the AlGaN MIS light emitting diode.

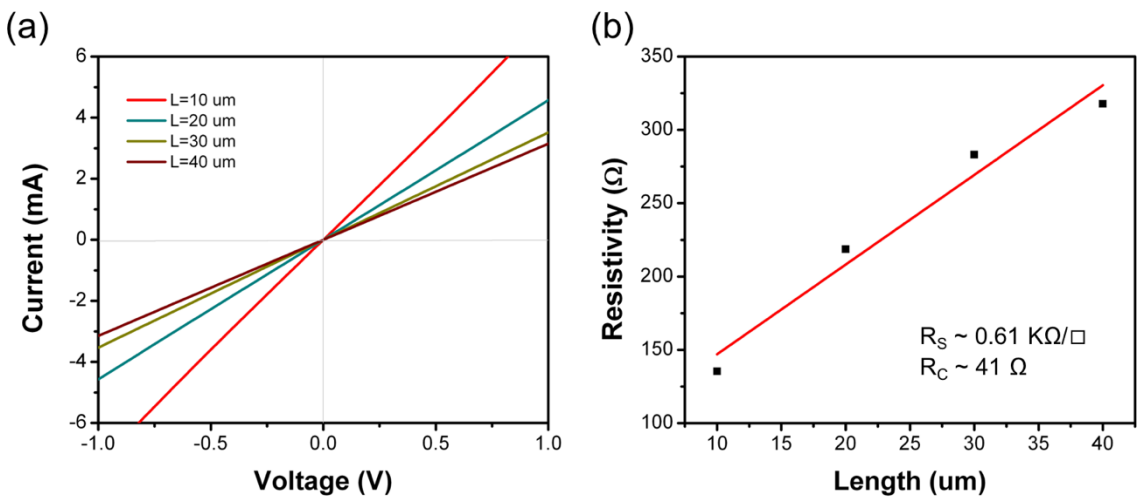

Figure 3-18: (a) I-V characterization of n-AlGaN with Ti/Al/Ni/Au contact annealing at 875 °C in forming gas for 30 seconds (b) TLM measurement on the mesa with various spacing of rectangular bars from 10 um to 40 um.

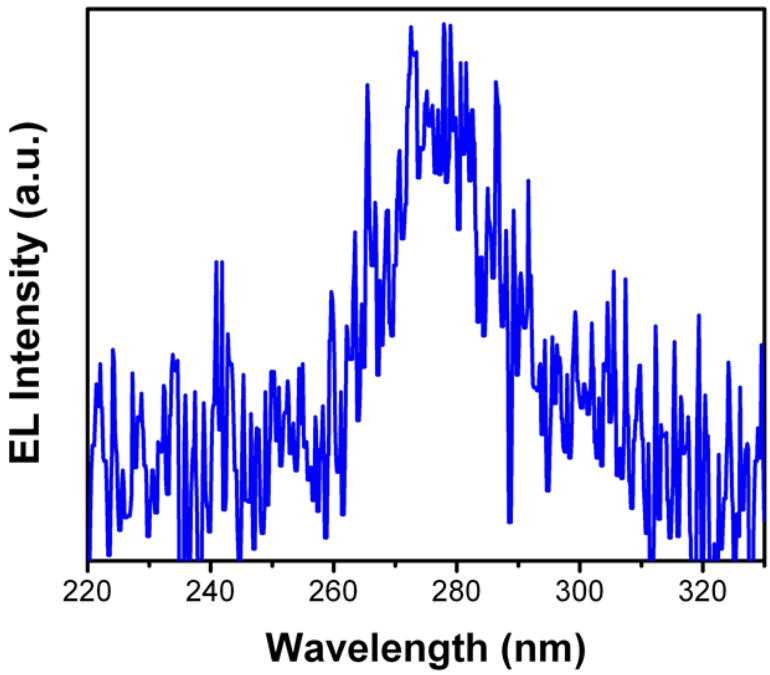

Figure 3-19: Electroluminescence spectrum of the AlGaN MIS light emitting diode.

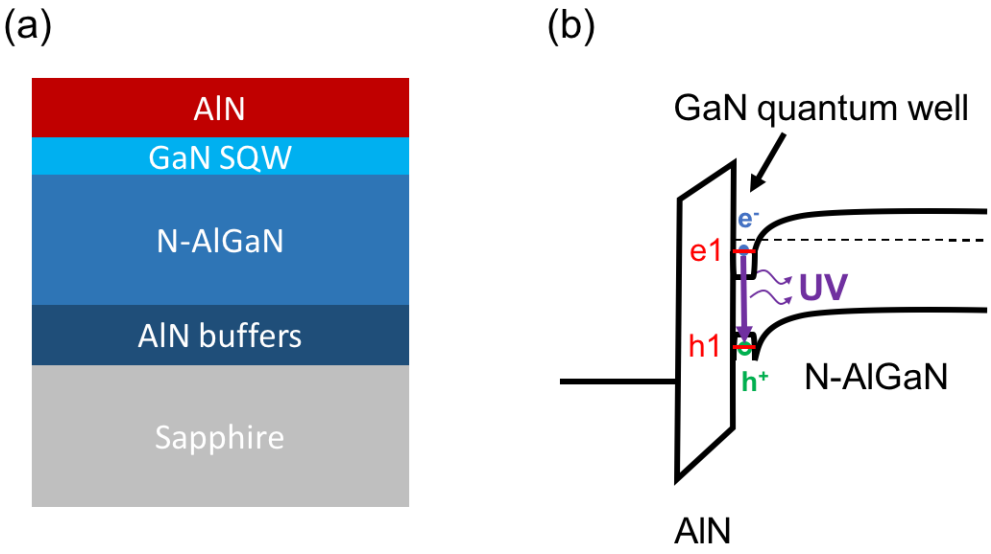

Figure 3-20: (a) Schematic illustration of GaN single quantum well MIS LED epitaxial layer. (b) The illustration of band structure of single quantum well MIS LEDs.

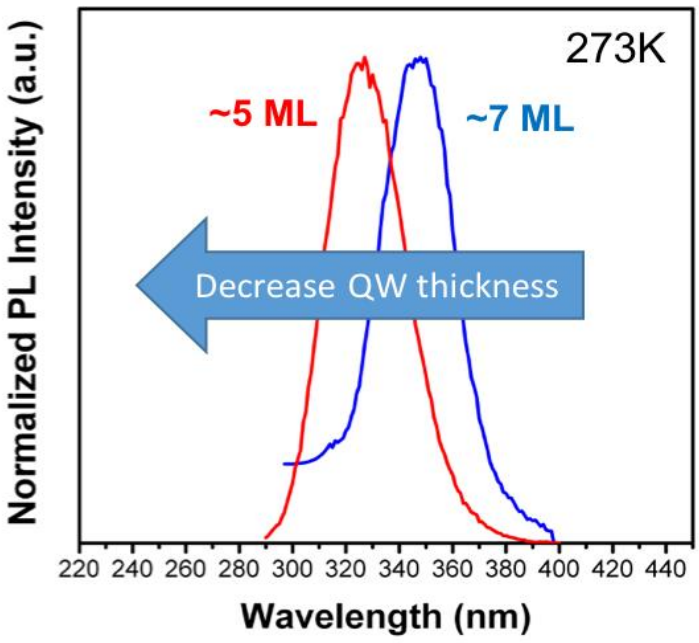

Figure 3-21: Room-temperature photoluminescence spectra of GaN quantum well metal-insulator-semiconductor LEDs.

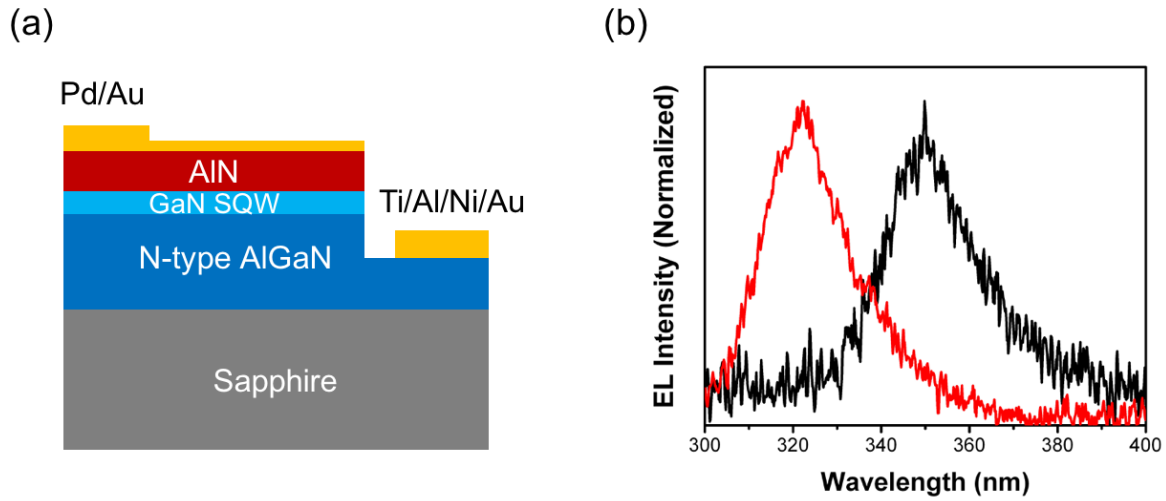

Figure 3-22: (a) Schematic diagram of GaN single quantum well MIS LED devices (b) Electroluminescence spectra of monolayer thin GaN MIS LEDs.

3.3 Reference

[1] Y. Liao, C. Kao, C. Thomidis, A. Moldawer, J. Woodward, D. Bhattarai, and T. D. Moustakas, "Recent Progess of efficient deep UV-LEDs by plasma-assisted molecular beam epitaxy," *Phys. Status Solidi*, vol. 801, no. 3, pp. 798–801, 2012.

[2] H. P. Maruska and D. A. Stevenson, "Mechanism of light production in metal-insulator-semiconductor diodes; GaN:Mg violet light-emitting diodes," *Solid State Electron.*, vol. 17, no. 11, pp. 1171–1179, 1974.

[3] Y. Taniyasu, M. Kasu, and T. Makimoto, "An aluminium nitride light-emitting diode with a wavelength of 210 nanometres," *Nature*, vol. 441, no. 7091, pp. 325–328, 2006.

[4] H. Huang, G. Fang, X. Mo, H. Long, and L. Yuan, "ZnO-Based Fairly Pure Ultraviolet Light-Emitting Diodes With a Low Operation Voltage," *IEEE Electron Device Lett.*, vol. 30, no. 10, pp. 1063–1065, 2009.

Chapter 4

Ultraviolet lasers

Having succeeded in making UV LEDs, we now focus on UV lasers. Two types of UV lasers will be discussed in this Chapter: a conventional edge-emitting laser structure, and an advanced photonic crystal surface-emitting laser.

4.1 Conventional edge-emitting UV laser diodes

4.1.1 Optically-pumped (Al, Ga)N UV lasers

Achieving high quality (Al, Ga)N epitaxial layers in which smooth mirror facets can be made is imperative to realizing electrically-pumped UV laser diodes. The first step along this path is demonstration of the feasibility of optically-pumped (Al, Ga)N lasers.

Figure 4-1 shows a schematic epitaxial layer structure for an (Al, Ga)N MQW laser structure grown on a c-plane sapphire substrate by plasma-assisted MBE. Growth is initiated by deposition of superlattice comprised of 30 periods of AlGaN/AlN on an AlN template. This superlattice can potentially release the built-in strain at the interface of the AlN template and the c-plane sapphire substrate. On top of the superlattice is grown an $Al_{0.25}Ga_{0.75}N$ buffer layer with a thickness of 650 nm. This is followed by 10 periods of $Al_{0.2}Ga_{0.8}N$ (10 nm)/GaN (2 nm) MQWs that are sandwiched between $Al_{0.2}Ga_{0.8}N$ cladding layers, each of which has a thickness of 50 nm.

The room temperature photoluminescence spectra of the (Al, Ga)N/GaN MQW structure are shown in Figure 4-2. An intense emission peak originating from the (Al,Ga)N/GaN multi-quantum well structure is observed at 362 nm; another weaker peak

located at 315 nm is also observed. The weaker peak is associated with the $Al_{0.2}Ga_{0.8}N$ cladding layers.

We have fabricated laser facets onto the (Al, Ga)N structure using chlorine-based, inductively-coupled plasma reactive-ion etching (ICP-RIE) tool. The etched facets were not anti-reflection coated. Laser devices with cavity lengths (L), ranging from 500 μm to 1000 μm, and ridge widths (W) ranging from 20 μm to 50 μm were isolated; these are illustrated in Figure 4-3. The laser bars were optically-pumped with a frequency-quadrupled Nd:YAG laser source at 266 nm with 400-ps pulses. The emission from the (Al, Ga)N MQW laser structure was characterized with a holographic grating spectrometer. A schematic of the measurement system is shown in Figure 4-4. Figure 4-5 (a) shows the emission spectra from the multiple-quantum well structure with the cavity length of 500 μm for different pumping power levels that range from 0.5 uW to 50 uW; these correspond to power densities of 0.159 W/cm^2 to 15.923 W/cm^2. We note that the spectra exhibit features typical of longitudinal Fabry-Perot waveguide modes. The mode spacing is given by

$$\Delta\lambda = \frac{1}{L} \cdot \left[\frac{\lambda^2}{2}\left(n - \lambda\frac{dn}{d\lambda}\right)\right] \qquad (4\text{-}1)$$

where L is the cavity length, and n is the index of refraction at a wavelength λ. For a given λ, the mode spacing $\Delta\lambda$ scales in proportional to the inverse cavity length ($1/L$). The inset image in Figure 4-5 (a) shows the successful emission resulting from the optically-pumped (Al, Ga)N MQW laser structure. The output light power as a function of excitation power density (Output Light versus Input Light curve) is shown in Figure 4-5 (b). The estimated input threshold lasing power density is larger than 26 W/cm^2.

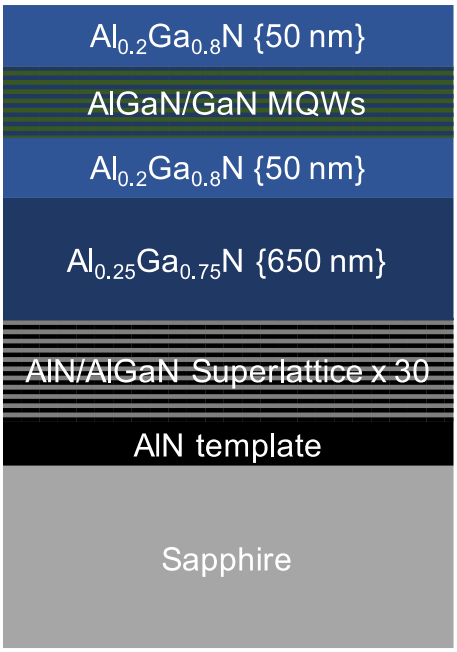

Figure 4-1: Schematic illustration of (Al,Ga)N MQW laser structure.

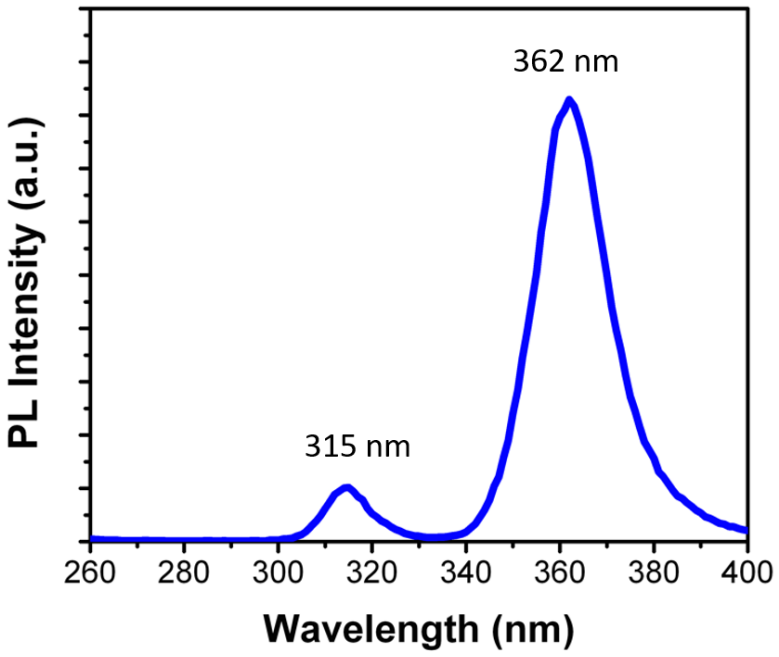

Figure 4-2: Photoluminescence spectrum of an epitaxial $Al_{0.2}Ga_{0.8}N$/GaN MQW laser structure.

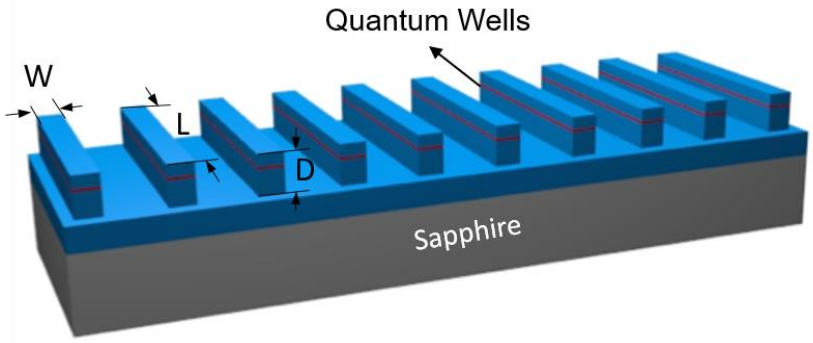

Figure 4-3: Schematic structure of an array of (Al, Ga)N MQW ridge-guide edge-emitting lasers, where W, L, and D represent the width, length, and depth of laser ridges, respectively.

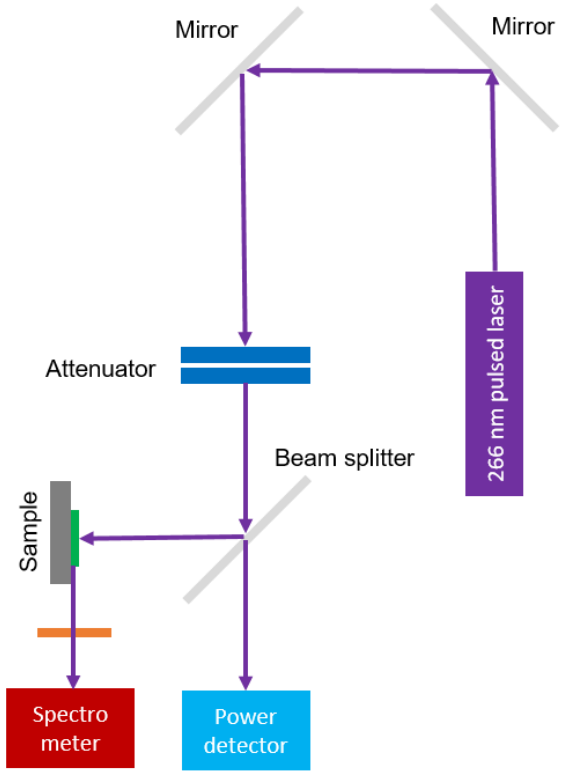

Figure 4-4: Schematic of the laser optical-pumping and measurement system.

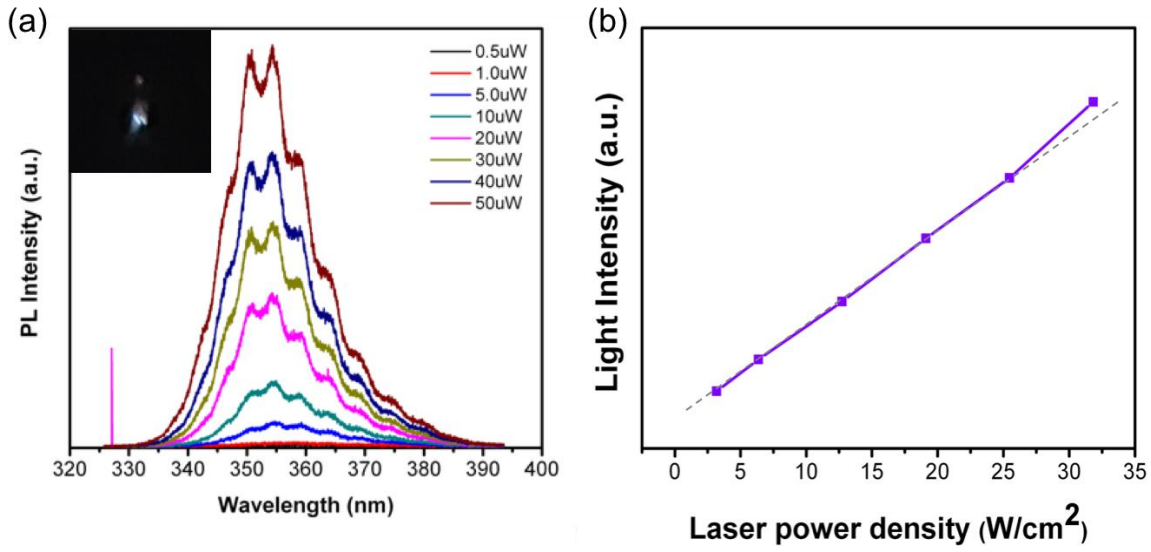

Figure 4-5: (a) Room temperature emission spectra from an $Al_{0.2}Ga_{0.8}N$/GaN MQW laser structure for different optical pumping power levels. The insert is an image of the emission from the optically-pumped MQW laser structure. (b) Output light intensity (in arbitrary units) as a function of the optical pumping power density at room temperature.

4.1.2 Electrically-pumped (Al, Ga)N UV lasers

Figure 4-6 depicts the schematic cross-sectional structure of an (Al, Ga)N UV laser diode. The structure was grown on top of a 25-nm AlN template on a c-plane sapphire substrate by plasma-assisted molecular beam epitaxy under liquid-metal-enabled growth conditions. On top of the templated is grown 30 periods of an AlGaN/AlN superlattice. Following this, a 1.5-μm-thick Si-doped $Al_{0.5}Ga_{0.5}N$ cladding layer is grown; the cladding is followed by a 100 nm-thick Si-doped $Al_{0.35}Ga_{0.65}N$ wave-guiding layer. The active region has 5 periods of an $Al_{0.35}Ga_{0.65}N$ (7 nm)/GaN (2 nm) multiple-quantum-well structure. On top of the active region is a 100-nm-thick Mg-doped $Al_{0.35}Ga_{0.65}N$ wave-guiding layer, then

a 10-nm-thick Mg–doped $Al_{0.6}Ga_{0.4}N$ electron-blocking layer; finally, a 20-nm-thick Mg-doped $Al_{0.5}Ga_{0.5}N$ cladding layer is grown; this is capped with 80 nm of p-GaN contact layer.

The (Al, Ga)N UV laser structure was then fabricated into devices by standard photolithographic processes depicted in Figure 4-7. Laser stripes of widths ranging from 20 μm to 50 μm were then created by chlorine-based dry-etching. A stack of metals consisting of Ti (40 nm)/ Al (120 nm)/ Ni (40 nm)/ Au (80 um) was deposited as the n-type contact electrode. This is annealed at 875 °C for 30 seconds in forming gas. This step is followed by deposition of a 100-nm-thick SiO_2 insulating layer on the p-side wall of the ridge for confining carrier flow. The last step is to deposit the p-type contact comprised of Ni (20 nm)/ Au (100 nm) layers; this metal combination is then annealed at 500 °C for 3 minutes in ambient air. Devices with cavity lengths ranging from 500 μm to 1000 μm were then formed by dry etching.

4.1.1.1 Electrical characteristic of UV laser diode

The contact resistivity of the fabricated UV laser diode was characterized by the transmission line measurement (TLM) method we discussed earlier. The linear I-V characteristic shown in Figure 4-8 (a) shows that a good ohmic contact is achieved for the n-contact electrode formed on top of the n-type $Al_{0.5}Ga_{0.5}N$ contact layer; this contact electrode was annealed at 875 °C in forming gas for 30 seconds. From the TLM curve in Figure 4-8 (b), we extract the contact resistance as 11 Ω and the corresponding sheet resistance as 0.605 kΩ/□. Figure 4-9 shows the I-V characteristic for the (Al, Ga)N UV laser diode. The forward current increases dramatically above the threshold voltage of 1.5 V.

This low turn-on voltage is attributed to the restriction of the current flow into the narrow stripe.

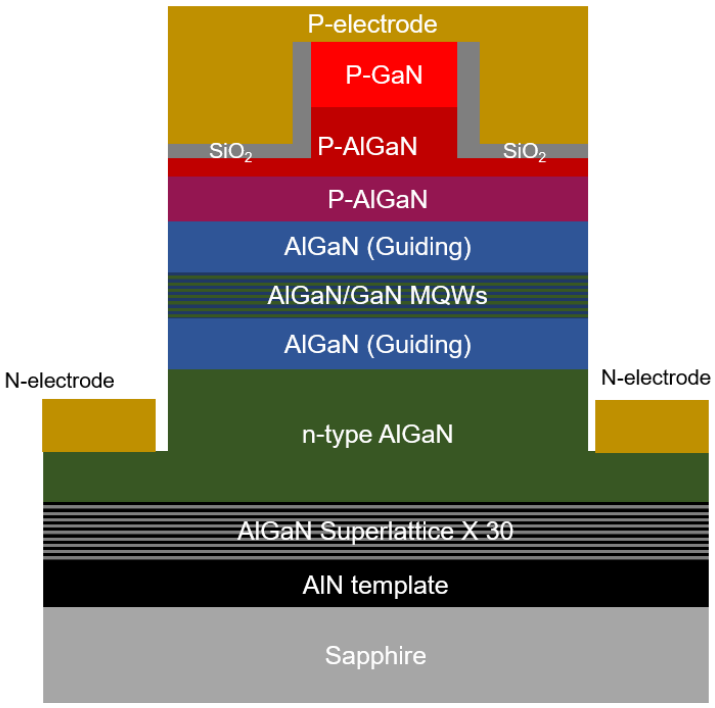

Figure 4-6: Schematic illustration of an edge-emitting UV laser diode.

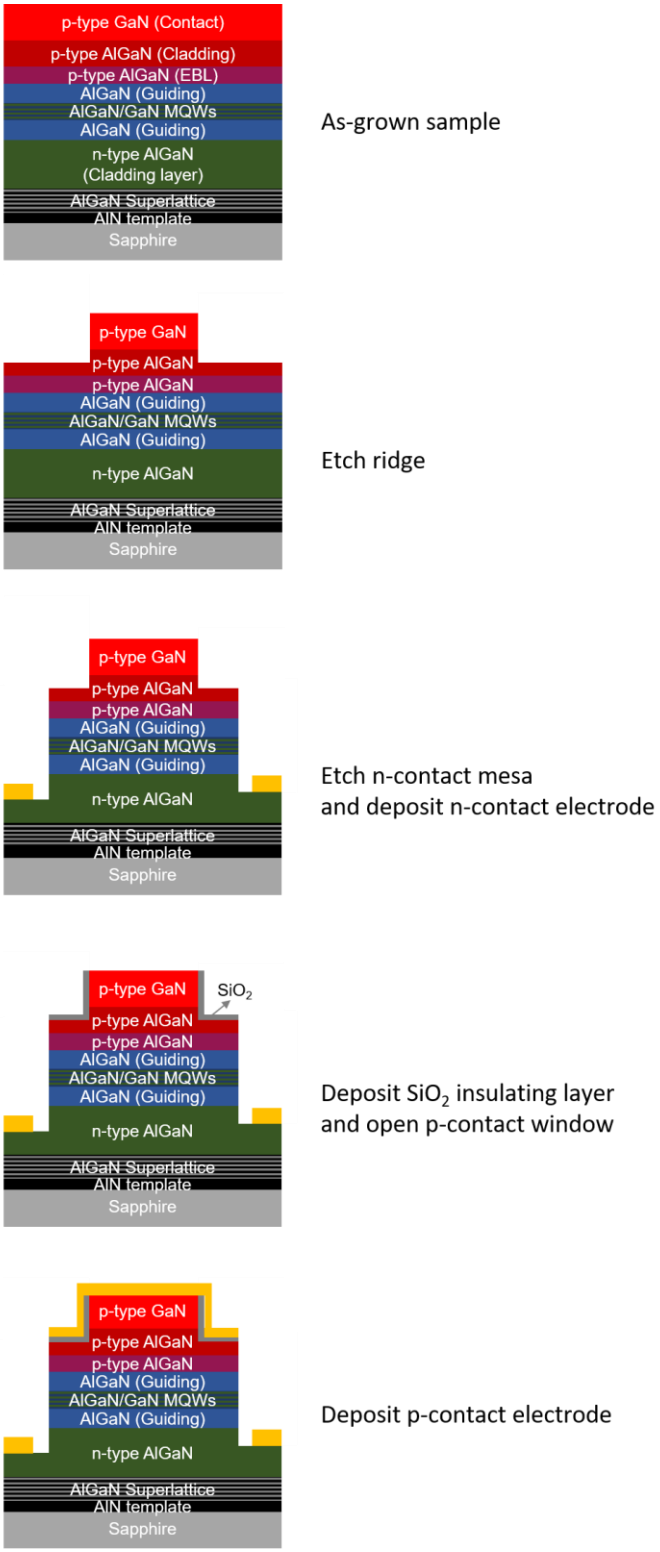

Figure 4-7: Schematic illustration of the micro-fabrication process for the UV laser diode.

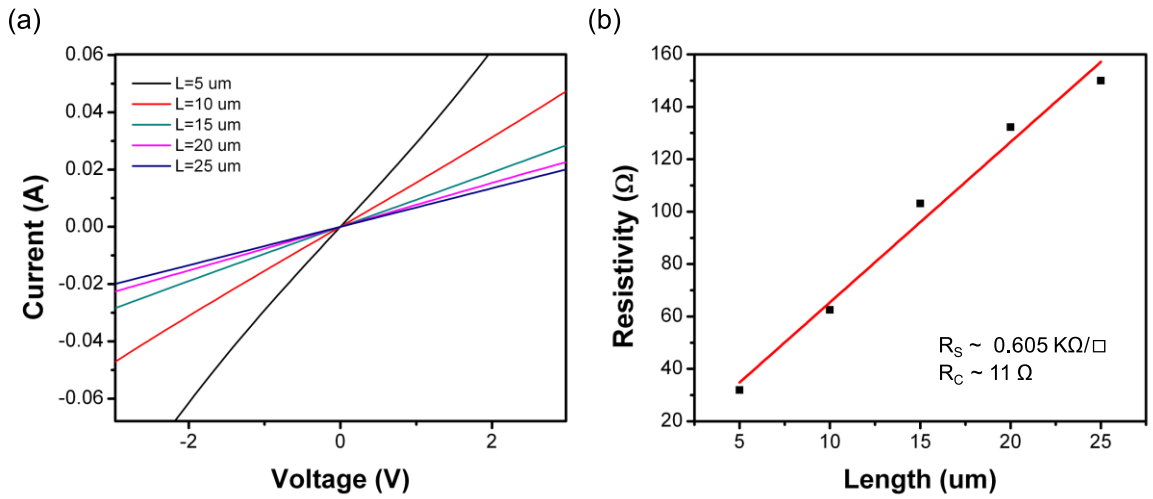

Figure 4-8: (a) Current-voltage (I-V) characteristic of n-$Al_{0.5}Ga_{0.5}N$ with Ti/Al/Ni/Au contact annealed at 875 °C in forming gas for 30 seconds (b) TLM measurement of the mesa with various spacing widths of rectangular bars from 5 μm to 25 μm.

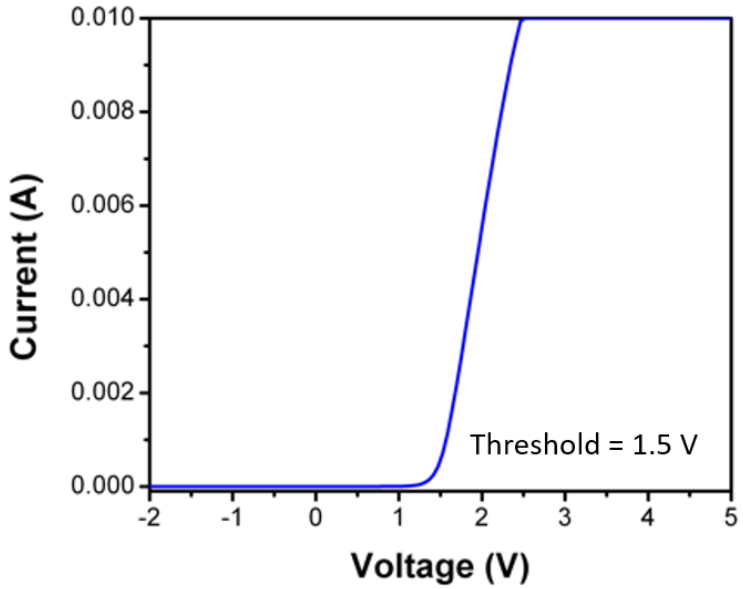

Figure 4-9: Current-voltage (I-V) characteristic of and (Al, Ga)N-based UV laser diode.

4.2 Photonic crystal surface-emitting UV laser diodes

Photonic crystal lasers with two- or three-dimensional Bragg reflectors have attracted considerable attention because of their potential advantages over conventional laser geometries as discussed in Chapter 1. In this section, we present one type of such laser — the photonic crystal defect-type nanocavity laser.

4.2.1 Numerical simulation of photonic crystals

Before fabricating a complex photonic crystal structure, it is imperative that an accurate computational model be developed for optimizing the key parameters. There are several numerical simulation methods for computing photonic crystal band structures. One such method is the plane wave expansion (PWE) method which can be used to analyze photonic crystals with infinite or defect-type periodic structures, photonic crystal waveguides, or photonic crystal fibers [1]. We briefly introduce the fundamental theory of the PWE method.

Propagation of light in periodic photonic crystal structures is governed by the macroscopic Maxwell equations, which are:

$$\begin{aligned} \nabla \cdot B &= 0 \\ \nabla \times E + \frac{\partial B}{\partial t} &= 0 \\ \nabla \cdot D &= \rho \\ \nabla \times H - \frac{\partial D}{\partial t} &= J \end{aligned} \tag{4-2}$$

where E and H are the macroscopic electric and magnetic field intensities, D and B are the displacement and magnetic induction fields, and ρ and J are the free charge and current densities, respectively. We will assume that light propagates within a mixed dielectric

medium, in which the dielectric material is a function of position vector r, and there are no free charges and currents ($\rho = 0$ and $J = 0$). With these assumptions, D and B can be related to the electric and magnetic field intensities through the constitutive relations as:

$$\begin{aligned} \mathrm{D(r)} &= \varepsilon_0 \varepsilon(r) E(r) \\ \mathrm{B(r)} &= \mu_0 \mu(r) E(r) \end{aligned} \tag{4-3}$$

where ε(r) is the relative permittivity and μ(r) is the relative magnetic permeability. Our medium is assumed to be loss-less, where ε(r) is real in the regions of interest, and $\mu(r) = \mu_0$ is constant. The Maxwell equations then become

$$\begin{aligned} \nabla \cdot H(r,t) &= 0 \\ \nabla \times E(r,t) + \mu_0 \frac{\partial H(r,t)}{\partial t} &= 0 \\ \nabla \cdot [\varepsilon(r) E(r,t)] &= 0 \\ \nabla \times H(r,t) - \varepsilon_0 \varepsilon(r) \frac{\partial E(r,t)}{\partial t} &= 0 \end{aligned} \tag{4-4}$$

We can separate the time dependence from the spatial dependence for both E and H by expanding the fields into a set of harmonic modes as below.

$$\begin{aligned} H(r,t) &= H(r) \cdot e^{-i\omega t} \\ E(r,t) &= E(r) \cdot e^{-i\omega t} \end{aligned} \tag{4-5}$$

To find the equations governing the mode profiles for a given frequency, we insert Equation (4-5) into Equation (4-4) to obtain:

$$\begin{aligned} \nabla \cdot H(r) &= 0 \\ \nabla \times E(r) - i\omega\mu_0 H(r) &= 0 \\ \nabla \cdot [\varepsilon(r) E(r)] &= 0 \\ \nabla \times H(r) + i\omega\varepsilon_0 \varepsilon(r) E(r) &= 0 \end{aligned} \tag{4-6}$$

One can obtain the eigen value equation, or the master equation, for the magnetic and electric fields, respectively, by combining the equations above and noting that $= 1/\sqrt{\varepsilon_0 \mu_0}$, thus:

$$\nabla \times \left[\frac{1}{\varepsilon(r)} \nabla \times \mathrm{H(r)}\right] = \left(\frac{\omega}{c}\right)^2 H(r)$$
$$\frac{1}{\varepsilon(r)} \nabla \times [\nabla \times \mathrm{E(r)}] = \left(\frac{\omega}{c}\right)^2 E(r) \tag{4-7}$$

According to Bloch's theorem, the eigen function of an infinite periodic structure can be represented as plane wave multiplied by a periodic function that has the periodicity of the lattice as follows:

$$H(r) = H_{k,n}(r) \cdot \exp(j \cdot k \cdot r)$$
$$E(r) = E_{k,n}(r) \cdot \exp(j \cdot k \cdot r) \tag{4-8}$$

Here, $H_{k,n}(r)$ has the periodicity of the lattice with wave vector k and state number n. We further expand the fields in Equation (4-7) into a Fourier series using the reciprocal lattice vectors, which for the magnetic field can be written as

$$H(r) = \sum_G H_{k,n}(G) \cdot \exp[j \cdot (k + G) \cdot r] \tag{4-9}$$

Since the dielectric function of the material is also a periodic function, it can be written as a Fourier series, thus:

$$\frac{1}{\varepsilon(r)} = \sum_{G''} \chi(G'') \cdot exp[j \cdot (k + G) \cdot r] \tag{4-10}$$

where $\chi(G'')$ are the Fourier expansion coefficients of the inverted dielectric function. Equations (4-9) and (4-10) can be substituted into Equation (4-7) to get

$$\sum_{G''}\frac{\partial}{\partial r}\chi(G'')\cdot\exp(j\cdot(k+G)\cdot r)\frac{\partial}{\partial r}\sum_{G'}H_{k,n}(G')\cdot\exp[j\cdot(k+G')\cdot r]$$
$$=\frac{\omega^2}{c^2}\sum_{G}H_{k,n}(G)\cdot\exp[j\cdot(k+G)\cdot r] \tag{4-11}$$

where $G=G'+G''$. Then, taking derivatives and combining the exponents we obtain:

$$\sum_{G}\sum_{G'}\chi(G-G')\cdot H_{k,n}(G')\cdot\exp[j\cdot(k+G)\cdot r]$$
$$\cdot[j\cdot(k+G)\cdot j\cdot(k+G')] \tag{4-12}$$
$$=\frac{\omega^2}{c^2}\sum_{G}H_{k,n}(G)\cdot\exp[j\cdot(k+G)\cdot r]$$

The projection to the basis $\exp[j\cdot(k+G)\cdot r]$ gives the equation:

$$-\sum_{G'}\chi(G-G')\cdot(k+G)\cdot(k+G')\cdot H_{k,n}(G')=\frac{{\omega_{k,n}^{H}}^2}{c^2}H_{k,n}(G) \tag{4-13}$$

This eigen value equation for the Fourier expansion coefficients of electric fields can also be performed in a similar fashion to give

$$-\sum_{G'}\chi(G-G')\cdot(k+G')\cdot(k+G')\cdot E_{k,n}(G')=\frac{{\omega_{k,n}^{E}}^2}{c^2}E_{k,n}(G) \tag{4-14}$$

where $\omega_{k,n}^{H}$ and $\omega_{k,n}^{E}$ are eigen frequencies for the TE and TM polarizations, respectively, corresponding to the eigenvectors for mode n; $H_{k,n}$ and $E_{k,n}$..

We show below an example of a photonic crystal band structure obtained by using the PWE method for a triangular array of air-holes in a GaN dielectric medium ($\varepsilon=n^2=2.5^2$). Figure 4-10 (a) and (b) are the calculated band structure diagrams for a 2D hexagonal lattice for the TE and TM modes, respectively. The vertical axes represent the ratio of the lattice constant to wavelength (a/λ); the horizontal axes represent the k-vectors in the

reduced Brillouin zone in the directions Γ, M, and K within the zone. The yellow shaded area represents the photonic band gap. Within the band gap, light cannot propagate in certain directions with specified frequencies. This unique property enables manipulation of various photonic behaviors in artificial photonic crystal structures.

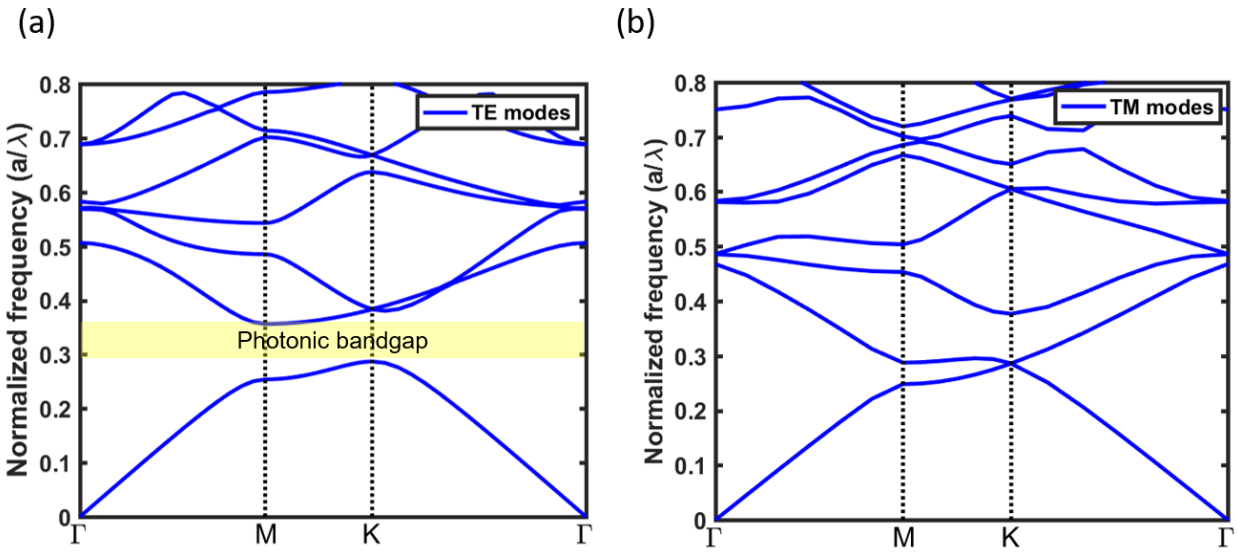

Figure 4-10: The photonic band structure of (a) TE modes and (b) TM modes for a GaN 2D triangular lattice structure.

4.2.2 Defect-type photonic crystal lasers

In the photonic crystal surface-emitting nanocavity, the optical cavity is created by a defect in the photonic crystal. This creates an optical mode localized in the defect region of high quality (Q) factor cavity. Defect modes are resonant in the cavity region and are evanescent away from the cavity in the x-y plane. The localized optical mode can be coupled to the gain medium in the defect region so that it emits when the threshold condition

is reached. Typically, photonic crystal nanocavity lasers have relatively small active volumes, leading to ultra-low threshold current densities. Such a structure also leads to extremely low material and cavity losses and to long photon life times in the cavity. These advantages make photonic crystal nanocavity lasers superior to conventional Fabry-Perot lasers for developing deep UV highly coherent sources.

In the following, we discuss our effort at making GaN photonic crystals before working on AlGaN-based photonic crystals. The photonic crystal band structure of a triangular GaN lattice with r/a = 0.28 is shown in Figure 4-11. Based on this band structure, a few of eigen-frequencies are located at around $a/\lambda = 0.55$ near the Γ point, where the most efficient coupling of horizontally guided modes and radiation modes occur. Figure 4-12 shows a two-dimensional GaN photonic crystal with a type of defect known as H2, which consists of seven missing air holes. The structure is fabricated from 1-μm-thick Si-doped GaN layer grown at 770 °C by molecular beam epitaxy. The photonic crystals are fabricated using a standard electron-beam lithography process that is illustrated in Figure 4-13. A hard mask consisting of a SiN_x layer of 200 nm was first deposited on the as-grown sample by plasma-enhanced chemical vapor deposition; this is followed by a soft mask consisting of a 200-nm polymethylmethacrylate (PMMA) layer. A hexagonal photonic crystal pattern covering an area of $20 \times 20\ \mu m^2$ was defined by electron beam lithography on the PMMA mask. The circular air hole diameter (r) ranges from 55 nm to 60 nm, while the lattice constant (a) is chosen to be 200 nm such that the ratio r/a is about 0.28. The photonic crystal pattern is transferred to the PMMA layer by developing in a solution of methyl-isobutylketone (MIBK) and isopropanol (IPA) mixed in the ratio MIBK:IPA = 1:3. The pattern is then transferred to the hard SiN_x mask by etching using an inductively-coupled

plasma reactive-ion etching (ICP-RIE) process. After the PMMA layer is removed by dissolution in acetone, ICP-RIE is used to etch the GaN film down to a depth of about 200 nm. Finally, the SiN_x hard mask is removed using buffered oxide etch (BOE). The fabricated GaN photonic crystal structure is examined under a scanning electron microscope; the completed structure is shown in the inset of Figure 4-14. The photonic crystal device was then optically-pumped by a frequency-quadrupled Nd:YAG laser that emits 400-ps pulses at 266 nm. The pump light is focused down to a spot size of about 20 μm around the H2 defect region by a 50X objective lens. Figure 4-14 (a) shows the emission spectra for varying pump input powers ranging from 1 μW to 50 μW. A single emission peak at the wavelength of 363 nm is observed from the GaN photonic crystal. The full-width-half-maximum (FWHM) of the emission peak is estimated to be about 11 nm. Figure 4-14 (b) shows the characteristic curve for the output emission intensity as a function of the input pump power. The threshold input pump power for the onset of emission is about 12.3 W/cm^2. Compared with conventional edge-emitting lasers, a lower threshold is expected for the photonic crystal layers.

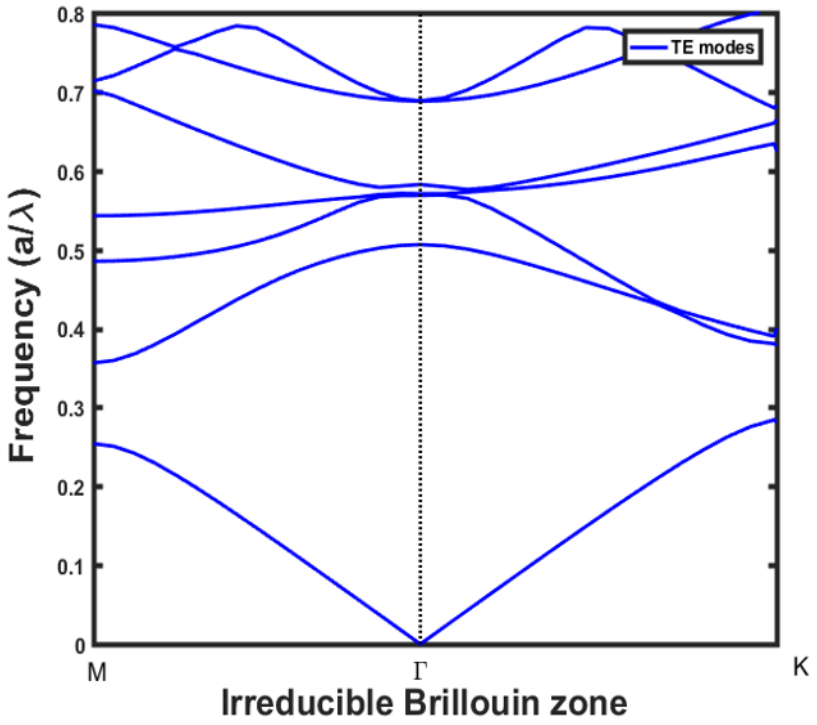

Figure 4-11: Schematic illustration of a photonic crystal band structure with GaN triangular lattice.

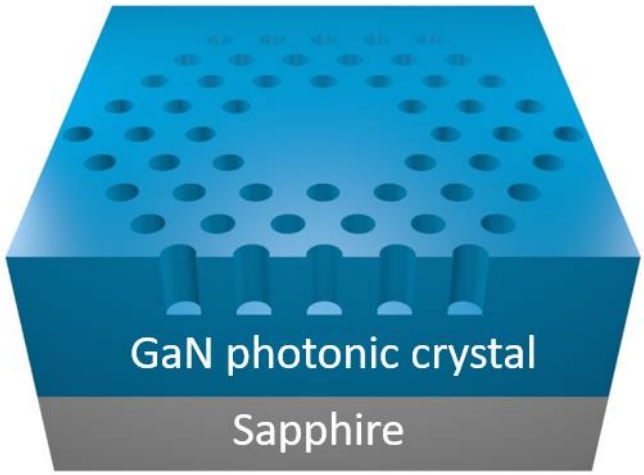

Figure 4-12: Schematic illustration of a GaN H2 defect photonic crystal.

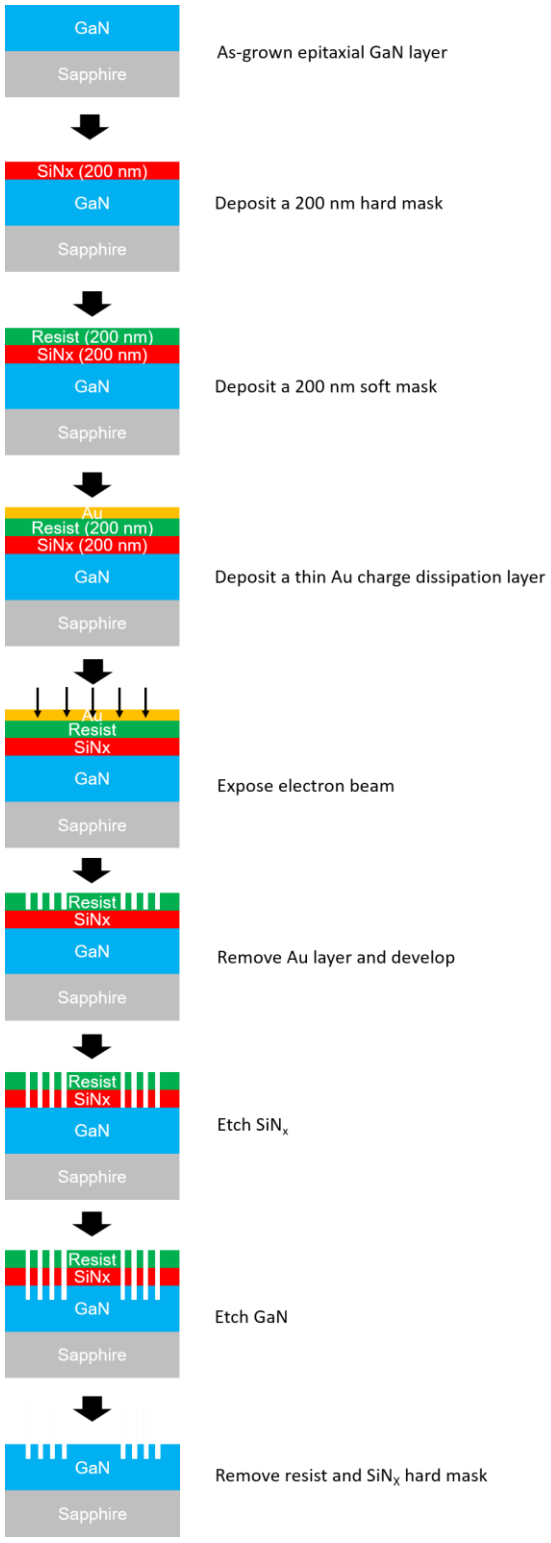

Figure 4-13: Schematic illustration of standard electron-beam lithography process for fabricating defect-type GaN photonic crystals.

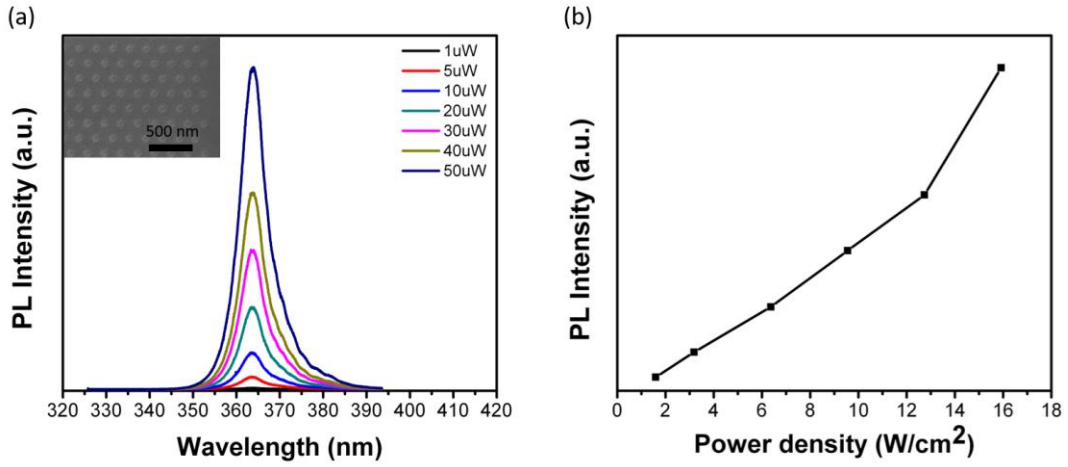

Figure 4-14: (a) PL spectra of defect-type GaN laser structure for different pumping powers. The inset is a scanning electron microscope image of the GaN photonic crystal. (b) PL intensity as a function of input power density.

4.3 Reference

[1] J. D. Joannopoulos, S. G. Johnson, J. N. Winn, and R. D. Meade, *Photonic crystals: Modeling the flow of light*, New Jersey. Princeton University Press, 2008.

Chapter 5
Summary and future work

5.1 Conclusions

The primary focus of this thesis was to develop schemes for growth and fabrication of compact and efficient semiconductor ultraviolet light-emitting devices for a range of applications. Semiconductor ultraviolet light emitters have several unique advantages over conventional sources. However, challenges in the development of high quality and efficiently doped semiconductor thin films of the right band gaps have limited progress in this quest.

In our research work, we have made tremendous progress in successfully developing techniques for synthesis of high quality, highly-doped, high-aluminum-content III-nitride films by using plasma-assisted molecular beam epitaxy under liquid-metal-enabled growth conditions. We show that under these conditions, the prevailing growth mechanism is driven by kinetics, which is unlike that of conventional liquid phase epitaxy as has been incorrectly suggested for liquid-metal-enabled MBE synthesis. Using the new experience and knowledge gained, we demonstrated that extremely high p-type doping of up to 6×10^{17} cm^{-3} and n-type doping of up to 1×10^{20} cm^{-3} in $Al_{0.7}Ga_{0.3}N$ films could be achieved. Furthermore, with the ability to grow high quality high-aluminum-content (Al,Ga)N films, we showed that high quality (Al, Ga)N multi-quantum-wells structures can be grown; these are essential building block structures for UV light emitters. The next logical step after achieving high crystalline quality and highly-doped (Al, Ga)N films, was to integrate them into device structures for deep UV light-emitting diodes. Two categories of AlGaN-based

light-emitting diodes have been investigated: conventional PIN heterostructures and metal-insulator-semiconductor (MIS) Schottky-type diodes. We utilize highly transparent p-type AlGaN layers in the structure of the conventional LED. By careful design of the device structures and control of the growth process, a maximum external quantum efficiency of 0.56% was achieved in our devices. This value is the highest efficiency ever reported for UVC LEDs grown by molecular beam epitaxy. However, AlGaN LEDs in the PIN heterojunction structure generally have high turn-on voltages which mean high energy consumption. We have therefore examined another type of LED structure based on a metal-insulator-semiconductor (MIS) configuration which potentially has low turn-on voltage. Such a low power LED would provide a huge advantage in energy-saving solid-state light emitting sources. The devices we fabricated do have low turn-on voltages but exhibit low emission intensities. We suspect this is probably due to low minority carrier (hole) injection and low carrier confinement. To mitigate this problem, we inserted a GaN quantum well structure at the interface between the insulating AlN layer and the n-type AlGaN semiconductor layer. This structure provided better carrier confinement and yielded relatively higher luminescent intensities.

The successful demonstration of efficient deep UV (Al,Ga)N light-emitting diodes cleared the path for development of coherent UV light sources. We investigated two types of laser structures: a conventional ridge-type edge-emitting laser, and a photonic crystal nanocavity laser. Both structures exhibited lasing characteristics at the ultraviolet wavelength of 360 nm. The defect-type photonic crystal nanocavity laser showed a lower threshold for lasing when compared to the conventional edge-emitting structure. In addition to the lower lasing threshold, the defect-type photonic crystal nanocavity laser has the

advantage that its small volume has low material losses and because it has no mirrors, no losses are suffered from this feature. We therefore believe that the photonic crystal nanolaser is the most viable path toward a deep UV laser for wavelengths below 300 nm.

5.2 References

[1] M. S. Shur and R. Gaska, “Deep-ultraviolet light-emitting diodes,” *IEEE Trans. Electron Devices*, vol. 57, pp. 12–25, 2010.

Appendices

Appendix A : Molecular beam epitaxy

In this Section, we briefly discuss the fundamentals of crystal growth by molecular beam epitaxy (MBE). In MBE growth, group-III metals such as Al, Ga, In and dopants such as Be and Si evaporate from high purity sources in Knudsen effusion cells to produce a stream of atomic fluxes that impinge onto a substrate at an appropriately elevated temperature in an ultra-high vacuum environment. The required nitrogen comes from a gaseous source that is converted to reactive radicals that can be incorporated in the epitaxial film. The most widely used source for generating reactive nitrogen is a radio-frequency (RF) or electron cyclotron resonance (ECR) generator through which the nitrogen is passed to create a plasma comprised of reactive nitrogen ions, free electrons, and neutral nitrogen atoms. Ammonia-based MBE systems, where ammonia molecules are thermally cracked are also in use. These systems however require higher temperature growths than the plasma-based MBE systems. The higher substrate temperatures can lead to high quality III-nitride films.

Growth by molecular beam epitaxy occurs far from thermodynamic equilibrium and is mainly governed by kinetics. The adatoms undergo adsorption, diffusion, incorporation, and desorption processes; these are illustrated in Figure A.1. Different atomic flux rates and arrival times can be precisely controlled by the temperature of the source and the substrate, as well as by timing of the opening of the mechanical shutters associated with the source. These features of molecular beam epitaxy enable growth of ultra-thin quantum layers with very sharp interfaces. The MBE growth method is also flexible to allow the engineering of

high quality two-dimensional planar films, superlattices, nanowires, and quantum dots simply by tuning the group III to group V ratios of the sources and the substrate temperature. Another advantage of this technique is that crystal surface reconstruction and the surface morphology of the epitaxial films can be analyzed and understood through use of reflection high-energy electron diffraction (RHEED), a technique that can provide a wealth of information about the epitaxial film growth process. At present the MBE growth technique is one of the most important approaches for growing high quality semiconductor thin films.

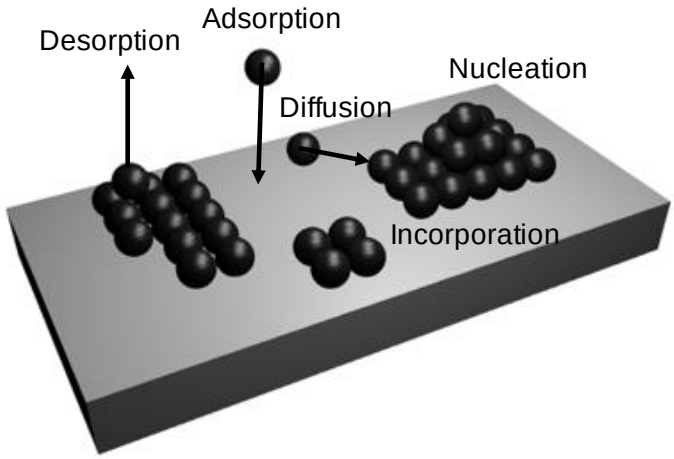

Figure A.1: Schematic illustration of the surface processes occurring during epilayer growth by MBE.

Figure A.2 shows a schematic layout of our RIBER Compact 12 MBE system. The chamber is equipped with effusion cells that contain high purity Al, Ga, In, Mg, metals and Si. The beam equivalent pressure (BEP) of each of these elements can be measured by a Bayard-Alpert type nude ionization gauge. An RF plasma source is employed for generating active nitrogen in our system. Ultra-high pure nitrogen is introduced into a prolytic boron nitride (PBN) cavity, where RF energy at 13.56 MHz is inductively coupled through a

copper coil to create a plasma of ionized nitrogen atoms, neutral nitrogen atoms, and electrons striped off from the nitrogen. The MBE system is also equipped with a 10-kV RHEED gun, a phosphor display screen, and a camera that provides real-time images for analyzing the crystal growth processes. The angle of incidence of the high energy electron beam is typically about 1° with respect to the surface of the epitaxial film. The ultimate pressure in this system can be as low as 10^{-10} Torr. This ultra-high vacuum environment minimizes incorporation of unwanted impurities such as carbon and hydrogen in the epitaxial films during e growth. High quality (Al,In,Ga)N-based films can be grown by optimizing the substrate temperature, source cell temperatures, and the group III to group V ratio of the constituent fluxes in the MBE system.

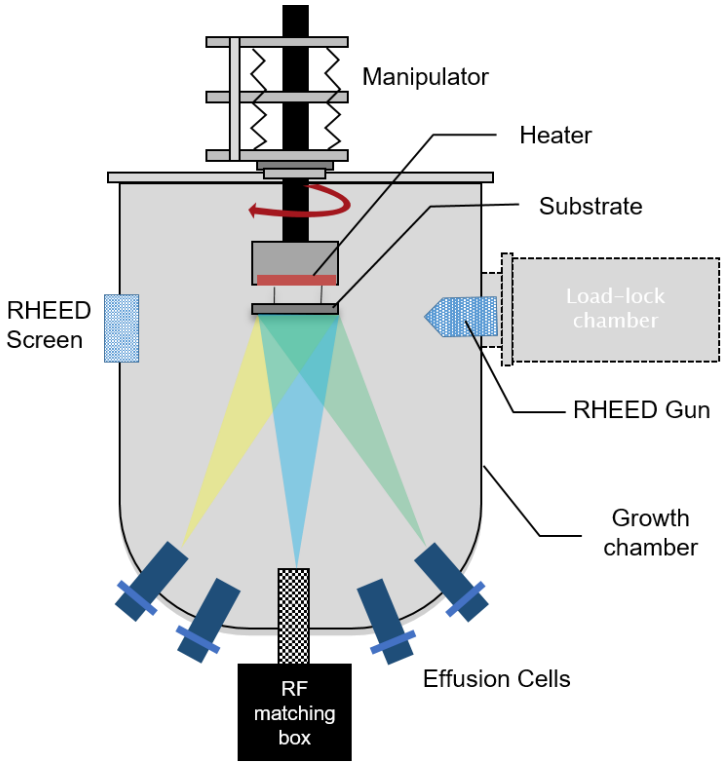

Figure A.2: Schematic of RIBER compact 12 MBE system.

Appendix B : MBE growth process

Prior to loading samples into the MBE chamber, the sapphire substrates, which are coated with molybdenum on the backside, should be cleaned in the following sequence: in acetone for 10 minutes, iso-propanol for 10 minutes, methanol for 10 minutes, in a mixture of $HCl:H_3PO_4$ = 3:1 at 100^oC for 30 minutes, and rinsed with DI water. An outgassing process is then performed on the cleaned substrates at 800^oC in the MBE chamber for 30 minutes. Following this, the sapphire substrate is nitridated at 750^oC for 30 minutes.

The beam fluxes of each effusion cells must be measured by an ion-gauge during the calibration process. The quality of the growing film and its morphology can be examined *in-situ* by a RHEED system during the growth. Throughout the deposition process, a continuous flow of liquid nitrogen is used to cool around the substrate holder and cells to remove condensable contaminants such as CO_2 and H_2O from the growth environment.

Appendix C : Characterization

After growth, the III-nitride thin films are characterized by several well-established techniques to obtain their structural, optical, and electrical properties. Information obtained from the characterization is important for optimizing the quality of the films for use in device structures.

C.1 Structural characterization

The structural and compositional properties of the III-nitride films are characterized by high resolution X-ray diffraction (HRXRD) and transmission electron microscopy (TEM). For the X-ray diffraction, we use a Panalytical X'Pert Pro X-ray Diffractometer system. One can obtain crystal structure, strain, and composition information with using this system. A schematic configuration of the X-ray diffraction set-up is illustrated Figure C.1. Crystal orientation and lattice spacing information can be determined from the position of the diffraction peak according to Bragg's law:

$$2 \cdot d \cdot sin\theta = n\lambda \tag{B.1}$$

where d is the inter-plane spacing in the crystal, λ is the wavelength of the X-ray radiation, θ is the angle of incidence for the radiation, and n is an integer. A typical composition of an (Al, Ga)N film can be determined from the HRXRD ω-2θ scans. By Vegard's law [1], the mole fraction in an alloy can be easily evaluated as

$$Al\ mole\ fraction\ (x) = \frac{\Delta\theta}{\Delta\theta_0} \tag{B.2}$$

where $\Delta\theta$ is the angular shift of of the $Al_xGa_{1-x}N$ peak from that of the AlN, and $\Delta\theta_0$ is the angular shift of the AlN peak to that of GaN.

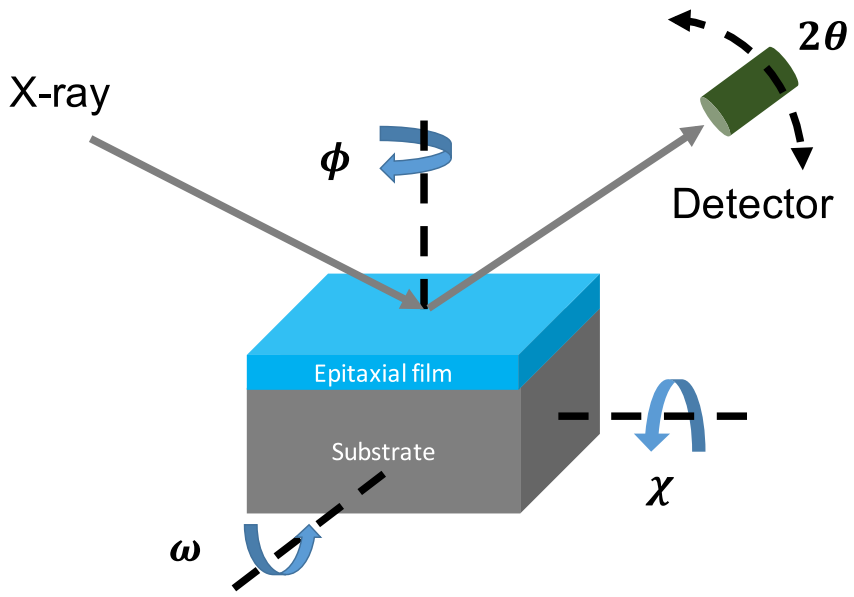

Figure C.1: Schematic configuration of X-ray diffraction set-up.

In addition to the XRD analysis, the composition of (Al, Ga)N-based epitaxial layers is also characterized by field emission Titan TEM equipped with an energy dispersive x-ray (EDX) spectrometer. An illustration of a typical implementation of an EDX system in a TEM is shown in Figure C.2. Characteristic X-ray radiation carrying information about elements in a specimen of interest are collected by the EDX spectrometer which displays the information. This technique can generally be coupled with scanning transmission electron microscopy (STEM) to record the energy-based elemental mapping images to extract information on compositional distribution in the sample. In addition to the TEM-EDX analysis, Z-contrast high angle annular dark field (HAADF) electron micrographs can be used to obtain information on quantum well structures. Figure C.2 depicts how the HAADF detector gathers electrons scattered through very high angles ($\theta >$ 50 mrad). The

compositional contrast is proportional to the atomic number Z, i.e. intensity ~ Z^2. Because of this dependence, it can enhance compositional contrast and provide better resolution images.

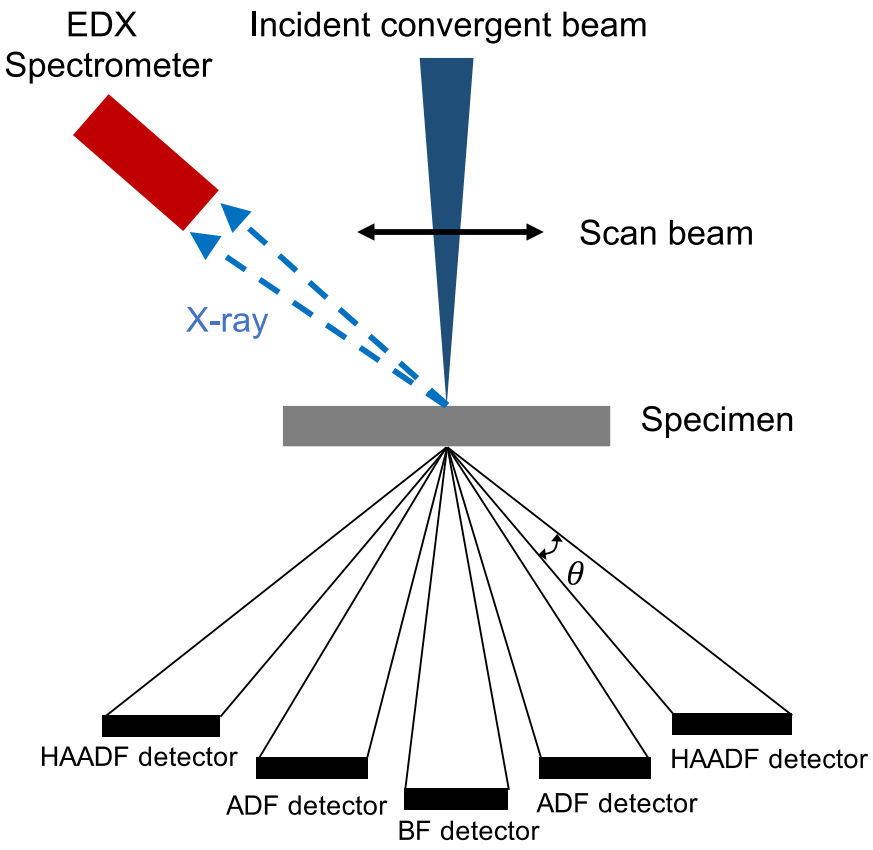

Figure C.2: Schematic illustration of STEM image detectors on EDX and HAADF.

C.2 Optical characterization

Photoluminescence (PL) is a major tool for evaluating the emission properties, crystalline quality, and doping characteristics of epitaxial AlGaN fims and device structures. We use a combination mini-Raman/PL system with a Hg-Ag deep UV pulsed laser source emitting at 248.6 nm as an excitation source for the PL measurements. The incident laser

excites electron-hole pairs in the semiconductor. These recombine and emit photons that are collected by a spectrometer. The spectrometer has a 1200 /mm grating for dispersing the collected photons which are directed to a photomultiplier (PMT) connected to a signal processor. Our system is equipped with cryostat for performing temperature-dependent PL. The cryostat facilitates the study of impurity and defect states in the materials or devices of interest.

C.3 Electrical characterization

The electrical properties of epitaxial III-nitride films doped with Si or Mg are characterized by conventional Hall effect measurements, using the Van der Pauw method. Figure C.3 shows the setup of the Hall effect system for measuring the Hall voltage, $V_{H,}$ for a semiconductor material where an electric field is applied along the x-axis and a magnetic field (B_Z) is applied along the z-axis. Charge carriers of either polarity (electrons or holes) pile up at one side of the sample due to the Lorentz force exerted on them; this force can be expressed as

$$F_L = qv_x \times B_Z \tag{B.3}$$

where v_x represents the carrier velocity which is related to the current density through

$$J_x = qv_x p = qv_x n \tag{B.4}$$

By balancing the Lorentz force with the force exerted by the Hall field, one obtains

$$qE_y = qv_x B_Z \tag{B.5}$$

where the Hall voltage, V_H, is externally measured and is expressed as

$$V_H = E_y w = \frac{J_x B_Z w}{qp} = R_H J_x B_Z w \tag{B.6}$$

where R_H is the Hall coefficient which representing the inverse of charge carrier density. The sign of the Hall coefficient determines whether electrons or holes predominate the available charge carriers. The sign of R_H is negative when electrons are the majority charge carriers and vice versa. As a result, Hall effect measurements provide a unique approach to extracting information about carrier type, carrier concentration, and resistivity of a film.

In our work, we use a model HEM-2000 Hall measurement system for characterizing the III-nitride films. The magnetic flux density applied in this system is 0.27 T, and all the measurements are carried out at room temperature.

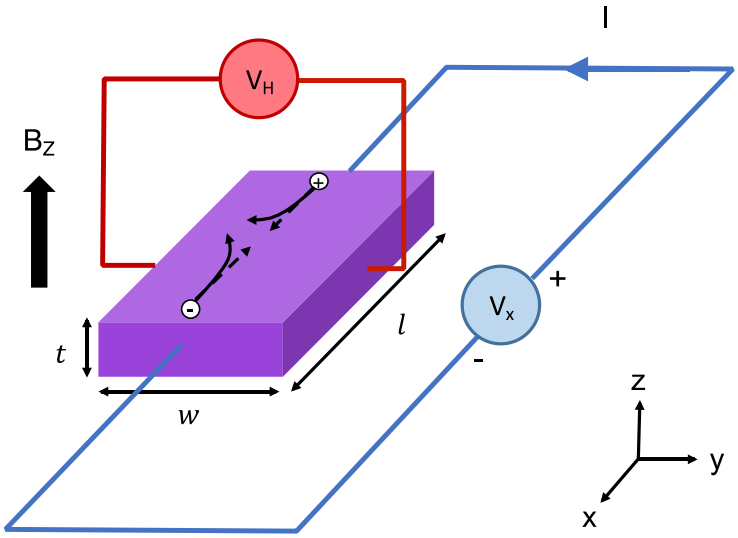

Figure C.3: Schematic representation of the Hall effect on measuring electrical properties of a semiconductor.